Shockley Surface States
from
First Principles

Masterarbeit

zur Erlangung des akademischen Grades eines
Master of Science
an der naturwissenschaftlichen Fakultät der
Karl-Franzens-Universität Graz

vorgelegt von

Dario Wolf Knebl

am Institut für Physik
Fachbereich für theoretische Physik

Betreuer: Ass.-Prof. Dr. Peter Puschnig

Graz, 2013

In the first part of this thesis, a comprehensive ab-initio study within the framework of density functional theory (DFT) of all Shockley surface states of the (110), (100), and (111) facets of the face-centered cubic metals Al and Cu is performed. By comparing the bulk projected band structure with those of slab calculations, Shockley surface states are identified and a comprehensive analysis of their characteristic properties is conducted. Particular care is put on the convergence of calculated energy positions and effective masses of surface states with respect to the number of metallic layers used in our repeated slab approach. In addition to band offsets and band dispersions, also computed surface energies, work functions, as well as typical decay lengths of surface states into the bulk and into the vacuum are compared among the investigated metals and facets and compared to available experimental data. Moreover, the DFT calculations are used to simulate angle-resolved photoemission (ARPES) intensities within the one-step model of photoemission.

In the second part of the thesis, the prototypical organic/metal interface PTCDA/Ag(110) is investigated. A careful convergence study on the projected density of states (pDOS) with respect to the number of atomic silver layers is performed. This highlights a parity dependence of the pDOS in the energy range of the lowest unoccupied molecule orbital (LUMO) on the number of silver layers. Additionally, photoemission intensities are simulated which allow a three-dimensional analysis of this issue.

Contents

List of Figures

List of Tables

1 Introduction

Shockley surface states of metals, first described by William Shockley [1], are long known to significantly affect the properties of solid surfaces in many aspects, such as molecular adsorption mechanisms. They exist in gaps of the bulk projected band structure of metals and affect details of the surface potential, which is important for dissociation rates and catalytic reactions [2]. Electrons which occupy such surface states are located only to few atom layers or even only to the topmost atom layer at the surface. The probability of finding such an electron decreases exponentially from the surface into the bulk material. Typical experiments to observe surface states are angle-resolved photoemission spectroscopy (ARPES) and scanning tunneling microscopy (STM). Often surface states contribute to bonding processes or even make bonding possible, e.g. molecule-monolayers on metal surfaces, by a hybridization of the energy bands corresponding to the surface state with energy bands of the molecule.

One aim of this thesis is to calculate characteristic properties of Shockley surface states. In order to calculate their electronic structures, from which all physical information of these surface states can be derived, from first principles, *i.e.* without the use of empirical data, an underlying theory which accounts for the quantum mechanical nature of the electron is needed. This basic theory is given by the many-electron Schrödinger equation. Only for a small number of very simple systems, analytic solutions of the single-electron Schrödinger equation have been found. For systems containing several electrons, the solution can only be obtained numerically, however, the computational effort scales exponentially with respect to the number of electrons. Thus, unfortunately, for most other cases, including metal surfaces, there is need for computational schemes and for approximations of the Hamiltonian of the Schrödinger equation. During the last century, a host of approximations and schemes which solve the many-electron-Schrödinger equation has been developed. One formalism, which does not seek to solve the many-electron Schrödinger equation, but to obtain properties of the electronic ground state from the electron density, is the density functional theory (DFT). In contrast to most other methods, where the many-electron wave functions are considered, the DFT is based on the electron density of the system. This approach was first proposed by Thomas and Fermi in 1927. A few decades later, in 1964, Hohenberg and Kohn gave the proof that the electron density can be handled as the basic property of a quantum-mechanical system [3]. In principle, the DFT is exact, but the main problem is that the total energy is not known solely in terms of the electron density. Unfortunately, the proof of Hohenberg and Kohn does not include a scheme for a practical use. A year after, Kohn and Sham presented such a practical concept, using the so-called Kohn-Sham equations [4]. In principle, this concept is also exact as long the total energy is explicitly known in terms of the density. For these unknown parts there has been elaborated a huge amount of approximations. One of them, which is used within this thesis, is the generalized gradient approximation (GGA), in particular the GGA-PBE, named after its authors Perdew, Burke, and Ernzerhof [5, 6].

In this thesis, relaxed uncovered low-index metal surfaces of aluminium and copper and a prototypical molecule/metal interface are investigated. In Chapter 2 the underlying basic concepts, such as the many-particle Schrödinger equation and facets of the face center cubic crystal, are briefly introduced. In Chapter 3 an introduction to DFT is given, by presenting the two theorems of Hohenberg and Kohn, Kohn-Sham formalism, and a brief overview of GGA. Within this thesis, the Vienna Ab-inito Simulation Package (VASP) has been used for solving the Kohn-Sham equations. Its applications with respect to this thesis are also introduced in Chapter 3, as well as the one-step model, which provides a framework to calculate photoemission intensities. Thereafter, in Chapter 4, the main part of this thesis, the calculated results are presented. This chapter consists of two parts. The first part contains a study of uncovered metal surfaces, namely the (110), the (100), and the (111) facets of aluminium and copper. Surface energies and work functions for these facets are calculated and compared to experimental data from literature. By use of the bulk projected band structure method, Shockley surface states of the investigated facets are detected and a careful convergence study with respect to the number of atom layers of characteristic properties, such as the effective electron mass, is performed. Thereafter, the DFT calculations are used to calculate photoemission intensity maps for Cu(110) within the one-step model. In the second part of Chapter 4, the molecule/metal interface PTCDA/Ag(110) is investigated motivated by recent research on this prototypical organic/metal interface [7, 8]. First, a careful convergence study on the projected density of states (pDOS) with respect to the number of atomic silver layers is performed. Thereby, in the energy range of the lowest unoccupied molecular orbital (LUMO), a characteristic dependence of the pDOS on the parity of the layer number is obtained. In detail, while for an even number of layers one intensity peak is obtained, for an odd number of layers three peaks appear. These merge into one peak for layer numbers greater than 19 or so. Moreover, photoemission intensity maps are calculated in order to receive a three-dimensional view to this issue, and further to analyse an unknown feature stated in Ref. [7]. Finally, photoemission intensity maps of the PTCDA/Ag(110) system are compared to band structures of the uncovered Ag(110) surface.

2 Basic Concepts

In this chapter the Schrödinger equation, the fundamental equation within this thesis, is introduced briefly. Afterwards, some crystal surfaces, which are used in the simulation part of the thesis are considered. The corresponding Brillouin zones are constructed and proper paths inside the Brillouin zones are defined. Moreover, surface states, bulk states and resonance states are distinguished. Finally, the photoelectric effect is brought up.

2.1 Many electron Schrödinger equation

The properties of materials are governed by the electro-static interaction between electrons and atomic nuclei. Within the Born-Oppenheimer approximation which allows to separate the electronic from the nuclear dynamics, the fundamental equation is the many-electron Schrödinger equation for the electrons.

$$i\hbar\frac{\partial}{\partial t}\Psi = \hat{H}\Psi \tag{2.1}$$

Usually one separates the spatial and temporal variables by

$$\Psi = \psi e^{-iEt/\hbar} \tag{2.2}$$

The resulting stationary non-relativistic Schrödinger equation is

$$\hat{H}\psi(\mathbf{r}_1\sigma_1, \mathbf{r}_2\sigma_2, ..., \mathbf{r}_N\sigma_N) = E\psi(\mathbf{r}_1\sigma_1, \mathbf{r}_2\sigma_2, ..., \mathbf{r}_N\sigma_N). \tag{2.3}$$

The Hamiltonian for N electrons is [9, 10, 11]

$$\hat{H} = \underbrace{-\frac{\hbar^2}{2m}\sum_{i=1}^{N}\nabla_i^2}_{=\hat{T}} + \underbrace{\sum_{i=1}^{N} v(\mathbf{r}_i)}_{=\hat{V}_{\text{ext}}} + \underbrace{\frac{1}{2}\sum_{i=1}^{N}\sum_{j\neq i}^{N}\frac{e^2}{|\mathbf{r}_i - \mathbf{r}_j|}}_{=\hat{V}_{\text{ee}}} \tag{2.4}$$

where $\hat{T}$ is the kinetic energy, $\hat{V}_{\text{ext}}$ is the external potential and $\hat{V}_{\text{ee}}$ is the electron-electron interaction. Electrons are known to be fermions, according to the spin-statistic theorem the solution of Eq. 2.3 has to be antisymmetric with respect to particle exchange

$$\psi(\mathbf{r}_1\sigma_1, ..., \mathbf{r}_i\sigma_i, ..., \mathbf{r}_j\sigma_j, ..., \mathbf{r}_N\sigma_N) = -\psi(\mathbf{r}_1\sigma_1, ..., \mathbf{r}_j\sigma_j, ..., \mathbf{r}_i\sigma_i, ..., \mathbf{r}_N\sigma_N) \tag{2.5}$$

From the antisymmetric behaviour it follows that there are $N!$ permutations of the indices with the same $|\psi|^2$. Hence the probability of detecting an electron with the spin σ_1 in the volume element d^3r_1, an electron with the spin σ_2 in the volume element d^3r_2, and so on, is given by

$$N!|\psi(\mathbf{r}_1\sigma_1, \mathbf{r}_2\sigma_2, ..., \mathbf{r}_N\sigma_N)|^2 d^3r_1 d^3r_2 \ldots d^3r_N \tag{2.6}$$

The summation over all spins and the integration over all spatial coordinates are

$$\frac{1}{N!}\sum_{\sigma_1\ldots\sigma_N}\int_{\mathbb{R}^{3N}} N!|\psi(\mathbf{r}_1\sigma_1, \mathbf{r}_2\sigma_2, ..., \mathbf{r}_N\sigma_N)|^2 d^3r_1 d^3r_2 \ldots d^3r_N = 1 \tag{2.7}$$

Further one can define the electron spin density $n_\sigma(\mathbf{r})$ as the probability of finding an electron in d^3r at $\mathbf{r}$ with the spin σ.

$$n_\sigma(\mathbf{r}) = \frac{1}{(N-1)!}\sum_{\sigma_2\ldots\sigma_N}\int_{\mathbb{R}^{3(N-1)}} N!|\psi(\mathbf{r}\sigma, \mathbf{r}_2\sigma_2, ..., \mathbf{r}_N\sigma_N)|^2 d^3r_2 \ldots d^3r_N \tag{2.8}$$

$$= N\sum_{\sigma_2\ldots\sigma_N}\int_{\mathbb{R}^{3(N-1)}} |\psi(\mathbf{r}\sigma, \mathbf{r}_2\sigma_2, ..., \mathbf{r}_N\sigma_N)|^2 d^3r_2 \ldots d^3r_N \tag{2.9}$$

2.1.1 The variational principle

Often one is interested in the ground state $|\psi\rangle$ of a Hamiltonian $\hat{H}$ with the ground state energy E_0. The definition

$$E[\psi] \equiv \frac{\langle\psi|\hat{H}|\psi\rangle}{\langle\psi|\psi\rangle} \tag{2.10}$$

leads directly to the

Variational principle: $\forall\psi : E[\psi] \geq E_0$

A practically important consequence is

$$E_0 = \min_\psi E[\psi] \tag{2.11}$$

Moreover, the division by the scalar product of the wavefunction guarantees the constraint $\langle\psi|\psi\rangle = 1$.

Proof. Let be $\{\psi_i\}$ the orthonormal eigenset of $\hat{H}$. Then $\psi = \sum_i c_i\psi_i$. Using Eq. 2.10 one gets

$$E[\psi] = \frac{\langle\psi|\hat{H}|\psi\rangle}{\langle\psi|\psi\rangle} = \frac{\sum_i |c_i|^2 E_i}{\sum_i |c_i|^2} \geq \frac{\sum_i |c_i|^2 E_0}{\sum_i |c_i|^2} = E_0 \tag{2.12}$$

because $E_0 \leq E_1 \leq E_2 \leq \ldots \square$

2.1.2 The Hellmann-Feynman-Theorem

Assume that the energy of a quantum system (with normalized wave functions) depends on a parameter λ.

$$E_\lambda = \langle\psi_\lambda|\hat{H}_\lambda|\psi_\lambda\rangle \tag{2.13}$$

One can consider the derivative

$$\frac{\partial E_\lambda}{\partial \lambda} = \frac{\partial}{\partial \tilde{\lambda}} \langle \psi_{\tilde{\lambda}} | \hat{H}_\lambda | \psi_{\tilde{\lambda}} \rangle \Bigg|_{\tilde{\lambda}=\lambda} + \langle \psi_\lambda | \frac{\partial \hat{H}_\lambda}{\partial \lambda} | \psi_\lambda \rangle \tag{2.14}$$

Using the variational principle, namely Eq. 2.11 one gets

$$\frac{\partial}{\partial \tilde{\lambda}} \langle \psi_{\tilde{\lambda}} | \hat{H}_\lambda | \psi_{\tilde{\lambda}} \rangle \Bigg|_{\tilde{\lambda}=\lambda} = 0 \tag{2.15}$$

Now Eq. 2.14 becomes

$$\frac{\partial E_\lambda}{\partial \lambda} = \langle \psi_\lambda | \frac{\partial \hat{H}_\lambda}{\partial \lambda} | \psi_\lambda \rangle \tag{2.16}$$

This is the Hellmann-Feynman theorem. An important application of the Hellmann-Feynman theorem is to determine the equilibrium geometries of the ions in a solid. To this end, an Hamiltonian with the positions of the ions $\mathbf{R}_\alpha$ as parameters has to be used.

$$\hat{H} = -\frac{\hbar^2}{2m} \sum_{i=1}^{N} \nabla_i^2 + \frac{1}{2} \sum_{i=1}^{N} \sum_{j \neq i}^{N} \frac{e^2}{|\mathbf{r}_i - \mathbf{r}_j|} + \sum_{i=1}^{N} \sum_{\alpha}^{M} \frac{e^2 Z_\alpha}{|\mathbf{r}_i - \mathbf{R}_\alpha|} + \frac{1}{2} \sum_{\alpha=1}^{M} \sum_{\beta \neq \alpha}^{M} \frac{e^2 Z_\alpha Z_\beta}{|\mathbf{R}_\alpha - \mathbf{R}_{beta}|} \tag{2.17}$$

Equilibrium will be reached, if the energy of the system is minimized and the forces on the ions

$$F_{\mathbf{R}_\alpha} = \nabla_{\mathbf{R}_\alpha} E = \langle \psi | \nabla_{\mathbf{R}_\alpha} \hat{H} | \psi \rangle \overset{!}{=} 0 \tag{2.18}$$

vanish.

2.1.3 Bloch's theorem

A crystal is characterized through its periodicity which is mathematically described by a spatially periodic potential in the Schrödinger equation. Bloch's theorem states the resulting properties to the wave functions of such a system with translational symmetry. The Schrödinger equation for an electron in a crystal reads

$$\Big(-\frac{\hbar^2}{2m} \nabla_{\mathbf{r}}^2 + V(\mathbf{r}) \Big) \psi_{n\mathbf{k}}(\mathbf{r}) = E_n(\mathbf{k}) \psi_{n\mathbf{k}}(\mathbf{r}) \tag{2.19}$$

where n denotes the band index and $\mathbf{k}$ is the wavevector or the crystal momentum of the corresponding electron. Furthermore, the periodicity of the (infinite) crystal leads to [12]

Bloch's theorem: If $V(\mathbf{r} + \zeta_1 \cdot \mathbf{a}_1 + \zeta_2 \cdot \mathbf{a}_2 + \zeta_3 \cdot \mathbf{a}_3) = V(\mathbf{r})$, with $\zeta_i \in \mathbb{Z}$ and three linear independent vectors $\mathbf{a}_i$, then the solutions are $\psi_{n\mathbf{k}}(\mathbf{r}) = u_{n\mathbf{k}}(\mathbf{z}) \exp\{i\mathbf{k} \cdot \mathbf{r}\}$, where $u_{n\mathbf{k}}(\mathbf{r} + \zeta_1 \cdot \mathbf{a}_1 + \zeta_2 \cdot \mathbf{a}_2 + \zeta_3 \cdot \mathbf{a}_3) = u_{n\mathbf{k}}(\mathbf{r})$.

The theorem states that for a periodic potential the wavefunction is given by a plane wave times a periodic function with the same periodicity as the potential. Note, that Bloch's theorem mathematically holds only for infinite crystals.

2.2 Crystal surfaces

All crystals investigated in this thesis are of the type face centered cubic (fcc) [12, 13] - see Fig. 2.1. In this section, the unit cell vectors of an fcc-crystal are reviewed. Then, three crystal surfaces are graphically displayed, namely the (100), (110) and (111) surface. For the later use, their unit cells are constructed. Further the unit cell vectors and the positions of the lattice points are calculated. Moreover, the reciprocal lattice vectors of those three unit cells are computed. As well, the Brillouin zone (BZ) of the fcc-crystal and in particular the Brillouin zones of the three surfaces are graphically displayed. Finally, **k**-paths in the Brillouin zones are suggested. To this end, some special points in the BZs are calculated.

2.2.1 The face centered cubic crystal

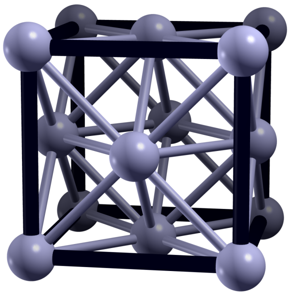

Figure 2.1: The unit cell of the fcc crystal.

The primitive lattice vectors of the fcc crystal are

$$\mathbf{a}_1 = \frac{a}{2}\begin{pmatrix} 0 \\ 1 \\ 1 \end{pmatrix} \tag{2.20}$$

$$\mathbf{a}_2 = \frac{a}{2}\begin{pmatrix} 1 \\ 0 \\ 1 \end{pmatrix} \tag{2.21}$$

$$\mathbf{a}_3 = \frac{a}{2}\begin{pmatrix} 1 \\ 1 \\ 0 \end{pmatrix} \tag{2.22}$$

2.2.2 Facets

A plane can be described by its normal vector

$$\mathbf{n} = \begin{pmatrix} l \\ m \\ n \end{pmatrix} \propto \begin{pmatrix} 1/s_x \\ 1/s_y \\ 1/s_z \end{pmatrix} \tag{2.23}$$

where s_x is the point of intersection of the x-axis and so on. The integer numbers l, m and n (with the smallest possible absolute values) are called Miller indices. A plane is then denoted by the expression (lmn). A negative number is usually denoted by an overline, e.g. $(10\overline{1})$. Moreover, one can write directions in a similar way, by using square brackets $[xyz]$, e.g. [100] for the x-direction.

As already mentioned, three surfaces are considered. Figs. 2.2a, 2.2b, and 2.2c show the lattice planes (100), (110) and (111) in the fcc crystal. In Fig. 2.2 the hatched areas define the unit cells of the facets. The red arrows define the lattice vectors of the unit cells of the facets. The black, gray and white spheres picture the atoms of the first, second and third layer. They lay on different planes parallel to the page. With the knowledge of the lattice vectors and the positions of the lattice points it is possible to build up an crystal with the desired surface.

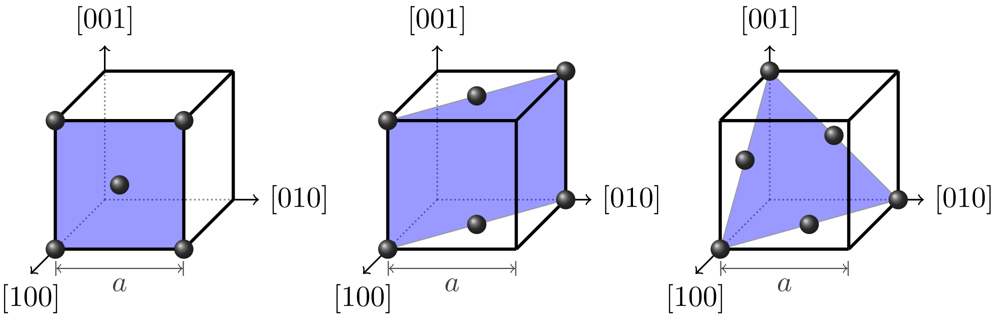

(a) The (100) facet of the fcc crystal.

(b) The (110) facet of the fcc crystal.

(c) The (111) facet of the fcc crystal.

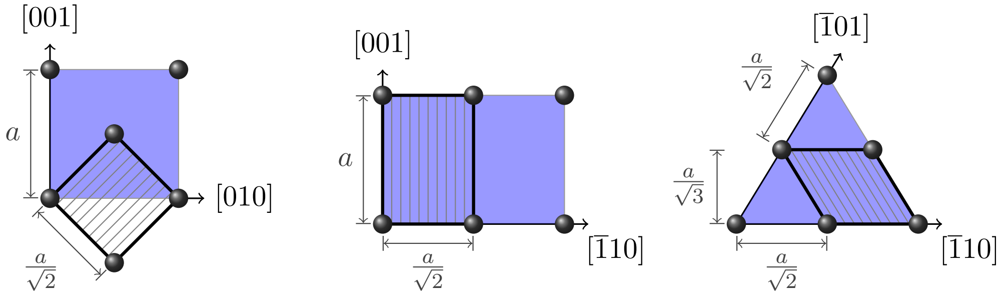

(d) The hatched area pictures the unit cell of the (100) facet.

(e) The hatched area pictures the unit cell of the (110) facet.

(f) The hatched area pictures the unit cell of the (111) facet.

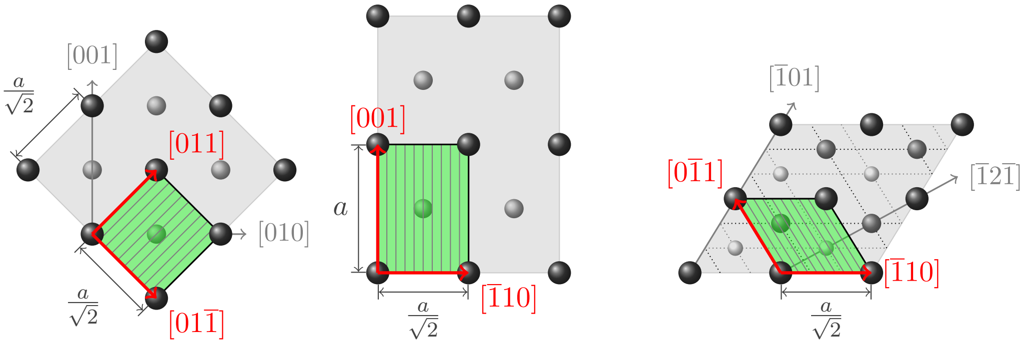

(g) The red arrows denote the lattice vectors of the (100) facet.

(h) The red arrows denote the lattice vectors of the (110) facet.

(i) The red arrows denote the lattice vectors of the (111) facet.

Figure 2.2: The (100), (110) and (111) facets of the fcc crystal.

Calculation of the lattice vectors

The (100) **facet.** The lattice vectors are represented by the red arrows of Fig. 2.2g. By defining the x-axis in $[01\bar{1}]$-direction, the y-axis in $[011]$-direction and the z-axis in $[100]$-direction, the (100) lattice vectors are

$$\mathbf{a}_1 = \frac{a}{\sqrt{2}} \begin{pmatrix} 1 \\ 0 \\ 0 \end{pmatrix}, \ \mathbf{a}_2 = \frac{a}{\sqrt{2}} \begin{pmatrix} 0 \\ 1 \\ 0 \end{pmatrix}, \ \mathbf{a}_3 = a \begin{pmatrix} 0 \\ 0 \\ 1 \end{pmatrix} \tag{2.24}$$

The cell contains two atoms at positions

$$\mathbf{P}_1 = \mathbf{0}, \mathbf{P}_2 = \frac{1}{2}\mathbf{a}_1 + \frac{1}{2}\mathbf{a}_2 + \frac{1}{2}\mathbf{a}_3 \tag{2.25}$$

and hence of two different layers. The layer sequence is ABABAB.. .

The (110) **facet.** The lattice vectors are represented by the red arrows of Fig. 2.2h. By defining the x-axis in $[\bar{1}10]$-direction, the y-axis in $[001]$-direction and the z-axis in $[110]$-direction, the (110) lattice vectors are

$$\mathbf{a}_1 = \frac{a}{\sqrt{2}} \begin{pmatrix} 1 \\ 0 \\ 0 \end{pmatrix}, \ \mathbf{a}_2 = a \begin{pmatrix} 0 \\ 1 \\ 0 \end{pmatrix}, \ \mathbf{a}_3 = \frac{a}{\sqrt{2}} \begin{pmatrix} 0 \\ 0 \\ 1 \end{pmatrix} \tag{2.26}$$

The cell contains two atoms at positions

$$\mathbf{P}_1 = \mathbf{0}, \mathbf{P}_2 = \frac{1}{2}\mathbf{a}_1 + \frac{1}{2}\mathbf{a}_2 + \frac{1}{2}\mathbf{a}_3 \tag{2.27}$$

and of two different layers. The layer sequence is ABABAB.. .

The (111) **facet.** The lattice vectors are represented by the red arrows of Fig. 2.2i. The x-axis is choosen to show in direction of $[\bar{1}2\bar{1}]$ and the y-axis shows in direction of $[0\bar{1}1]$. The z-axis cleary shows in direction of $[111]$. The lattice vector $\mathbf{a}_1$ shows into direction $[\bar{1}10]$, $\mathbf{a}_2$ shows into direction $[0\bar{1}1]$, and, $\mathbf{a}_3$ shows into direction $[111]$. The length of $\mathbf{a}_3$ is the space diagonal $\sqrt{3}a$ of Fig. 2.2c. The coordinates $a_{2,y} = \frac{a}{\sqrt{2}}$, $a_{2,x} = 0$, $a_{1,y} = -\frac{a}{2\sqrt{2}}$ and

$$a_{1,x} = \sqrt{\left(\frac{a}{\sqrt{2}}\right)^2 - \left(\frac{a}{2\sqrt{2}}\right)^2} = \sqrt{\frac{3a^2}{8}} = \sqrt{\frac{3}{2}}\frac{a}{2} \tag{2.28}$$

follows from Fig. 2.2i. The (111) lattice vectors are

$$\mathbf{a}_1 = \frac{a}{2\sqrt{2}} \begin{pmatrix} \sqrt{3} \\ -1 \\ 0 \end{pmatrix}, \ \mathbf{a}_2 = \frac{a}{\sqrt{2}} \begin{pmatrix} 0 \\ 1 \\ 0 \end{pmatrix}, \ \mathbf{a}_3 = \sqrt{3}a \begin{pmatrix} 0 \\ 0 \\ 1 \end{pmatrix} \tag{2.29}$$

The cell contains three atoms at positions

$$\mathbf{P}_1 = \mathbf{a}_1, \mathbf{P}_2 = \frac{2}{3}\mathbf{a}_1 + \frac{1}{3}\mathbf{a}_2 + \frac{1}{3}\mathbf{a}_3, \mathbf{P}_3 = \frac{1}{3}\mathbf{a}_1 + \frac{2}{3}\mathbf{a}_2 + \frac{2}{3}\mathbf{a}_3 \tag{2.30}$$

and of three different layers. The layer sequence is ABCABCABC.. .

2.2.3 The reciprocal lattice

The reciprocal lattice is defined through

$$e^{i\mathbf{K}\cdot\mathbf{R}} = 1 \tag{2.31}$$

where $\mathbf{K}$ is a point of the reciprocal lattice and $\mathbf{R}$ is a point of the 'real space' lattice. If $\mathbf{a}_1, \mathbf{a}_2, \mathbf{a}_3$ are the lattice vectors then the cell volume is $V = \mathbf{a}_1 \cdot (\mathbf{a}_2 \times \mathbf{a}_3)$ and the reciprocal lattice vectors are

$$\begin{aligned} \mathbf{b}_1 &= \frac{2\pi}{V}(\mathbf{a}_2 \times \mathbf{a}_3) \\ \mathbf{b}_2 &= \frac{2\pi}{V}(\mathbf{a}_3 \times \mathbf{a}_1) \\ \mathbf{b}_3 &= \frac{2\pi}{V}(\mathbf{a}_1 \times \mathbf{a}_2) \end{aligned} \tag{2.32}$$

The reciprocal lattice vectors of the (100) facet

By using Eq. 2.32 one gets

$$V = \frac{a^3}{2} \tag{2.33}$$

and further

$$\mathbf{b}_1 = \frac{2\pi}{a}\begin{pmatrix} \sqrt{2} \\ 0 \\ 0 \end{pmatrix}, \ \mathbf{b}_2 = \frac{2\pi}{a}\begin{pmatrix} 0 \\ \sqrt{2} \\ 0 \end{pmatrix}, \ \mathbf{b}_3 = \frac{2\pi}{a}\begin{pmatrix} 0 \\ 0 \\ 1 \end{pmatrix} \tag{2.34}$$

The reciprocal lattice vectors of the (110) facet

By using Eq. 2.32 one gets

$$V = \frac{a^3}{2} \tag{2.35}$$

and further

$$\mathbf{b}_1 = \frac{2\pi}{a}\begin{pmatrix} \sqrt{2} \\ 0 \\ 0 \end{pmatrix}, \ \mathbf{b}_2 = \frac{2\pi}{a}\begin{pmatrix} 0 \\ 1 \\ 0 \end{pmatrix}, \ \mathbf{b}_3 = \frac{2\pi}{a}\begin{pmatrix} 0 \\ 0 \\ \sqrt{2} \end{pmatrix} \tag{2.36}$$

The reciprocal lattice vectors of the (111) facet

By using Eq. 2.32 one gets

$$V = \frac{3}{4}a^3 \tag{2.37}$$

and further

$$\mathbf{b}_1 = \frac{2\pi}{a}\begin{pmatrix} 2\sqrt{\frac{2}{3}} \\ 0 \\ 0 \end{pmatrix}, \ \mathbf{b}_2 = \frac{2\pi}{a}\begin{pmatrix} \sqrt{\frac{2}{3}} \\ \sqrt{2} \\ 0 \end{pmatrix}, \ \mathbf{b}_3 = \frac{2\pi}{a}\begin{pmatrix} 0 \\ 0 \\ \frac{1}{\sqrt{3}} \end{pmatrix} \tag{2.38}$$

2.2.4 k-paths in the first Brillouin zone

The first Brillouin zone is the Wigner-Seitz cell in the reciprocal lattice. In Fig. 2.3, the Brillouin zone of a bulk fcc lattice is plotted. Commonly the band structure $E(\mathbf{k})$ is plotted by choosing representative **k**-paths within the BZ. The two red paths represent proper **k**-paths on the two-dimensional surface Brillouin zones. In general, paths are defined through **k**-points with a special symmetry, e.g. the most symmetric point Γ. **k**-points on the surface of the 3D-Brillouin zone, i.e. on a two-dimensional surface Brillouin zone, are denoted by an overline, e.g. $\overline{\Gamma}$.

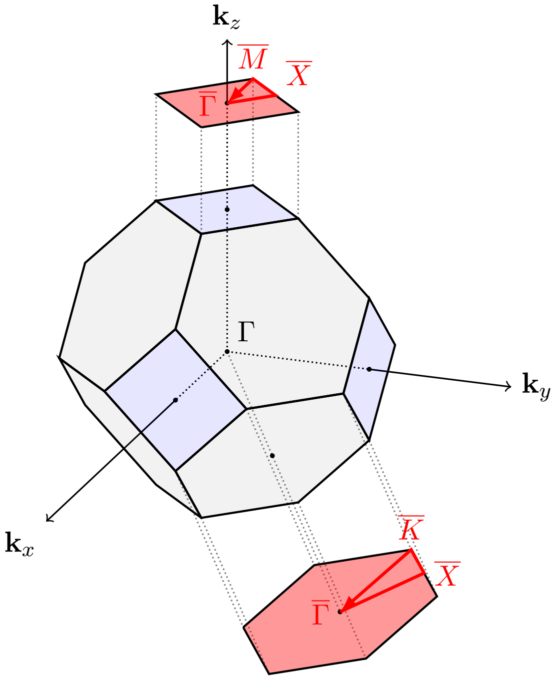

Figure 2.3: First Brillouin zone of the fcc lattice. In addition, the (001)-surface and the $(11\overline{1})$-surface.

The k-path on the k_x, k_y-surface of the Brillouin zone of the (100) facet.

By using Fig. 2.4 the **k**-points are

$$\overline{\Gamma} = 0,\ \overline{X} = \frac{1}{2}\mathbf{b}_1,\ \overline{M} = \frac{1}{2}\mathbf{b}_1 + \frac{1}{2}\mathbf{b}_2 \tag{2.39}$$

where the vectors $\mathbf{b}_i$ are taken from Eq. 2.34.

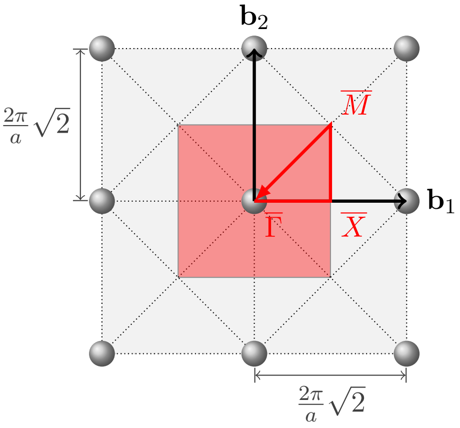

Figure 2.4: First Brillouin zone of the (100) facet.

The k-path on the k_x, k_y-surface of the Brillouin zone of the (110) facet.

By using Fig. 2.5 the **k**-points are

$$\overline{\Gamma} = 0,\ \overline{X} = \frac{1}{2}\mathbf{b}_1,\ \overline{S} = \frac{1}{2}\mathbf{b}_1 + \frac{1}{2}\mathbf{b}_2,\ \overline{Y} = \frac{1}{2}\mathbf{b}_2 \tag{2.40}$$

where the vectors $\mathbf{b}_i$ are taken from Eq. 2.36.

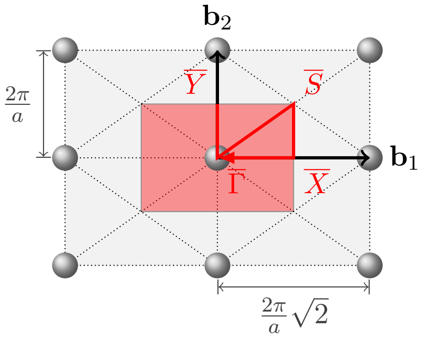

Figure 2.5: First Brillouin zone of the (110) facet.

The k-path on the k_x, k_y-surface of the Brillouin zone of the (111) facet.

By using Fig. 2.6 the **k**-points are

$$\overline{\Gamma} = 0,\ \overline{M} = \frac{1}{2}\mathbf{b}_1,\ \overline{K} = \frac{1}{3}\mathbf{b}_1 + \frac{1}{3}\mathbf{b}_2 \tag{2.41}$$

where the vectors $\mathbf{b}_i$ are taken from Eq. 2.38.

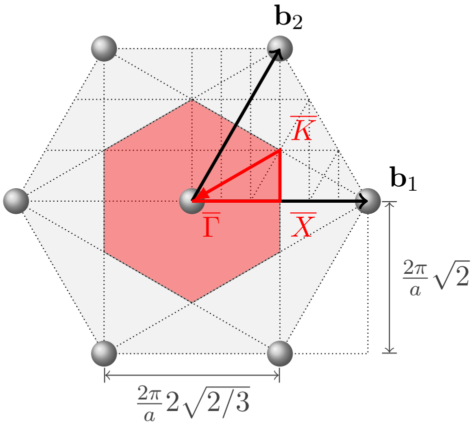

Figure 2.6: First Brillouin zone of the (111) facet.

2.3 Shockley surface states

A crystal surface violates the periodicity of the crystal lattice. Thus, in the direction perpendicular to the surface the fundamental theorem about periodicity of crystals, the theorem of Bloch, does not hold anymore. This allows for new solutions for the electron wavefunction. In the vicinity of the surface, the probability for such a new electron wavefunction is larger than apart from the surface. In other words one can say that the electron is more localized at the vicinity of the surface. Hence one denotes it as a surface state. On the contrary, a usual bulk wavefunction (a plane wave times a lattice periodic function) does not have this feature of the probability. A one-dimensional illustration of the lattice periodic potential of a crystal without and with a terminating surface is shown in Fig. 2.7a and 2.7b, respectively.
Recall Eq. 2.19 - the Schrödinger equation for an electron in a crystal

$$\Big(-\frac{\hbar^2}{2m}\nabla_{\mathbf{r}}^2+V(\mathbf{r})\Big)\psi_{n\mathbf{k}}(\mathbf{r})=E_n(\mathbf{k})\psi_{n\mathbf{k}}(\mathbf{r}). \tag{2.42}$$

Consider an infinite periodic one-dimensional lattice - see Fig. 2.7a. Then the Schrödinger equation simplifies to a one-dimensional form.

$$\Big(-\frac{\hbar^2}{2m}\frac{d^2}{dz^2}+V(\mathbf{z})\Big)\psi_{n\mathbf{k}}(z)=E_n(\mathbf{k})\psi_{n\mathbf{k}}(z) \tag{2.43}$$

One can apply

Bloch's theorem (in 1D): If $V(z+\zeta\cdot a)=V(z)$, with $\zeta\in\mathbb{Z}$, then the solutions are $\psi_{nk}(z)=u_{nk}(z)\exp\{ikz\}$, where $u_{nk}(z+\zeta\cdot a)=u_{nk}(z)$.

Note that the wavenumber $k\in\mathbb{R}$. Now consider a half-infinite periodic one-dimensional lattice - Fig. 2.7b. Due to the surface at $z=0$, the translational periodicity of the lattice is broken. This leads to the following ansatz for the wavefunctions [14]:

$$\psi_{nk}(z)=\begin{cases}Bu_{-nk}(z)\exp\{-ikz\}+Cu_{nk}(z)\exp\{ikz\} & \text{if } z<0\\ A\exp\{-\sqrt{2m(V_0-E)}\frac{z}{\hbar}\} & \text{if } z>0\end{cases} \tag{2.44}$$

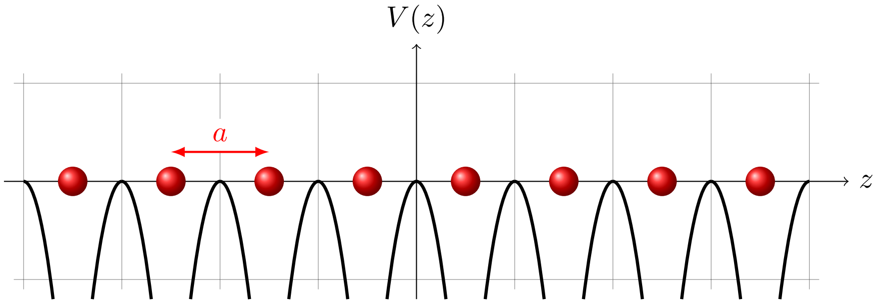

(a) An infinite 1D lattice.

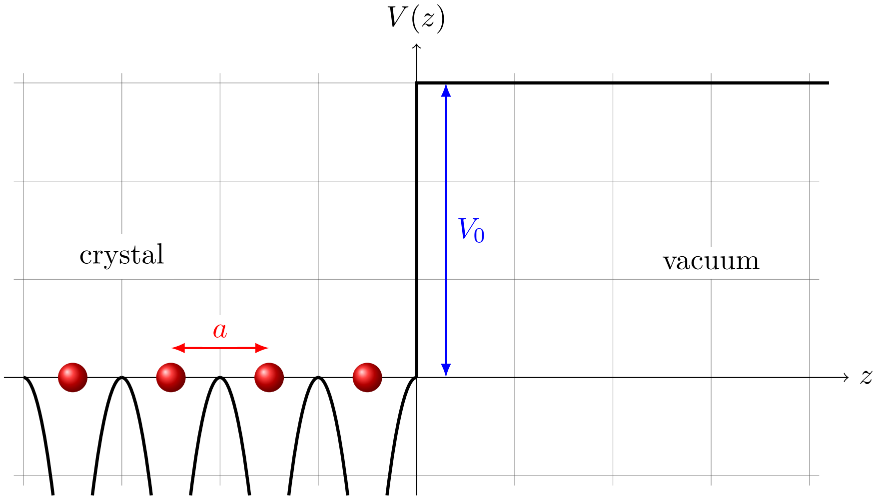

(b) A half-infinite 1D lattice.

Figure 2.7: A simple 1D lattice example.

The coefficients A, B, C are determined by the condition that ψ and ψ' must be continuous at $z = 0$ and be normalized. In contrast to the infinite 1D lattice, where $k \in \mathbb{R}$, in the half-infinite 1D lattice the wavenumber $k \in \mathbb{C}$. In this simple example there are two cases which lead to different types of the wavefunction - see Fig. 2.8.

Case 1: $\mathrm{Im}k = 0 \Longrightarrow$ bulk state - see Fig. 2.8a

Case 2: $\mathrm{Im}k \neq 0 \Longrightarrow$ surface state - see Fig. 2.8b

For the sake of completeness, it should be mentioned that there is the possibility of another state, the resonance state - see Fig. 2.8c, which, however, does not occur in this simplified example.

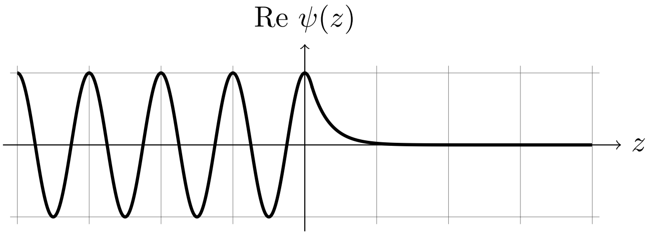

(a) Bulk state.

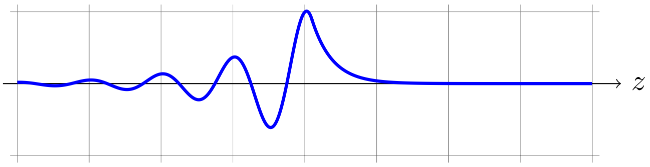

(b) Surface state.

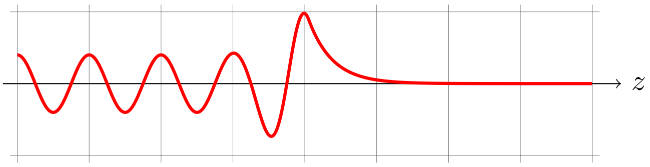

(c) Resonance state.

Figure 2.8: The different types of states at crystal surfaces.

2.4 The photoelectric effect

The photoelectric effect was experimentally discovered by Heinrich Hertz in 1887 and theoretically described by Albert Einstein in 1905. An electron of a solid can be emitted when a photon with energy $\hbar\omega$ is absorbed by the solid. This is the so-called photoelectric effect [15]. In this effect the work function Φ plays an important role. It determines the lower limit of the frequency of the photon - see Fig. 2.9. One can define this angular frequency limit ω_0 through $\Phi = \hbar\omega_0$. With that definition the range of the kinetic energy E_{kin} of the emitted electron can now be given with respect to the energy of the photon.

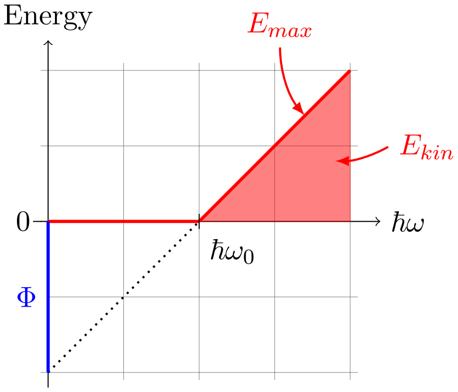

Figure 2.9: The lower limit of the frequency.

$$E_{kin} \in (0, E_{max}] \tag{2.45}$$

where $E_{max} = \hbar(\omega - \omega_0)$. If $\omega - \omega_0 < 0$ then the mechanism is not possible and the electron can not leave the solid.

3 Theory

In this chapter a brief introduction to density functional theory with the focus on the Kohn-Sham equations is given. Further, some standard methods for numerically solving the Kohn-Sham equations are introduced. Moreover, the problem that plane waves provide a poor description of the wave function close to atomic nuclei is considered. This has led to the invention of many methods, e.g. the pseudo-potential method, or the PAW method. A small selection of such methods, according to the simulation package which is used, is shortly introduced. After that, the concept of the supercell is brought up which provides a possibility to simulate a crystal surface. Finally, the calculation of the photoemission intensity via the one-step model is presented.

3.1 Density functional theory (DFT)

Usually when solving the Schrödinger equation, the external potential is given by the atomic nuclei. Thus, the external potential determines the wavefunction and thereby the electron density.

$$v_{\text{ext}}(\mathbf{r}) \Longrightarrow \psi(\mathbf{r}, \mathbf{r}_2, .., \mathbf{r}_N) \Longrightarrow n(\mathbf{r}) = N \int |\psi(\mathbf{r}, \mathbf{r}_2, .., \mathbf{r}_N)|^2 d^3r_2..d^3r_N \tag{3.1}$$

The question that may arises now is: is it conceptual possible to reverse this procedure and start from the electron density? At this point density functional theory comes into play which offers that possibility.

One can consider the Thomas-Fermi model, proposed in 1927, as a first density functional theory. Based on the uniform electron gas, they expressed the total classical energy of an atom in terms of the density only. Although, the model was historically important, its results are bad, since the kinetic energy is approximated in a poor manner.

After the Thomas-Fermi theory, it took more than 30 years until Hohenberg and Kohn showed that the electron density can be handled as the central quantity and an accurate computational scheme can be developed. The basis of DFT is provided by the [3]

First Hohenberg-Kohn theorem: A given electron density uniquely determines the (external) potential and hence the total energy of the system.

$$n(\mathbf{r}) \Longrightarrow v_{\text{ext}}(\mathbf{r}) \tag{3.2}$$

Proof by contradiction. Consider two many-electron systems with different external potentials $v' \neq v + \text{const}$.

System 1: $n, \psi, v, \hat{H}, E$

System 2: $n', \psi', v', \hat{H}', E'$

Assume that there is only one density for two different potentials.

$$n = n' \tag{3.3}$$

Using the variational principle - Eq. 2.11 - one has

$$E = \langle \psi | \hat{H} | \psi \rangle < \langle \psi' | \hat{H} | \psi' \rangle = \langle \psi' | \hat{H}' | \psi' \rangle + \int (v - v') n' d^3 r \tag{3.4}$$

$$E' = \langle \psi' | \hat{H}' | \psi' \rangle < \langle \psi | \hat{H}' | \psi \rangle = \langle \psi | \hat{H} | \psi \rangle + \int (v' - v) n d^3 r \tag{3.5}$$

Addition of these two inequalities gives

$$E + E' < E + E' + \int (v - v')(n' - n) d^3 r \tag{3.6}$$

$$0 < \int (v - v') \underbrace{(n' - n)}_{=0} d^3 r = 0 \tag{3.7}$$

where the assumption $(n' - n) = 0$ has been used, which leads to a contradiction. Hence, there can not exist two different potentials, apart from an additional constant, which lead to the same density □.

It is very surprising that the electron density already contains all physical informations of the system, but has $3(N-1)$ variables less than the N-electron-wavefunction.

Since the electron density is a fundamental characteristic of a many-electron system, it makes sense to write the total energy as a functional of the electron density. This is best done by the so-called 'constrained search' approach by Levy [16], which gives another opportunity to prove the first Hohenberg-Kohn theorem and further leads directly to their second theorem. The total energy functional can be obtained by minimizing $\langle \psi | \hat{H} | \psi \rangle$ over all many-electron wave functions ψ that yield a given electron density n. Denote this set of such ψ which yield the same density as

$$\{\psi \to n\} \equiv \left\{ \psi \in \mathcal{H} \middle| N \int |\psi(\mathbf{r}, \mathbf{r}_2, .., \mathbf{r}_N)|^2 d^3 r_2 .. d^3 r_N \right\} \tag{3.8}$$

The total energy functional

$$\begin{aligned} E[n] &= \min_{\{\psi \to n\}} \langle \psi | \hat{H} | \psi \rangle \\ &= \min_{\{\psi \to n\}} \langle \psi | \hat{T} + \hat{V}_{ee} + \hat{V}_{ext} | \psi \rangle \\ &= \min_{\{\psi \to n\}} \langle \psi | \hat{T} + \hat{V}_{ee} | \psi \rangle + \int v(\mathbf{r}) n(\mathbf{r}) d^3 r \end{aligned} \tag{3.9}$$

Thus, the total energy may be separated into a universal part

$$F[n] \equiv \min_{\{\psi \to n\}} \langle \psi | \hat{T} + \hat{V}_{ee} | \psi \rangle \tag{3.10}$$

which is the same for any system of N electrons, and, into a system-specific part, which contains the Coulomb energy of $n(\mathbf{r})$ in $\hat{V}_{ext}$. Now one can get the ground state energy by minimizing $E[n]$ with respect to n.

$$E_0 = \min_n E[n] = \min_n \Big(F[n] + \int v(\mathbf{r}) n(\mathbf{r}) d^3 r \Big) \tag{3.11}$$

Eq. 3.11 states the

Second Hohenberg-Kohn theorem: The density n_0 which minimizes the total energy is the ground state density.

Before a method for calculating (approximately) the ground state energy of a many particle system is considered, the total energy functional is separated into suitable parts.

$$\begin{aligned} E[n] &= F[n] + V[n] \\ &= T[n] + V_{ee}[n] + V[n] \\ &= T_s[n] + V_H[n] + (T[n] - T_s[n]) + (V_{ee}[n] - V_H[n]) + V[n] \end{aligned} \tag{3.12}$$

where $T_s[n]$ is the kinetic energy of non-interacting particles. For a non-interacting system the universal part reduces to

$$F[n] \mapsto T_s[n] = \min_{\psi \to n} \langle \psi | \hat{T} | \psi \rangle \tag{3.13}$$

One can define the so-called **exchange-correlation-energy** via

$$E_{xc}[n] \equiv \Big(T[n] - T_s[n] \Big) + \Big(V_{ee}[n] - V_H[n] \Big) \tag{3.14}$$

The exchange part of it is due to the Pauli principle and the correlation part is due to correlations. Now the total energy can be rewritten

$$F[n] = T_s[n] + V_H[n] + E_{xc}[n] \tag{3.15}$$

where

$$V_H[n] = \frac{1}{2} \int \int \frac{n(\mathbf{r}) n(\mathbf{r}')}{|\mathbf{r} - \mathbf{r}'|} d^3 r d^3 r' \tag{3.16}$$

is the Hartree energy, which describes the classical part of the electron-electron repulsion. The external potential energy $V[n]$ contains the electron-core-interaction plus another possible potential V_0, e.g. an external electric field.

$$V[n] = \int v_0(\mathbf{r}) d^3 r + \sum_\alpha \int \frac{Z_\alpha n(\mathbf{r})}{|\mathbf{R}_\alpha - \mathbf{r}|} d^3 r \tag{3.17}$$

3.1.1 Kohn-Sham equations

Although the Hohenberg-Kohn theorems, published in 1964, are rather important and powerful and give some insights to quantum physics, they unfortunately do not provide a way of calculating the ground state energy. In order to derive a scheme that can be applied in practice, in 1965 Kohn and Sham suggested to consider a non-interacting system of electrons [4], i.e. $\hat{V}_{ee} = 0$, which leads to the same density as the corresponding physical system. For a non-interacting electron system each electron obeys a one-particle Schrödinger equation

$$\Big(-\frac{1}{2}\Delta + v_s([n];\mathbf{r})\Big)\phi_k(\mathbf{r}) = \epsilon_k \phi_k(\mathbf{r}) \tag{3.18}$$

the so-called Kohn-Sham equations [4]. The wavefunctions ϕ_k are the so-called Kohn-Sham orbitals. The important trick is do define the potential v_s such that the Kohn-Sham system yields the same density as the corresponding physical system. This can be achieved by choosing

$$v_s([n];\mathbf{r}) = v_{\text{ext}}([n];\mathbf{r}) + v_H([n];\mathbf{r}) + v_{xc}([n];\mathbf{r}) \tag{3.19}$$

where

$$v_H([n];\mathbf{r}) = \frac{\delta V_H[n]}{\delta n(\mathbf{r})} = \int \frac{n(\mathbf{r}')}{|\mathbf{r}-\mathbf{r}'|} d^3r' \tag{3.20}$$

and

$$v_{\text{ext}}([n];\mathbf{r}) = \frac{\delta V[n]}{\delta n(\mathbf{r})} = v_0(\mathbf{r}) + \sum_\alpha \frac{Z_\alpha}{|\mathbf{R}_\alpha - \mathbf{r}|} \tag{3.21}$$

can be explicitly given in terms of the electron density while the exchange-correlation energy per volume

$$v_{xc}([n];\mathbf{r}) = \frac{\delta E_{xc}[n]}{\delta n(\mathbf{r})} \tag{3.22}$$

needs to be approximated in an appropriate manner. The Kohn-Sham equations have to be solved in a self-consistent way - see Fig. 3.1. Mathematically the Kohn-Sham equations describe a non-interacting system hence the probabilities $|\phi_k|^2$ are independent. In this case the electron density is simply the sum over these probabilities

$$n(\mathbf{r}) = \sum_{\mathbf{k}\in \text{BZ}} \sum_{n}^{\text{occ}} |\phi_{n\mathbf{k}}(\mathbf{r})|^2 \tag{3.23}$$

where the first summation is over all **k**-points in the Brillouin zone and the second summation is over the occupated states only.

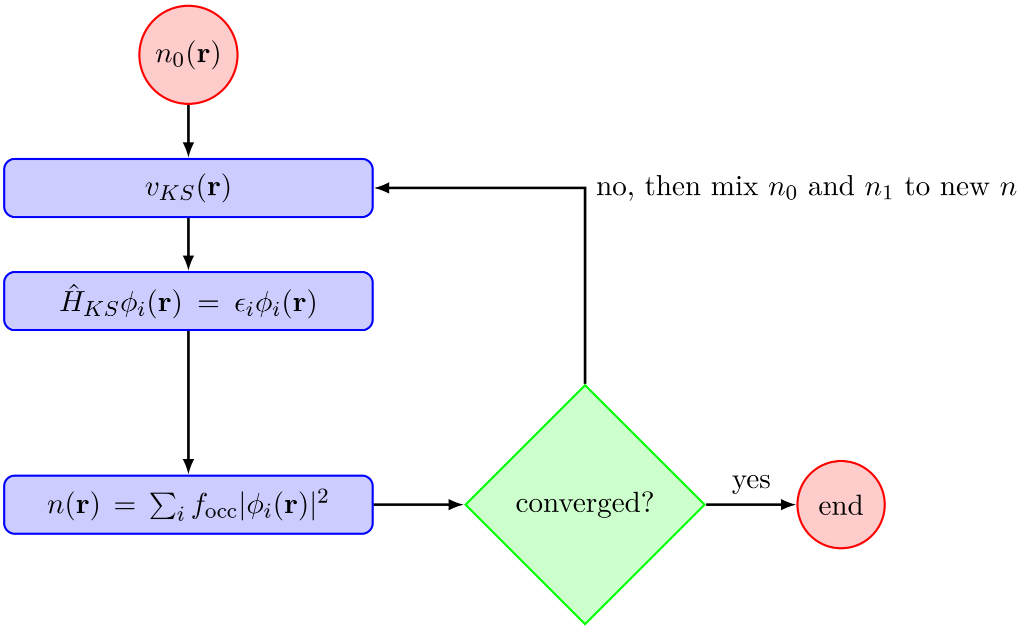

Figure 3.1: The self-consistent algorithm for solving the Kohn-Sham equations.

3.1.2 Exchange-correlation energy

The main difficulty of DFT is to find good approximations for the exchange-correlation energy functional $E_{xc}[n]$. There are many approximations, e.g. the local-density approximation (LDA).

$$E_{xc}^{\text{LDA}}[n] = \int e_{xc}^{unif}(n(\mathbf{r}))d^3r \tag{3.24}$$

where $e_{xc}^{unif}(n(\mathbf{r})) = e_x^{unif}(n) + e_c^{unif}(n)$ is the exchange-correlation energy per volume of a uniform electron gas with the electron density $n(\mathbf{r})$. The exchange energy of a uniform electron gas $e_x^{unif} \propto n^{4/3}$ can be derived via uniform coordinate scaling [10]. The correlation energy of a uniform electron gas is not known exactly, hence approximations are needed. Usually one uses the following expression [10]

$$e_c^{unif}(n) = -2c_0(1 + \alpha_1 r_s)\ln\left[1 + \frac{1}{2c_0(\beta_1 r_s^{1/2} + \beta_2 r_s + \beta_3 r_s^{3/2} + \beta_4 r_s^2)}\right] \tag{3.25}$$

where

$$\beta_1 = \frac{1}{2c_0}\exp\left(-\frac{c_1}{2c_0}\right), \tag{3.26}$$

$\beta_2 = 2c_0\beta_1^2$, and the constants $c_0 = 0.031091$ and $c_1 = 0.046644$. The parameter $r_s = \left(\frac{3}{4\pi n}\right)^{1/3}$ is the Wigner-Seitz radius, the radius of a sphere which on average contains one electron. The other constants $\alpha_1 = 0.21370$, $\beta_3 = 1.6382$, and $\beta_4 = 0.49294$ are determined via fits within Quantum Monte Carlo methods. The LDA forms the basis of all other ab inito exchange-correlation functional approximations.

In this thesis, a generalized gradient approximation (GGA) is used - to be more precise, the GGA-PBE [5, 6], which is named after its authors John P. Perdew, Kieron Burke, and Matthias Ernzerhof. In contrast to LDA, in the GGA the gradient of the density is taken into account. A generalized gradient approximation can be written as [10]

$$E_{xc}^{\mathrm{GGA}}[n] = E_x^{\mathrm{GGA}}[n] + E_c^{\mathrm{GGA}}[n] = \int f(n(\mathbf{r}), \nabla n(\mathbf{r})) d^3r \tag{3.27}$$

The exchange energy is given by

$$E_x^{\mathrm{GGA}}[n] = A_x \int n^{4/3} F_x(s) d^3r \tag{3.28}$$

where A_x is a constant and

$$F_x(s) = 1 + \kappa - \frac{\kappa}{1 + \mu s^2/\kappa} \tag{3.29}$$

is a function of the reduced density gradient $s = \frac{|\nabla n|}{2k_F n} = \frac{|\nabla n|}{2(3\pi)^{1/3} n^{4/3}}$ with the Fermi wavenumber k_F and a constant $0 \leq \kappa \leq 0.804$ to satisfy the Lieb-Oxford bound. Note, that for a constant density $E_x^{\mathrm{GGA}}\Big|_{s=0} = E_x^{\mathrm{LDA}}$. The correlation energy is given by

$$E_c^{\mathrm{GGA}}[n_\uparrow, n_\downarrow] = \int n_\downarrow \Big(e_c(r_s, \zeta) + H(r_s, \zeta, t) \Big) d^3r \tag{3.30}$$

where $n_\uparrow, n_\downarrow$ are the spin densities and e_c is the correlation energy per electron of the uniform electron gas. Further one has another reduced density gradient $t = \frac{|\nabla n|}{2k_s n}$ with the Thomas-Fermi-wavenumber k_s and the relative spin polarization $\zeta = \frac{n_\uparrow - n_\downarrow}{n_\uparrow + n_\downarrow}$. The additional function in the integral of Eq. 3.30 is

$$H(r_s, \zeta, t) = c_0 \phi^3(\zeta) \ln \left(1 + \frac{\beta_{MB}}{c_0} t^2 \Big[\frac{1 + At^2}{1 + At^2 + A^2 t^4} \Big] \right) \tag{3.31}$$

where $\beta_{MB} = 0.066725$ is calculated via the high-density limit,

$$\phi = \frac{1}{2} \Big[(1 + \zeta)^{2/3} + (1 - \zeta)^{2/3} \Big] \tag{3.32}$$

and

$$A = \frac{\beta_{MB}}{c_0} \frac{1}{\exp[-e_c(r_s, \zeta)/c_0 \phi^3]} \tag{3.33}$$

3.2 DFT in practice

The algorithm in Fig. 3.1 provides a scheme to solve the Kohn-Sham equations in a self-consistent way. In this section, the concept of writing the Kohn-Sham equations as a matrix equation is introduced. For that a set of basis functions has to be choosen. The case of plane waves as basis functions is explicitly described. Further, a pseudo-potential method and the PAW method are introduced. Pseudo potentials and the PAW method are used within the simulation package VASP, which afterwards is overviewed in this section. Finally, a concept of simulating crystal surfaces is introduced.

3.2.1 The Kohn-Sham equations as a matrix eigenvalue problem

The Kohn-Sham equations for a translationally periodic potential are

$$\hat{H}\phi_{\mathbf{k}}(\mathbf{r}) = \epsilon(\mathbf{k})\phi_{\mathbf{k}}(\mathbf{r}). \tag{3.34}$$

Motivated by Bloch's theorem, the wavefunction $\phi_{\mathbf{k}}(\mathbf{r})$ can be written as a linear expansion

$$\phi_{\mathbf{k}}(\mathbf{r}) = e^{i\mathbf{k}\cdot\mathbf{r}} \underbrace{\sum_j c_j(\mathbf{k})\varphi_j(\mathbf{r})}_{u_{\mathbf{k}(\mathbf{r})}} \tag{3.35}$$

with a set of lattice-periodic basis functions $\varphi_j(\mathbf{r}+\mathbf{R}) = \varphi_j(\mathbf{r})$. Plugging this expansion into Eq. 3.34 one obtains

$$\sum_j H_{ij}(\mathbf{k})c_j(\mathbf{k}) = \epsilon(\mathbf{k})\sum_j S_{ij}(\mathbf{k})c_j(\mathbf{k}), \tag{3.36}$$

the so-called secular equation, where the Hamiltonian matrix elements are the following integrals over the cell volume Ω

$$H_{ij}(\mathbf{k}) = \int_\Omega \varphi_i^*(\mathbf{r})e^{-i\mathbf{k}\cdot\mathbf{r}}\hat{H}e^{i\mathbf{k}\cdot\mathbf{r}}\varphi_j(\mathbf{r})d^3r, \tag{3.37}$$

and the overlap matrix elements are

$$S_{ij}(\mathbf{k}) = \int_\Omega \varphi_i^*(\mathbf{r})\varphi_j(\mathbf{r})d^3r. \tag{3.38}$$

Plane wave basis set.

It is convenient to choose plane waves for the basis functions.

$$\varphi_j(\mathbf{r}) \equiv \varphi_{\mathbf{G}}(\mathbf{r}) = \frac{1}{\sqrt{\Omega}}e^{i\mathbf{G}\cdot\mathbf{r}} \tag{3.39}$$

Then Eq. 3.35 becomes

$$\phi_{\mathbf{k}}(\mathbf{r}) = \frac{1}{\sqrt{\Omega}}e^{i\mathbf{k}\cdot\mathbf{r}}\sum_{\mathbf{G}} c_{\mathbf{G}}(\mathbf{k})e^{i\mathbf{G}\cdot\mathbf{r}} \tag{3.40}$$

To fulfill the lattice-periodicity, **G** must be a point of the reciprocal lattice. For a plane wave basis set, the overlap matrix elements are simply the Kronecker deltas

$$S_{\mathbf{G}\mathbf{G}'} = \frac{1}{\Omega}\int_{\Omega} e^{-i\mathbf{G}\cdot\mathbf{r}} e^{i\mathbf{G}'\cdot\mathbf{r}} d^3r = \delta_{\mathbf{G}\mathbf{G}'} \tag{3.41}$$

and the Hamiltonian matrix element is

$$H_{\mathbf{G}\mathbf{G}'}(\mathbf{k}) = \frac{1}{2}(\mathbf{k}+\mathbf{G})^2\delta_{\mathbf{G}\mathbf{G}'} + \frac{1}{\Omega}\int_{\Omega} V(\mathbf{r}) e^{-i(\mathbf{G}-\mathbf{G}')\mathbf{r}} d^3r \tag{3.42}$$

Eq. 3.36 becomes

$$\sum_{\mathbf{G}'} H_{\mathbf{G}\mathbf{G}'}(\mathbf{k}) c_{\mathbf{G}'}(\mathbf{k}) = \epsilon(\mathbf{k}) c_{\mathbf{G}}(\mathbf{k}) \tag{3.43}$$

This eigenvalue equation represents the Kohn-Sham equations in a plane wave expansion. In principle the expansion in plane waves includes a summation over an infinite number of **G** vectors. For numerical applications, one has to make a cut-off. The cut-off is defined through the maximal energy of the plane waves

$$E_{\text{cutoff}} = \frac{1}{2}G^2_{\text{max}}. \tag{3.44}$$

The numerical expansion of the wavefunction is

$$\phi_{\mathbf{k}}(\mathbf{r}) = \frac{1}{\sqrt{\Omega}} e^{i\mathbf{k}\cdot\mathbf{r}} \sum_{\mathbf{G}}^{|\mathbf{k}+\mathbf{G}|\leq G_{\text{max}}} c_{\mathbf{G}}(\mathbf{k}) e^{i\mathbf{G}\cdot\mathbf{r}} \tag{3.45}$$

3.2.2 Pseudo-potential

The Kohn-Sham equations describe all electron states including the core states. When investigating systems where the unit cell contains several atoms, the number of electrons will be rather large. In this case a big effort has to be made to compute such systems. Particularly, when expanding the wavefunction of a notably localized electron into plane waves [1]. At this point, one can distinguish between core electrons and valence electrons. A rough description is that the core electrons are tightly bound (localized) to the nuclei, while the valence electrons are not localized. In the

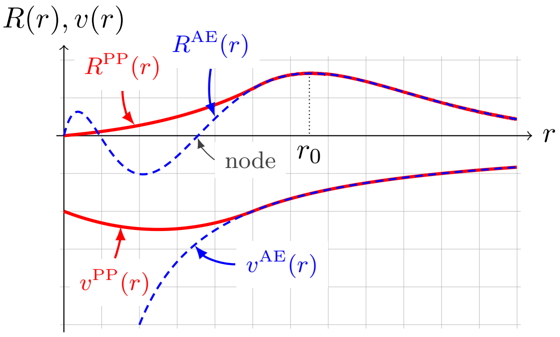

Figure 3.2: Example of a pseudo-potential.

---

[1] Typically, electrons localized near nuclei are well-described by a product of a few spherical harmonics and radial wavefunctions. Unfortunately, their plane-wave expansion has a poor convergence.

pseudo-potential method one consider the valence electrons only. Nevertheless, the core electrons have to be taken into account. Since the core electrons are localized close to the nuclei, it is convenient to treat them together as ions. In order to obtain frozen ions, i.e. the ions have no dynamics, one has to introduce the so-called frozen-core-approximation. Within this approximation the core electrons contribute to the effective potential of the ions.

The aim of the pseudo-potential method is, that a valence wavefunction is represented by a smooth function (the so-called pseudo wavefunction) $|\phi_v\rangle$, to avoid the exhaustive use of plane waves. Usually a plane wave is not orthogonal to a core wavefunction and hence the pseudo wavefunctions need to be orthogonalized. Let $|\psi_c\rangle$ be the core wavefunctions and let $|\psi_v\rangle$ be the valence wavefunctions. The connection between a pseudo wavefunction and the corresponding valence wavefunction can be achieved via [10, 12]

$$|\psi_v\rangle = \Big(1 - \sum_c |\psi_c\rangle\langle\psi_c|\Big)|\phi_v\rangle \tag{3.46}$$

where the coefficients $\langle\psi_c|\phi_v\rangle$ guarantee the orthogonality of the valence states to the core states. The Kohn-Sham equation for $|\phi_v\rangle$ is

$$\begin{aligned} \hat{H}|\psi_v\rangle &= \epsilon_v|\psi_v\rangle \\ \hat{H}|\Big(1 - \sum_c |\psi_c\rangle\langle\psi_c|\Big)|\phi_v\rangle &= \epsilon_v\Big(1 - \sum_c |\psi_c\rangle\langle\psi_c|\Big)|\phi_v\rangle \\ \hat{H}|\phi_v\rangle - \sum_c \langle\psi_c|\phi_v\rangle \underbrace{\hat{H}|\psi_c\rangle}_{=\epsilon_c|\psi_c\rangle} &= \epsilon_v|\phi_v\rangle - \sum_c \langle\psi_c|\phi_v\rangle\epsilon_v|\psi_c\rangle \\ \Rightarrow \underbrace{\Big(\hat{H} - \sum_c (\epsilon_c - \epsilon_v)|\psi_c\rangle\langle\psi_c|\Big)}_{\equiv \hat{H}_{\text{pseudo}}} |\phi_v\rangle &= \epsilon_v|\phi_v\rangle \end{aligned} \tag{3.47}$$

where $\hat{H}_{\text{pseudo}}$ is the Pseudo-Hamiltonian and $|\phi_v\rangle$ is the Pseudo-wavefunction.

Pseudo-Potential construction

The general construction of a first-principle norm-conserving pseudo-potential according to the recipe of Troullier and Martins [17, 10] involves the following steps:

(1) Solve self-consistently the free atom all-electron (AE) radial Kohn-Sham equation

$$\left(-\frac{1}{2}\frac{d^2}{dr^2} + \frac{l(l+1)}{2r^2} + v_{\text{KS}}^{\text{AE}}[n^{\text{AE}}](r) \right) rR_{nl}^{\text{AE}}(r) = \epsilon_{nl}^{\text{AE}} rR_{nl}^{\text{AE}}(r) \tag{3.48}$$

where

$$v_{\text{KS}}^{\text{AE}}[n^{\text{AE}}](r) = -\frac{Z}{r} + v_{\text{H}}[n^{\text{AE}}](r) + v_{\text{xc}}[n^{\text{AE}}](r) \tag{3.49}$$

(2) Choose a proper cutoff radii r_0 which is at least larger than any node-position of the all-electron wavefunction.

(3) Normalization conditions for the ansatz for the PP-wavefunction $R_l^{\mathrm{PP}}(r)$

- if $r > r_0$ then $R_l^{\mathrm{PP}}(r) = R_l^{\mathrm{AE}}(r)$
- if $r < r_0$ then $\int_0^{r_0} |R_l^{\mathrm{PP}}(r)|^2 r^2 dr = \int_0^{r_0} |R_l^{\mathrm{AE}}(r)|^2 r^2 dr$

(4) Inversion of Eq. 3.48 yields the screened pseudo-potential.

$$v_{\mathrm{scr},l}^{\mathrm{PP}}(r) = \epsilon_l^{\mathrm{PP}} - \frac{l(l+1)}{2r^2} + \frac{1}{2rR_l^{\mathrm{PP}}(r)} \frac{d^2}{dr^2}\left(rR_l^{\mathrm{PP}}(r)\right) \tag{3.50}$$

(5) Remove screening effects

$$v_l^{\mathrm{PP}}(r) = v_{\mathrm{scr},l}^{\mathrm{PP}}(r) - v_{\mathrm{H}}[n^{\mathrm{AE}}](r) - v_{\mathrm{xc}}[n^{\mathrm{AE}}](r) \tag{3.51}$$

An example for the radial wavefunctions $R_l^{\mathrm{AE}}(r)$ and $R_l^{\mathrm{PP}}(r)$ and the corresponding potentials are given in Fig. 3.2. A pseudo wavefunction must not have any nodes. It also must not change the charge of the ion because then the properties of scattering processes would be modified. A typical ansatz for the pseudo wavefunction is a sum of even polynomial functions or a sum of spherical Bessel functions.

3.2.3 PAW-method

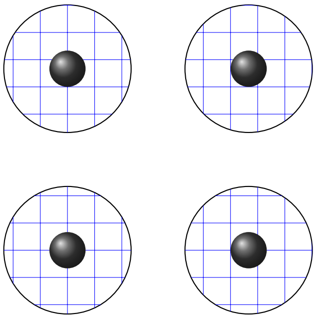

Figure 3.3: The augmented regions in the vicinity of the nuclei.

Usually electronic wavefunctions have strong oscillations near the nuclei, while auxiliary wavefunctions, e.g. pseudo wavefunctions, have no oscillations in the vicinity of the nuclei. As already mentioned when expanding a wavefunction into plane waves with a given accuracy, the physical (all-electron) wavefunction needs much more plane waves than a pseudo (valence-electron) wavefunction. However, due to the fact that for pseudo wavefunctions the number of nodes in the vicinity of the nuclei is not correct, pure pseudo-potential methods lead to some physically wrong results. An aim would be to have a combination of physical correct results such as in all-electron theories and a numerically fast performance such as in pseudo-potential methods. Accordingly, the projector augmented wave (PAW) method [18] combines advantages of the pseudo-potential method and all-electron methods such as the LAPW-method. In this method one has the real, physical wavefunction $|\psi\rangle$ and an auxiliary wavefunction (a pseudo wavefunction) $|\tilde{\psi}\rangle$ both for the valence electrons.

In the PAW method space is divided into two regions - see Fig. 3.3. One type of region is in the vicinity of the nuclei, the so-called augmentation regions Ω_α around each ion at the positions $\mathbf{R}_\alpha$. The second type of region is formed by the disjoint of the first type. In the second type of region, the wavefunctions $|\psi\rangle = |\tilde{\psi}\rangle$. In the vicinity of the nuclei the auxiliary wavefunction is different to the physical wavefunction.

In order to switch between both wavefunctions, a linear transformation $\mathcal{T}$ maps the auxiliary wavefunction onto the real wavefunction.

$$|\psi\rangle = \mathcal{T}|\tilde{\psi}\rangle \tag{3.52}$$

Since there is only a difference inside the augmentation regions, the transformation can be written

$$\mathcal{T} = 1 + \sum_{\alpha} \hat{\mathcal{T}}_{\alpha} \tag{3.53}$$

When applying $\hat{\mathcal{T}}_{\alpha}$ onto the auxiliary wavefunction, it gives a contribution inside the augmented region Ω_{α} around the ion at $\mathbf{R}_{\alpha}$ only. The expansion of the auxiliary wavefunction within Ω_{α} into partial waves $|\tilde{\phi}_i\rangle$, i.e. plane waves, reads

$$|\tilde{\psi}\rangle = \sum_{i} |\tilde{\phi}\rangle c_i \tag{3.54}$$

The coefficients are

$$c_i = \langle \tilde{p}_i | \tilde{\psi}\rangle \tag{3.55}$$

where $|\tilde{p}_i\rangle$ are the so-called projector functions. In each augmented region Ω_{α}

$$\langle \tilde{p}_i | \tilde{\phi}_j \rangle = \delta_{ij} \tag{3.56}$$

The linear transformation $\mathcal{T}$ can be written as

$$\mathcal{T} = 1 + \sum_{i} (|\phi_i\rangle - |\tilde{\phi}_i\rangle)\langle \tilde{p}_i|. \tag{3.57}$$

The physical wavefunction can thus be obtained from the auxiliary wave functions in the following way

$$|\psi\rangle = |\tilde{\psi}\rangle - \sum_{i} |\tilde{\phi}_i\rangle\langle \tilde{p}_i|\tilde{\psi}\rangle + \sum_{i} |\phi_i\rangle\langle \tilde{p}_i|\tilde{\psi}\rangle. \tag{3.58}$$

The first summation term subtracts the auxiliary parts of the wavefunction inside the augmented regions. The second summation term adds the physical parts of the wavefunction inside the augmented regions.

As the wavefunctions, all other quantities, e.g. the electron density and the total energy, can be transformed between the physical and the auxiliary representation. Each quantity Q consists of its auxiliary representation $\tilde{Q}$, minus the projected augmentation auxiliary part $\tilde{Q}^1$, and plus the projected augmentation physical part Q^1.

$$Q = \tilde{Q} - \tilde{Q}^1 + Q^1 \tag{3.59}$$

The representation of an arbitrary local operator $\mathcal{A}$ reads

$$\tilde{\mathcal{A}} = \mathcal{T}^{\dagger}\mathcal{A}\mathcal{T} = \mathcal{A} + \sum_{i,j} |\tilde{p}_i\rangle \left(\langle \phi_i|\mathcal{A}|\phi_j\rangle - \langle \tilde{\phi}_i|\mathcal{A}|\tilde{\phi}_j\rangle \right) \langle \tilde{p}_j| \tag{3.60}$$

For example the electron density is given by

$$\langle \psi|\mathbf{r}\rangle\langle\mathbf{r}|\psi\rangle = \langle \tilde{\psi}|\mathbf{r}\rangle\langle\mathbf{r}|\tilde{\psi}\rangle + \sum_{i,j} \langle \tilde{\psi}|\tilde{p}_i\rangle \left(\langle \phi_i|\mathbf{r}\rangle\langle\mathbf{r}|\phi_j\rangle - \langle \tilde{\phi}_i|\mathbf{r}\rangle\langle\mathbf{r}|\tilde{\phi}_j\rangle \right) \langle \tilde{p}_j|\tilde{\psi}\rangle \tag{3.61}$$

3.2.4 Vienna ab initio simulation package (VASP)

Within this thesis, the Vienna ab Initio Simulation Package (VASP), written in Fortran, has been used. VASP solves the Kohn-Sham equations using a plane wave basis set with periodic boundary conditions [19, 20, 21, 22]. Moreover a Hartree-Fock method, a many-body perturbation method, and a Green's function method is available.

Now a brief introduction into performing a calculation with VASP is given. There are four input files, which are necessary when executing VASP, the file 'INCAR', the file 'KPOINTS', the file 'POSCAR', and the file 'POTCAR'.

INCAR In the INCAR file one can declare possible parameters of the calculation, e.g. the global break condition (which determines when the Kohn-Sham algorithm stops) via the tag EDIFF. For almost any parameter there are default values, e.g. EDIFF=E-04. In Tabs. 3.1 and 3.2 a selection of tags are described.

An example of an INCAR file for a self-consistent computation of the Kohn-Sham-equations is given below.

```
SYSTEM=Al bulk

#precision of calculation
PREC=Accurate
ENCUT=400           # plane wave cut-off in eV
EDIFF=1E-8          # total energy scf-criterion

#make DOSCAR file
ISMEAR=1            # switch for the type of smearing
SIGMA=0.1           # width of the smearing in eV
EMIN=-20            # lower boundary of the energy range for DOS
EMAX=20             # upper boundary of the energy range for DOS
NEDOS=1001          # number of grid points for the DOS
LORBIT=10           # DOS is written into the file DOSCAR

#make LOCPOT file
LVHAR=.TRUE.        # write potential into the file LOCPOT
```

The SYSTEM tag allows to add a comment, e.g. what system is calculated. The tags PREC, ENCUT, and EDIFF determine the accuracy of the calculation. The tag LORBIT determines that a file with the density of states should be generated and the tags ISMEAR, SIGMA, EMIN, EMAX, and NEDOS state how the DOS should be computed.

Another example of an INCAR file for the non-self-consistent calculation of the energy eigenvalues of a choosen **k**-path to plot a bandstructure is shown below.

```
SYSTEM=$system_name bulk

#precision of calculation
PREC=Accurate
ENCUT=400             # plane wave cut-off in eV
EDIFF=1E-8            # total energy scf-criterion
```

```

#read from previous computed WAVECAR file
ISTART=1
#non-selfconsistent calculation
ICHARG=11
```

The tags ISTART=1 and ICHARG=11 states that no self-consistent calculations are performed and the orbitals and the density has to be read from the files WAVECAR and CHGCAR from a previous self-consistent calculation.

Table 3.1: A list of VASP-tags for the INCAR file.

Tags for a usual Kohn-Sham run.

SYSTEM	For comments, e.g. the name of the system.
PREC	Defines precision mode of calculation. Roughly, one can choose between accuracy and speed. Possible values are 'Low | Medium | High | Normal | Single | Accurate'.
EDIFF	Global break condition: If the total energy difference and the eigenvalue difference between two Kohn-Sham steps are both smaller than EDIFF then the Kohn-Sham algorithm stops.
NELMIN	Minimum number of Kohn-Sham iterations. Default value is 2.
NELM	Maximum number of Kohn-Sham iterations. Default value is 60.
ENCUT	Cut-off energy.
NBANDS	Number of energy bands in the calculation. There should be always some unoccupied bands in the calculation.

Tags for computing the density of states.

EMIN	Lower boundary of the energy range for the calculation of the DOS
EMAX	Upper boundary of the energy range for the calculation of the DOS
NEDOS	Number of grid points on which the DOS is evaluated.
ISMEAR	Determines how the occupacies of the orbitals are set.
SIGMA	Width of the smearing in eV. In theory the occupation curve is the Fermi-Dirac-distribution at $T = 0$ which is a step function. To handle with a smoother curve, one introduces via the parameter SIGMA a 'computational' temperature above zero.

KPOINTS When calculating the density, an integral over the Brillouin zone has to be performed. In numerical applications one uses a finite set of proper **k**-points, e.g. a grid of **k**-points. The file KPOINTS defines these **k**-points. A simple example for automatically generating a **k**-mesh is given below.

```
Automatic mesh
0
Monkhorst-Pack
3  3  3          # 3x3x3 k-points
0. 0. 0.         # global shift of all k-points
```

The first line is a comment line for the user only. The second line contains the number of k-points with the exception of the number 0, which activates an automatic generation scheme. For the automatic generation scheme, the first character of the third line specifies the generation method, here the 'M' of the so-called Monkhorst-Pack [23]. The only two possible characters are 'M' and 'G'. Both generate a mesh-grid, the latter generates a centered one at the Γ point. The three positive integer numbers at line four determines the number of points along the reciprocal lattice vectors $\mathbf{b}_1$, $\mathbf{b}_2$, and $\mathbf{b}_3$. Line five offers a global shift of all **k**-points. Another example for entering **k**-points for a **k**-path is given below.

```
1   kpoints for bandstructure G-M-K-G
2   10                              # number of k-points of one line
3   Line                            # switch to line mode
4   Reciprocal                      # reciprocal coordinate mode
5
6    0.00000 0.00000 0.00000 1     # Gamma
7    0.50000 0.00000 0.00000 1     # M
8
9    0.50000 0.00000 0.00000 1     # M
10   0.33333 0.33333 0.00000 1     # K
11
12   0.33333 0.33333 0.00000 1     # K
13   0.00000 0.00000 0.00000 1     # Gamma
```

VASP will generate 10 equidistant points between the **k**-points $(0,0,0)$ and $(0.5,0,0)$, 10 equidistant points between $(0.5,0,0)$ and $(0.33333,0.33333,0)$, and 10 equidistant points between $(0.33333,0.33333,0)$ and $(0,0,0)$. The first character of line three 'L' switches to this line scheme. The first character of line four 'R' states that the **k**-points below are given in units of the reciprocal lattice vectors. Otherwise one can use the Cartesian mode with the character 'C'. Then the **k**-points are given in units of $2\pi/a$, where a is the lattice constant.

POSCAR This file contains the lattice vectors and the positions of the ions in the cell. A simple example for a POSCAR files is given below.

```
1   Cu-fcc
2    3.61              # scaling factor
3    0.00 0.50 0.50    # first lattice vector
4    0.50 0.00 0.50    # second lattice vector
5    0.50 0.50 0.00    # third lattice vector
6    Cu
7    1                 # number of ions
8   Direct             # direct coordinate mode
9   0 0 0              # position of ion
```

Again, the first line is a comment line for the user only. The number in the second line is a scaling factor, usually 1 or the lattice constant in Å. Lines three to five define the lattice vectors. Their values has to be multiplied by the scaling factor from line two. In line six, one can specify the atomic types, here 'Cu' for copper. For more than one species, one has to separate them by the space character, e.g. 'Cu H O'. In line seven, the number of ions are given. For more than one species, again one has to separate them by the space character, e.g. '4 2 1'. The first character of line eight 'D' states that the positions of the ions are given in units of the lattice vectors. Otherwise one can use the Cartesian mode via 'C'. Then the coordinates of the ions, here only one ion, are written in the further lines.

POTCAR This file contains pseudopotentials of an atomic species. Moreover, the file contains constants such as the atomic mass, the number of valence electrons, and others. If more than one species is used, then one has to concatenate the corresponding POTCAR files in the right order. The same order has to be taken as specified in the 'POSCAR' file. Fortunately, one does not need to generate a POTCAR file by oneself, which would of course exceed the scope of this thesis, since the VASP community offers a whole collection of POTCAR files for all elements in the periodic table.

Table 3.2: A further list of VASP-tags for the INCAR file.

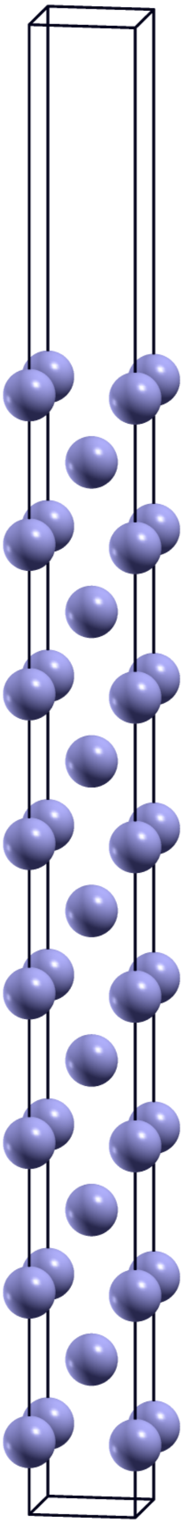

Figure 3.4: Supercell.

Tags for a ionic relaxation run.

EDIFFG	Break condition for a ionic relaxation: If the total energy difference between two ionic steps is smaller than EDIFFG then stop. If EDIFFG is negative then the relaxation will stop if all forces on the ions are smaller than the absolute value of EDIFFG.
NSW	Maximum number of ionic steps. The default value is zero.
POTIM	Sets a scaling constant for a relaxation step. When a coordinate is changed, then the width of the change is proportional to POTIM.
IBRION	This tag sets how the positions of the ions are updated and moved. Several modes '-1, 0, 1, 2, 3, 5, 6, 7, 8, 44' are possible. Within this thesis mode '2' has been used. In this mode a conjugate gradient method is used to obtain the relaxed ion positions.

Tags to store data of the potential.

LVHAR	If this tag is set to .TRUE. then VASP stores the total local potential minus the exchange-correlation-potential to the file LOCPOT.
LVTOT	If this tag is set to .TRUE. then VASP stores the total local potential to the file LOCPOT.

Tags to compute k-paths for bandstructures.

ISTART	Determines whether or not to read the orbital coefficients from the file WAVECAR. ISTART=0 specifies that the coefficients are not read from WAVECAR. ISTART=1 specifies to read the coefficients.
ICHARG	Determines the initial charge density for tag-values from 0 to 4. For tag value 11 the charge density will be read from the file CHGCAR from a previous calulation.

3.2.5 Supercell - How to simulate a surface?

The periodic boundary condition states that a defined crystal cell will be repeated infinitely times in all spatial directions. To simulate a surface of a crystal, one has to construct a so-called supercell [24]. That means that the usual unit cell is enlarged into the normal direction of the surface plane. The enlarged space is kept empty and represents the vacuum - see Fig. 3.4 where the supercell of a (100) slab consisting of 15 layers is visualized. There are three important questions:

1. What (enlarged) thickness is needed for a good representation of the vacuum?
2. How many atom layers are necessary for a good simulation?
3. Does the geometric equilibrium still hold for the 'bulk' positions of the atoms in the presence of a vacuum?

All three questions are taken into account within the simulations in this theses. The first and the second questions offer to perform convergence tests, while the last one can be handled via Eq. 2.18, which has been derived with the help of the Hellmann-Feynman theorem. Such a geometric optimization is already implemented in VASP and is used in the simulations in this thesis. If the surface plane is normal to the z-direction, the z-values of the ionic positions have to be relaxed only. Therefore the VASP-tags for ionic relaxations of Tab. 3.2 has to be specified. Additionally, in the POSCAR file one has to set what coordinates of what ions has to be relaxed. For example, the relaxed POSCAR file of Al(100) is given below.

```
 1  Al(100) surface 05 layer
 2     1.0000000000000000
 3       2.8567113959936519    0.0000000000000000    0.0000000000000000
 4       0.0000000000000000    2.8567113959936519    0.0000000000000000
 5       0.0000000000000000    0.0000000000000000   20.0799999999999983
 6     Al
 7       5
 8  Selective dynamics
 9  Direct
10    0.000000000000000  0.000000000000000  0.795571630928995   F   F   T
11    0.500000000000000  0.500000000000000  0.898145385663847   F   F   T
12    0.000000000000000  0.000000000000000  0.000000000000000   F   F   F
13    0.500000000000000  0.500000000000000  0.101854614336152   F   F   T
14    0.000000000000000  0.000000000000000  0.204428369071004   F   F   T
```

In line 8 the first character 'S' states that there is additional information to the positions of the ions (lines 10–14) that specifies whether a coordinate of a ion can be changed during ionic relaxation or not. This specification is set by the characters 'T' and 'F'. However, at least one coordinate in z-direction should be set to FALSE, otherwise it could be possible that during ionic relaxation the whole slab is moving through the supercell.

3.3 Calculation of photoemission intensity

3.3.1 The one-step model

If a photon of sufficiently large energy $\hbar\omega$ excites an electron of a sample, and no electron-electron collision and no electron-phonon collision takes place, then the electron will be emitted with the energy $\hbar\omega - E_B$ off the solid, where E_B is the binding energy of the initial electron state. The binding energy can be rewritten by $E_B = E_i + \Phi$ where Φ is the work function of the sample and E_i is the energy below the Fermi level of the initial state of the electron before it has been emitted. A schematically picture of this process of ultraviolet angle-resolved photoelectron spectroscopy (ARPES) is illustrated in Fig. 3.5. Within the one-step model of photoemission, the intensity of the emitted electrons is given by the sum over the transition probabilities of all occupied orbitals [25, 26]

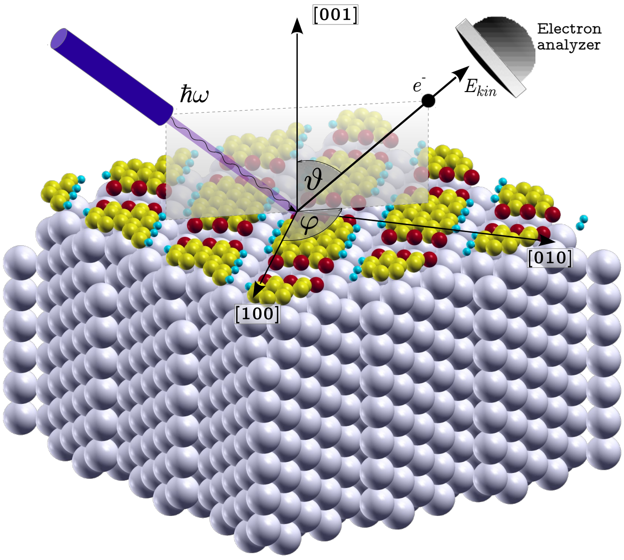

Figure 3.5: The one-step model.

$$I(\vartheta, \varphi; E_{kin}) \propto \sum_i \left| \langle \psi_f^*(\vartheta, \varphi; E_{kin}) | \frac{e}{2mc} (\mathbf{A} \cdot \mathbf{p} + \mathbf{p} \cdot \mathbf{A}) | \psi_i \rangle \right|^2 \times \delta(E_i + \Phi + E_{kin} - \hbar\omega). \tag{3.62}$$

Here, the δ-functional guarantees energy conservation. Additionally, the parallel momentum is conserved. The photon interacts through its vector potential $\mathbf{A}$ and momentum operator $\mathbf{p}$. Moreover, $|\psi_f\rangle$ represents the final state and $|\psi_i\rangle$ represents the initial state, an occupied orbital, of the emitted electron. The polar emission angle ϑ, the azimuthal emission angle φ and the kinetic energy E_{kin} of the emitted electron is just another representation of the wavevector $\mathbf{k}$ of the emitted electron [8]

$$\begin{aligned} k_x &= \sqrt{2m_e E_{kin}/\hbar^2} \sin\vartheta \cos\varphi \\ k_y &= \sqrt{2m_e E_{kin}/\hbar^2} \sin\vartheta \sin\varphi \\ k_z &= \sqrt{2m_e E_{kin}/\hbar^2} \cos\vartheta \end{aligned} \tag{3.63}$$

Within the one-step model higher orders of interaction are neglected, which would describe that an excited electron would fall back to its initial state and emits another photon which excites another electron (and so on).

Further, for ultraviolet (UV) light one can apply the dipole approximation. Since the wavelengths of UV light are much larger than usual lattice constants, one can neglect the the spatial derivation of the photon vector potential. With that the commutator of the momentum operator and the vector potential vanishes

$$[\mathbf{p}, \mathbf{A}] = -i\hbar\nabla \cdot \mathbf{A} \approx 0 \tag{3.64}$$

and hence the dipole approximation simplifies the term

$$\frac{e}{2mc}(\mathbf{A} \cdot \mathbf{p} + \mathbf{p} \cdot \mathbf{A}) \approx \frac{e}{mc}\mathbf{A} \cdot \mathbf{p} \tag{3.65}$$

3.3.2 Final state approach

The most simple approximation, and one which has been shown to produce excellent results for organic molecules/metals [25], is to approximate the final state $|\psi_f\rangle$ in Eq. 3.62 by a plane wave. Here, a plane wave does not include the possibility of an interaction of the electron with the matter. This fact is taken into account by introducing an inelastic mean free path (IMFP) z_0 for the electrons inside the metal. The intensity of excited electrons which do not interact inside the solid decreases exponentially by the IMFP into the solid.

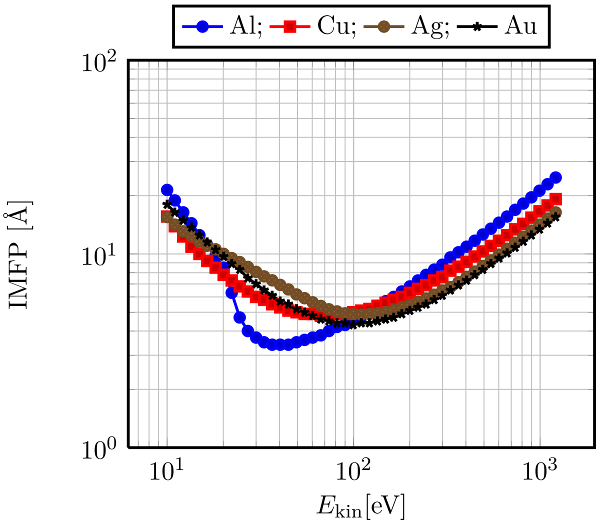

Figure 3.6: Universal curve of the inelastic mean free path (IMFP) for the materials Al, Cu, Ag, Au.

$$I = I_0 e^{-\frac{z}{z_0}} \tag{3.66}$$

The IMFP z_0 can be approximately described by a function of the kinetic energy E_{kin} of the electron, the so-called universal curve. Fig. 3.6 shows the universal curve for the materials aluminium, copper, silver and gold taken from [27].

4 Results

In the first section, the uncovered metal surfaces of aluminium and copper are investigated. A convergence study with respect to the number of atomic metal layers forms the heart of the first section. In order to strengthen the significance of the statements, convergence studies with respect to the k-mesh and with respect to the vacuum thickness are performed. Apart from surface energies and from work functions of the studied facets, surface states are determined and several properties, e.g. the effective electron mass, are calculated. The simulated results are then compared with selected experimental data. Furthermore photoemission intensity maps of Cu(110) are calculated within the one-step model. In the second section, the metallic Ag(110) surface covered by the organic molecule PTCDA (3,4,9,10-perylene-tetracarboxylic-dianhydride) is considered. As in the first part, the number of metal layers are varied and photoemission intensity maps are calculated.

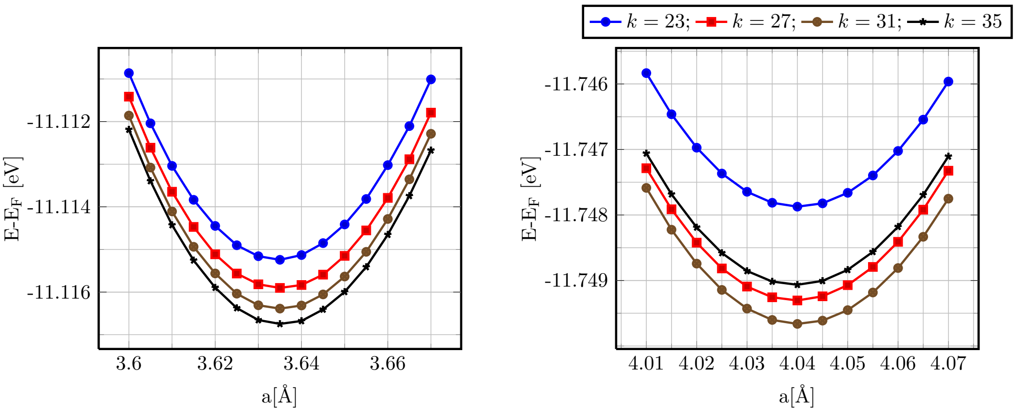

(a) Copper.

(b) Aluminium.

Figure 4.1: Total energy vs. lattice constant of copper and aluminium.

DFT-GGA optimized lattice constant. A simple application of the VASP package is to calculate the DFT-GGA optimized lattice constants of aluminium (Al) and copper (Cu). For this purpose, one varies the size of the lattice constant of the simulated structure, solves for each size the Kohn-Sham equations and plots the lattice constant versus the total energy leading to the equation of state (Energy vs. volume). This is a standard method to find theoretical values of the lattice constant of a compound. Additionally, in Fig. 4.1 the equation of state curves are computed for various k-meshes. For the lattice constant $a_{sim} = 3.635$ Å, the simulated total energy of copper reaches its minimum. The experimental value of copper reads $a_{exp} = 3.61$ Å. For aluminium one has $a_{sim} = 4.04$ Å and $a_{exp} = 4.05$ Å. Note that for all subsequent calculations of this thesis, the DFT-optimized lattice constants a_{sim} are used.

4.1 Uncovered metal surfaces

4.1.1 Vacuum thickness

When constructing a surface within the repeated slab approach, a vacuum layer has to be inserted in order to separate adjacent surfaces in the supercell. In order to determine the appropriate width of this layer, a convergence study is performed. In Fig. 4.2a the surface energy of a 15 layer Al(100) slab and in Fig. 4.2b the work function of a 15 layer Al(100) slab is plotted against the vacuum thickness. Since here the focus is set on the vacuum thickness, the surface energy and the work function are defined later in Subsec. 4.1.5 and Subsec. 4.1.6. For the subsequent studies of clean surfaces a vacuum thickness of 12 Å is taken.

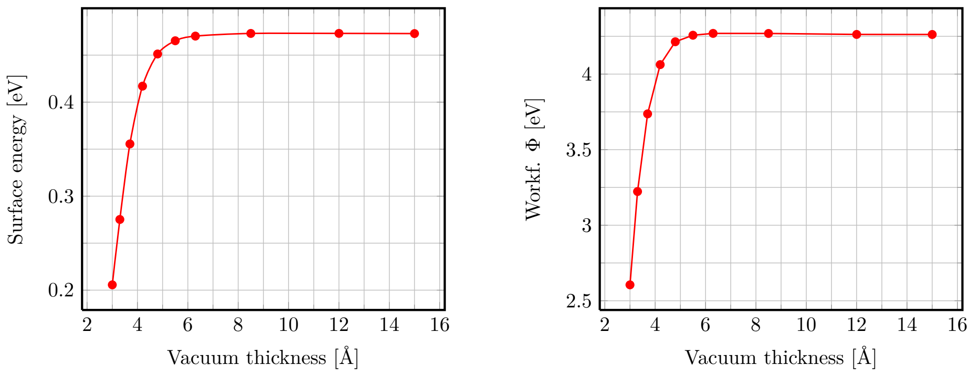

(a) Surface energy of Al(100).

(b) Work function of Al(100)

Figure 4.2: Convergence studies of the vacuum thickness.

4.1.2 Number of k-points

As for the vacuum thickness, a brief study about the convergence with respect to the k-point-sampling is now considered. In Fig. 4.3a and in Fig. 4.3b, the surface energy and the work function of Al(100) is plotted against the number of **k**-points in the first Brillouin zone.

For further studies in this section the used number of **k**-points is 27x27x19 (27x27x1) for (100) and (111) bulk (surface) calculations and 27x19x27 (27x19x1) for (110) bulk (surface) calculations [1].

---

[1] For a (110) facet the ratio $|\mathbf{b}_1|/|\mathbf{b}_2| = \sqrt{2}$. In order to obtain an almost square k-mesh, the number of **k**-points along $\mathbf{b}_2$ is choosen to $19 \approx 27 \cdot \frac{1}{\sqrt{2}}$.

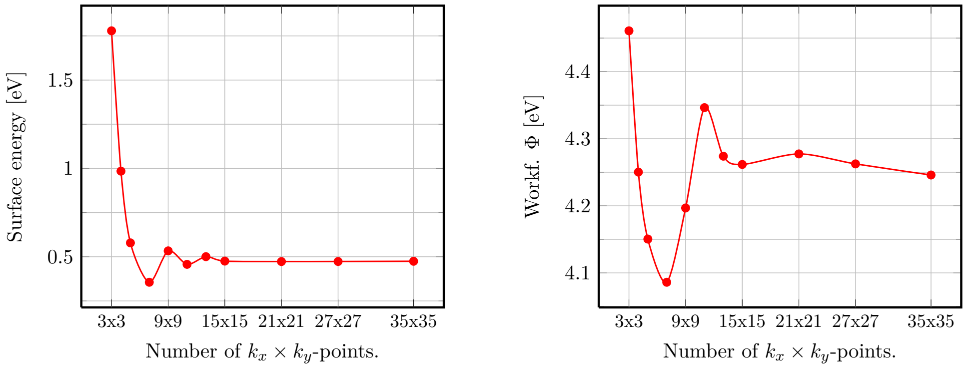

(a) Surface energy of Al(100).

(b) Work function of Al(100).

Figure 4.3: Convergence studies of number of **k**-points.

4.1.3 Ionic relaxation

The distances between the ions in a slab such as in Fig. 3.4 need to be modified because due to the surface the crystal translational symmetry is broken. Particularly for ions near to the surface, interlayer spacings are expected to relax where typical changes are in the order of 5% with respect to bulk interlayer distances. The INCAR file of the ionic relaxation reads

```
SYSTEM = ionic relaxation

PREC   = Accurate
ENCUT  = 400        # plane wave cut−off in eV
EDIFF  = 1E−8       # total energy scf−criterion

EDIFFG = −1E−2      # break condition for ionic relaxation
IBRION = 2          # take conjugate gradient method
NSW    = 50         # Maximum number of ionic steps
POTIM  = 0.1        # scaling constant for a relaxation step
SMASS  = −3
```

The tag EDIFFG=-E-2 guarantees that after the ionic relaxation all forces acting on the ions have dropped below 0.01 eV / Å. A conjugate gradient method is used by setting IBRION=2. The corresponding POSCAR file is similar to the one in Subsec. 3.2.5. The unrelaxed POSCAR file can be constructed via Eqs. 2.24 and 2.25.

Such relaxation calculations are rather time consuming. One has to perform a self-consistent calculation for every geometric step.

Since the distance between adjacent layers d_{ij} converges to material dependent numbers, one can save much computational time when using the relaxed data from previous calculations. For example when calculating the ionic relaxed positions for a N-layer slab and the $N-1$ slab has already been relaxed, then one can use the results of d_{ij} of the $N-1$-layer slab to construct a pre-relaxed N-layer slab. For this pre-relaxed slab less geometric steps are needed to reach the desired accuracy specified by the tag EDIFFG. Such a construction scheme has been used within this thesis.

After the ionic relaxation has been completed, one can calculate the difference of the relaxed and the bulk distances d_{ij}, where i and j denote the layer number counted from the top to bottom, respectively.

$$\Delta d_{ij} \equiv d_{ij}^{relaxed} - d_{ij}^{bulk} \tag{4.1}$$

A list of Δd_{12} for aluminium and copper facets is given in Tab. 4.1.

Table 4.1: Relative changes in interlayer distances Δd_{12} of aluminium and copper. The absolute values of the Hellmann-Feynman forces on the ions have dropped below 0.01 eV Å^{-1}.

	Δd_{12} [%]					
Number of layers	Al(100)	Al(110)	Al(111)	Cu(100)	Cu(110)	Cu(111)
5	1.96	-6.86	1.61	-3.15	-9.46	-1.01
6	0.90	-9.83	0.64	-3.11	-10.22	-0.81
7	1.62	-8.46	0.68	-3.00	-9.88	-0.80
8	1.02	-7.19	1.40	-2.94	-10.13	-0.96
9	1.58	-5.91	0.95	-2.86	-9.90	-0.86
10	1.50	-7.07	0.65	-2.99	-10.08	-0.90
11	1.82	-8.88	1.14	-2.98	-9.95	-0.86
12	1.75	-8.04	0.94	-3.00	-10.07	-0.90
13	1.78	-6.73	0.81	-3.01	-10.06	-0.86
14	1.54	-7.21	0.87	-2.94	-9.98	-0.90
15	1.46	-7.34	0.93	-3.00	-9.97	-0.89
16	1.51	-8.10	0.79	-3.00	-10.05	-0.88
17	1.33	-7.94	0.88	-3.03	-10.05	-0.88
18	1.42	-7.43	0.94	-3.00	-9.93	-0.86
19	1.37	-7.30	0.81	-3.03	-10.05	-0.87
20	1.43	-7.71	0.86	-3.01	-10.05	-0.88
21	1.44	-7.88	0.94	-3.02	-10.05	-0.86
22	1.46	-7.66	0.85	-3.01	-10.00	-0.86
23	1.44	-7.49	0.86	-3.02	-10.05	-0.88
24	1.41	-7.48	0.94	-3.01	-9.99	-0.85
25	1.42	-7.65	0.81	-3.02	-10.05	-0.87

In Fig. 4.4, the relaxation distances Δd_{ij} in percent between adjacent layers i and j of the three investigated aluminium facets are plotted. As expected Δd_{ij} tends to zero for increasing indices i and j. One interesting feature is the sign of Δd_{ij}. For example the sign of Δd_{ij} of Al(110) alternates with increasing indices. In Fig. 4.5

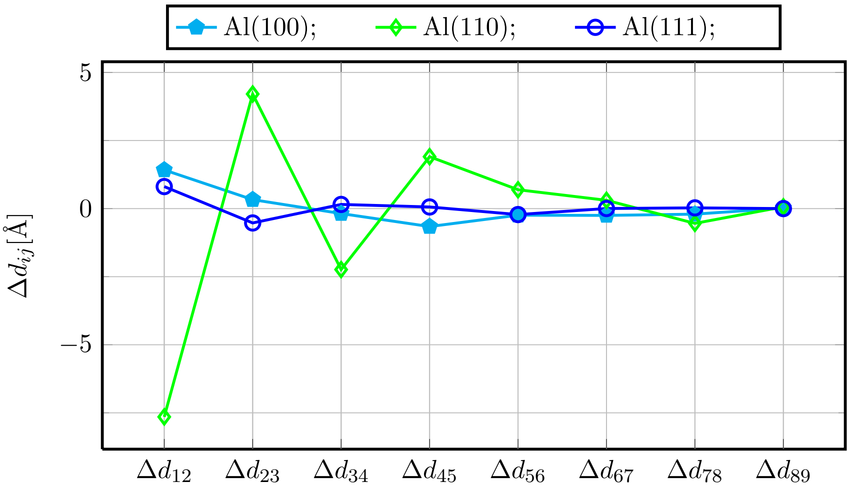

Figure 4.4: Relative changes in interlayer distances Δd_{ij} of 25-layer Al(100), Al(110), and Al(111) slabs.

the relative relaxation distances Δd_{ij} between adjacent layers i and j of the three investigated copper facets are plotted. One also notes that relaxations are largest for the (110) facet which contains the least-coordinated atoms on the surface, the (111) facet shows the smallest geometrical changes due to the high coordination number of surface atoms.

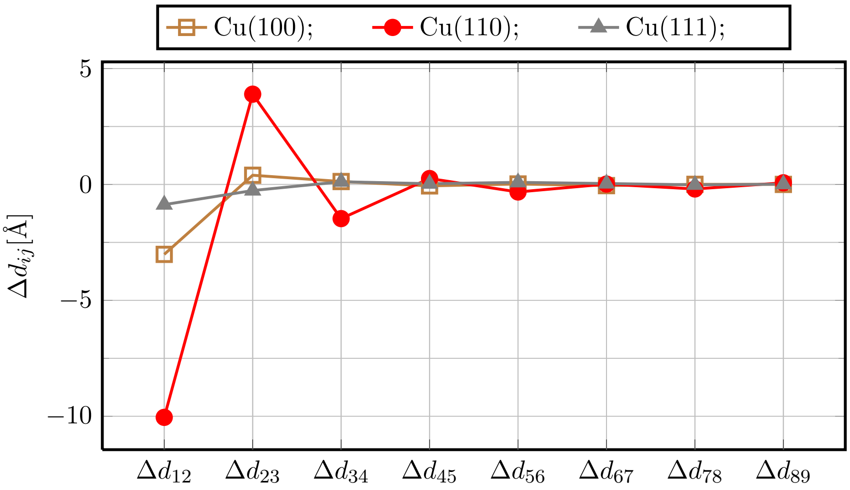

Figure 4.5: Relative changes in interlayer distances Δd_{ij} of 25-layer Cu(100), Cu(110), and Cu(111) slabs.

4.1.4 Band structure

Consider a unit cell of a bulk system which is constructed by N layers perpendicular to the z-direction of the unit cell. Within VASP two steps of calculation are needed to obtain the energy and **k**-point data for band structures. In the first step, one has to solve self-consistently the Kohn-Sham equations of the system. In the second step, one performs a non-self-consistent calculation using the Kohn-Sham potential and the electron density of the first step. This can be achieved via the VASP-tags ISTART=1 and ICHARG=11. In the second step, the line mode has to be used to define the choosen **k**-path in the file KPOINTS (see Subsec. 3.2.4). Afterwards, the **k**-points of the path and the corresponding energy values of the bands are stored into the file EIGENVAL. In order to get scalar k values for plotting the band structure one has to use the following algorithm.

Computing a scalar k-path from the file EIGENVAL

Each band (denoted as n) of the band structure stored in the file EIGENVAL can be considered as a set

$$\Big\{ \left(\mathbf{k}_1, E^n_{\mathbf{k}_1}\right), \left(\mathbf{k}_2, E^n_{\mathbf{k}_2}\right), ..., \left(\mathbf{k}_m, E^n_{\mathbf{k}_m}\right) \Big\} \tag{4.2}$$

where m is the number of **k**-points in the **k**-path.

1. Step Set the first **k**-point of the path to zero (or any other constant).

$$k_1 \equiv 0 \tag{4.3}$$

2. Step Compute the difference vector $\Delta\mathbf{k}_j$.

$$\forall j \in \{2, 3, ..., m\} : \qquad \Delta\mathbf{k}_j \equiv \mathbf{k}_j - \mathbf{k}_{j-1} \tag{4.4}$$

3. Step Transform the difference vector from the reciprocal basis into the Cartesian basis.

$$\forall j \in \{2, 3, ..., m\} : \qquad \Delta\mathbf{k}'_j \equiv B^T\mathbf{k}_j \tag{4.5}$$

where $B = \begin{pmatrix} b_{11} & b_{12} & b_{13} \\ b_{21} & b_{22} & b_{23} \\ b_{31} & b_{32} & b_{33} \end{pmatrix}$ with the reciprocal lattice vectors $\mathbf{b}_i = \begin{pmatrix} b_{i1} \\ b_{i2} \\ b_{i3} \end{pmatrix}$.

4. Step Compute the scalar k-value.

$$\forall j \in \{2, 3, ..., m\} : \qquad k_j \equiv k_{j-1} + |\Delta\mathbf{k}'_j| \tag{4.6}$$

Finally, after applying this algorithm for all bands stored in EIGENVAL, one has obtained a bandstructure which can be plotted using two dimensions only.

$$\Big\{ \left(k_1, E^n_{\mathbf{k}_1}\right), \left(k_2, E^n_{\mathbf{k}_2}\right), ..., \left(k_m, E^n_{\mathbf{k}_m}\right) \Big\} \tag{4.7}$$

Bulk projected bandstructures

When comparing the band structure of a slab calculation with that of the bulk crystal, one represents the bulk band structure as so-called bulk projected band structure. Since the k_z value is not a good quantum number for the surface due to the broken translational symmetry at the surface, one plots band structures for a series of k_z values. In practice one has to increase the z-value by sufficiently small steps from $k_z = 0$ to $k_z = k_{z,max} \equiv b_{33}/2$ and calculate for each k_z the band structure, where b_{33} is the z-coordinate of the reciprocal lattice vector $\mathbf{b}_3$ (see Eqs. 2.34, 2.36, and 2.38). A $\mathbf{k}$-point with z-component $k_z = k_{z,max}$ is located at the edge of the Brillouin zone. Finally, one can plot all these computed bands together and one has a bandstructure with 'filled' bands. Within this method band gaps are easily visible. For the calculation of the energy bands of the slab calculation (the bands which are

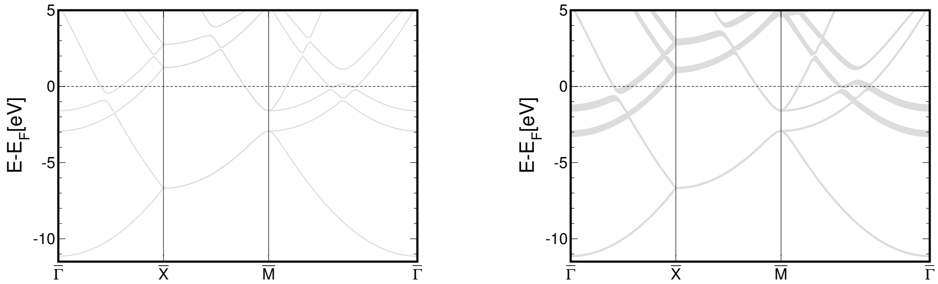

(a) Bulk projected band structure for $k_z = 0$.

(b) Bulk projected band structure for $k_z \in \{0, 1/10 k_{z,max}\}$.

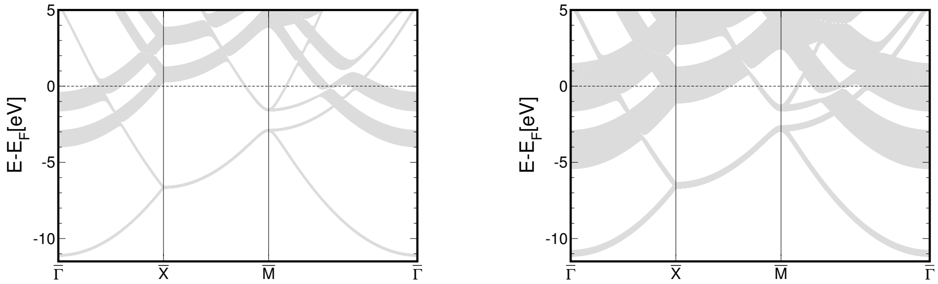

(c) Bulk projected band structure for $k_z \in \{0, 2/10 k_{z,max}\}$.

(d) Bulk projected band structure for $k_z \in \{0, 4/10 k_{z,max}\}$.

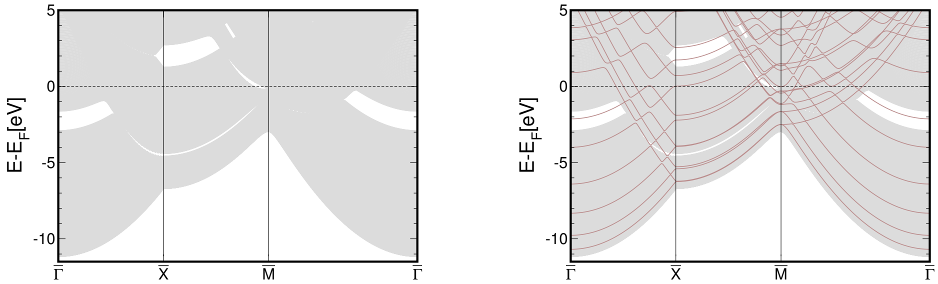

(e) Whole bulk projected band structure for $k_z \in \{0, k_{z,max}\}$.

(f) Surface band structure of 5 layer slab compared with the bulk projected band structure.

Figure 4.6: Band structure generation of Al(100).

plotted overlayed on top of the bulk bands in Fig. 4.6f), one computes the **k**-path with $k_z = 0$ only. Afterall, one can plot the bands of the supercell onto the bulk bands. This is a method to find surface states via bandstructures. A surface state corresponds to an energy band which is located in a band gap of the bulk projected bands.

The choosen **k**-path for the (100) facet is

$$\overline{\Gamma} - \overline{X} - \overline{M} - \overline{\Gamma} \tag{4.8}$$

for the (110) facet

$$\overline{S} - \overline{Y} - \overline{\Gamma} - \overline{S} - \overline{X} - \overline{\Gamma} \tag{4.9}$$

and for the (111) facet

$$\overline{\Gamma} - \overline{M} - \overline{K} - \overline{\Gamma} \tag{4.10}$$

These special **k**-points of the first Brillouin zone have been defined in Subsec. 2.2.4 The three **k**-paths above are visualized in Figs. 2.4–2.6 by the red lines.

The KPOINTS file for the **k**-path of a (100) facet, which has been used for Fig. 4.6f, reads

```
kpoints for bandstructure G-X-M-G
81                               # number of k-points of one line
line                             # switch to line mode
reciprocal                       # reciprocal coordinate mode

 0.00000  0.00000  0.000  1    # Gamma
 0.50000  0.00000  0.000  1    # X

 0.50000  0.00000  0.000  1    # X
 0.50000  0.50000  0.000  1    # M

 0.50000  0.50000  0.000  1    # M
 0.00000  0.00000  0.000  1    # Gamma
```

The second line states that 81 **k**-points are computed between two specified points. That's in total 243 points for each energy band of the (100) facet.

In Figs. 4.7–4.12 the band structures of the three investigated surfaces of aluminium and copper are plotted. The bulk energy bands are visualized by the gray areas. The energy bands of the slab calculation are shown as lines. A brown color is used for bulk-like bands, that are those which lie on top of areas filled by the bulk projected bands. Bands which exhibit a pronounced surface state character, i.e., which are located in the gaps of the bulk projected bands, are highlighted by the red lines.

In all bandstructure plots the Fermi energy is set to zero. The Fermi level is figured by a dashed line.

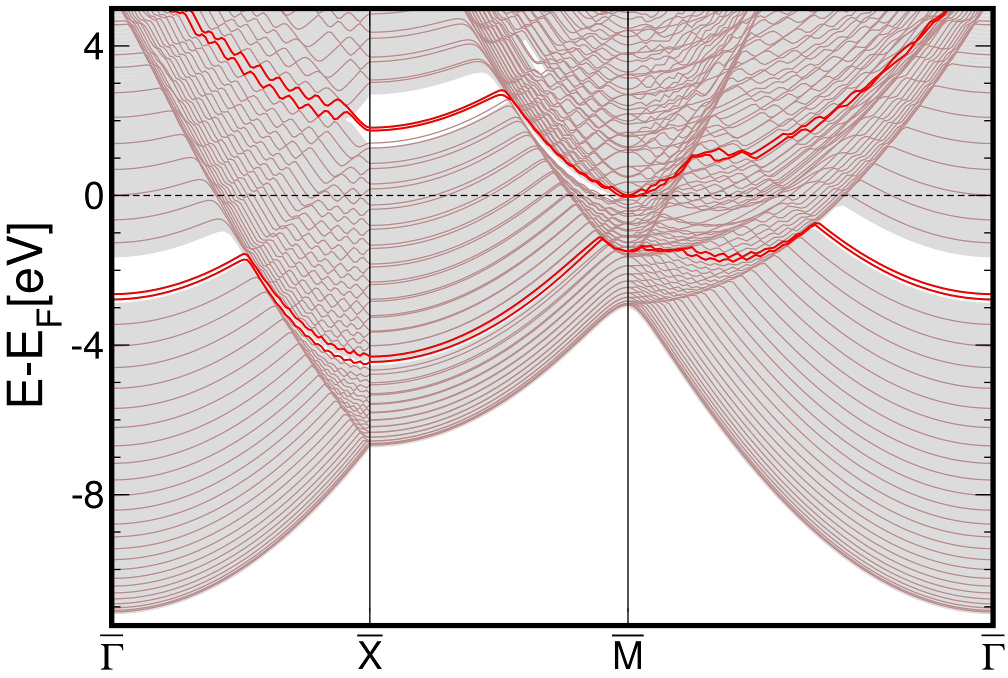

Figure 4.7: Band structure of a 25-layer Al(100) slab plotted on top of the bulk projected band structure.

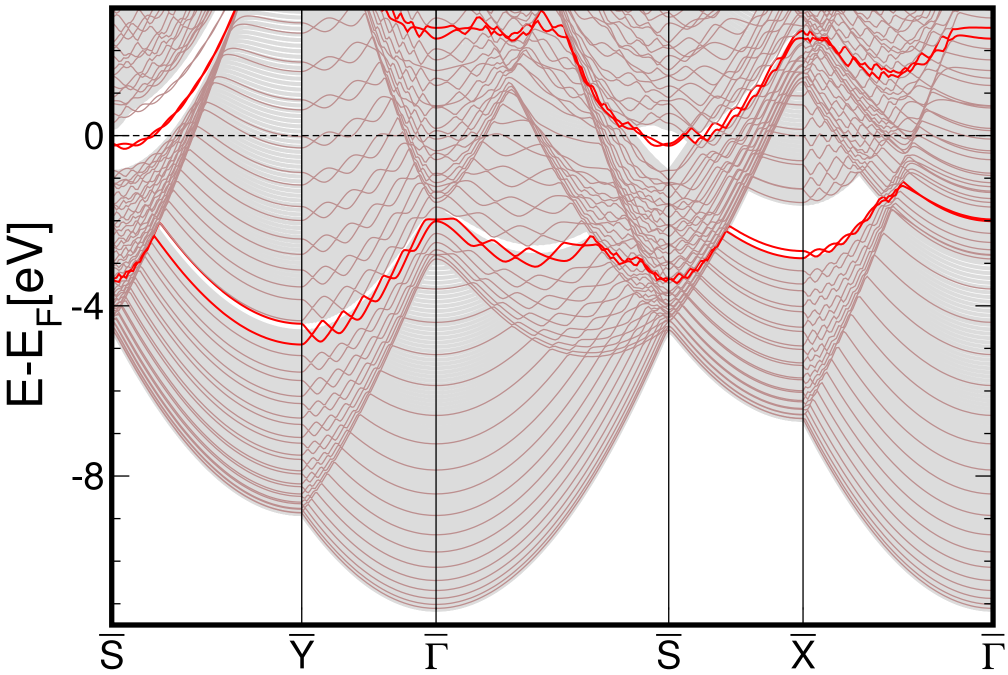

Figure 4.8: Band structure of a 25-layer Al(110) slab plotted on top of the bulk projected band structure.

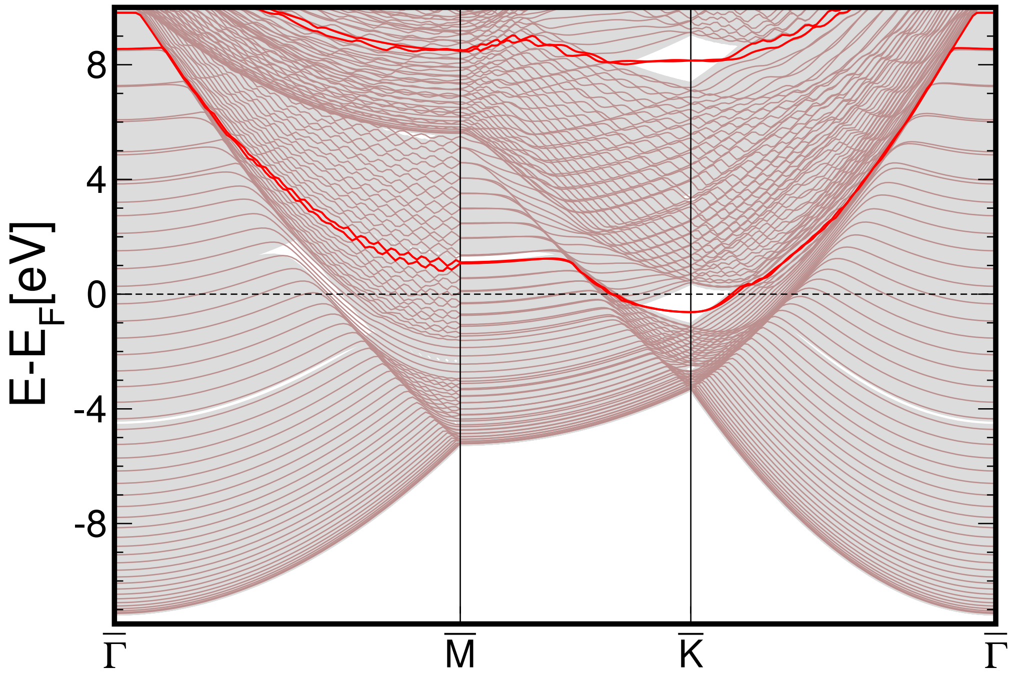

Figure 4.9: Band structure of a 25-layer Al(111) slab plotted on top of the bulk projected band structure.

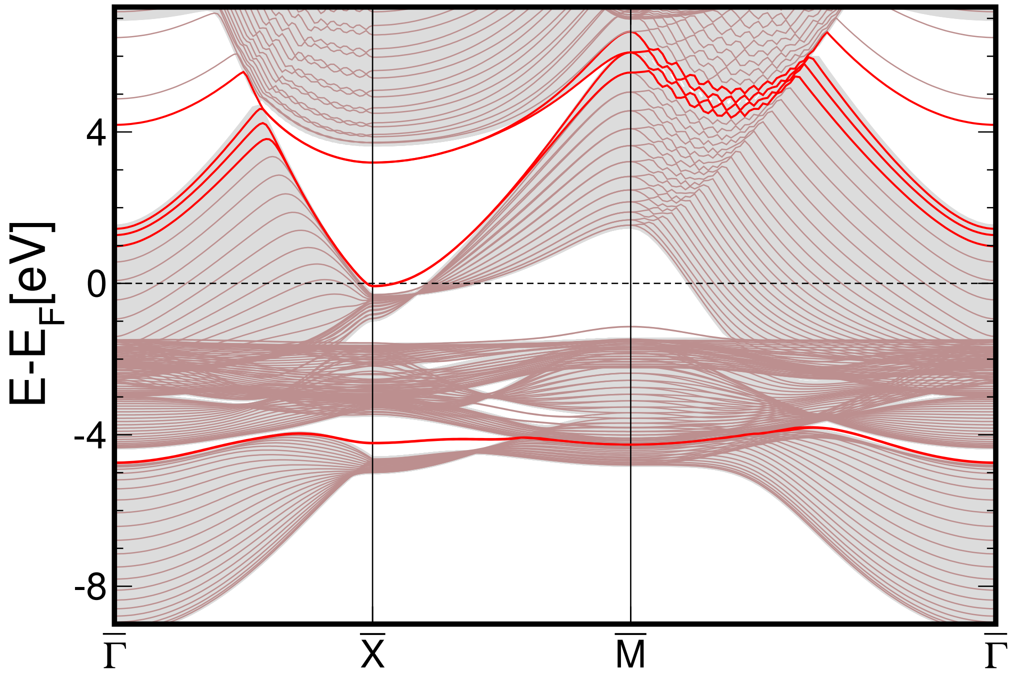

Figure 4.10: Band structure of a 25-layer Cu(100) slab plotted on top of the bulk projected band structure.

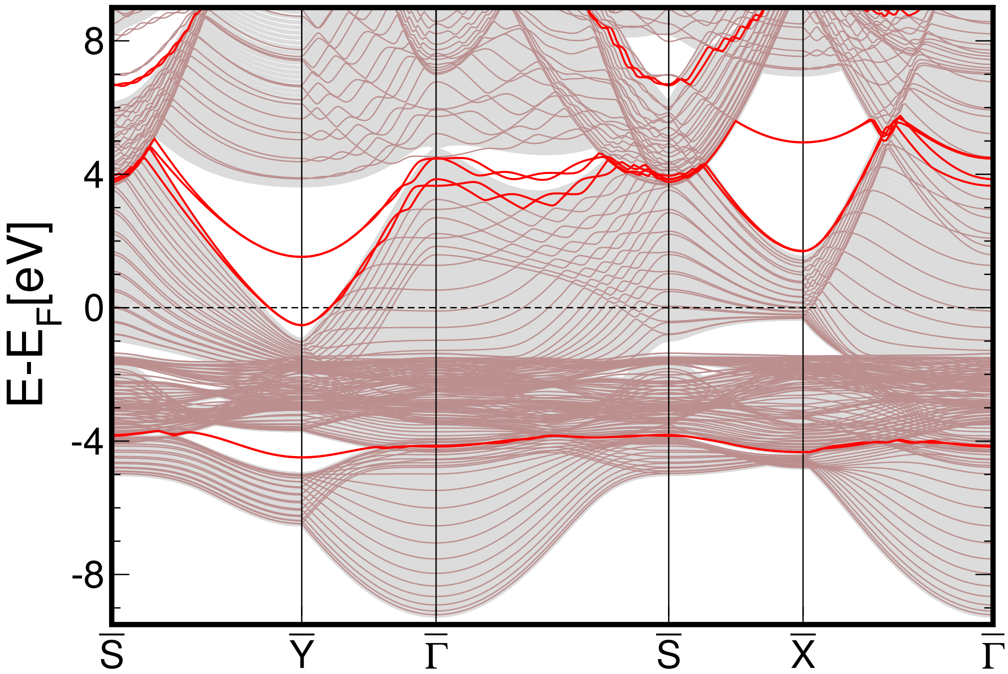

Figure 4.11: Band structure of a 25-layer Cu(110) slab plotted on top of the bulk projected band structure.

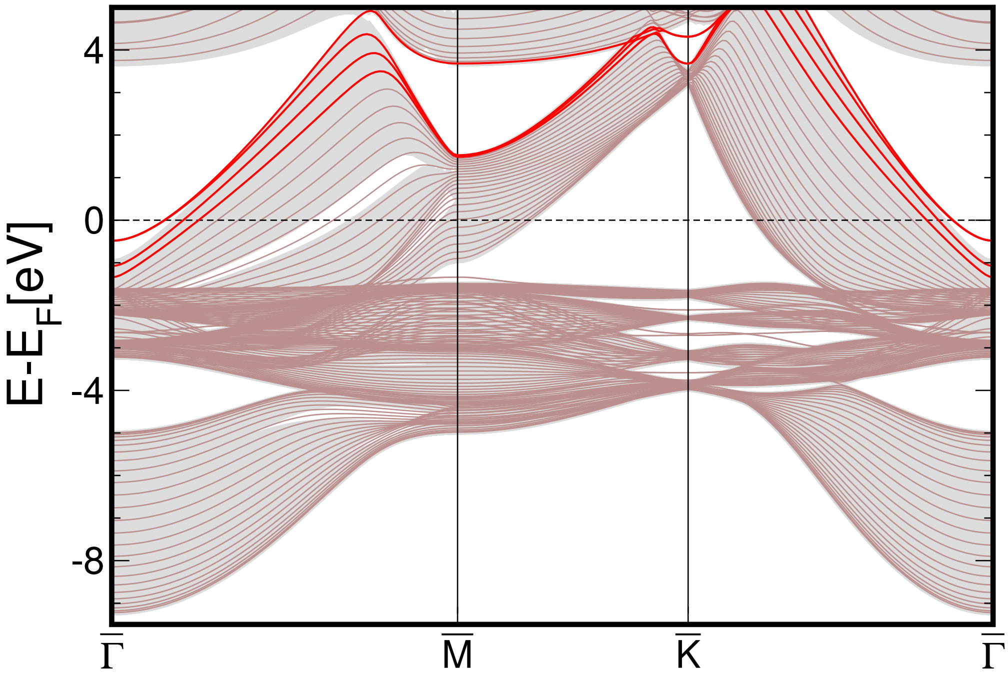

Figure 4.12: Band structure of a 25-layer Cu(111) slab plotted on top of the bulk projected band structure.

4.1.5 Surface energy

The total energy per molecule/atom of a crystal with a surface differs from the total energy per molecule/atom of its corresponding infinite crystal (bulk). One can define the so-called surface energy as this difference. The crystal defined via Fig. 3.4 has two surfaces per unit cell. Taking this into account the surface energy reads

$$E_{surf} = \frac{1}{2}\left(E_{slab} - N \cdot E_{bulk}\right) \tag{4.11}$$

where E_{slab} is the total energy of the system with the surface, E_{bulk} is the total energy per molecule/atom of the bulk system, and N is the number of layers in the slab. In Fig. 4.13 the surface energies of the investigated surfaces are plotted vs. the number of layers.

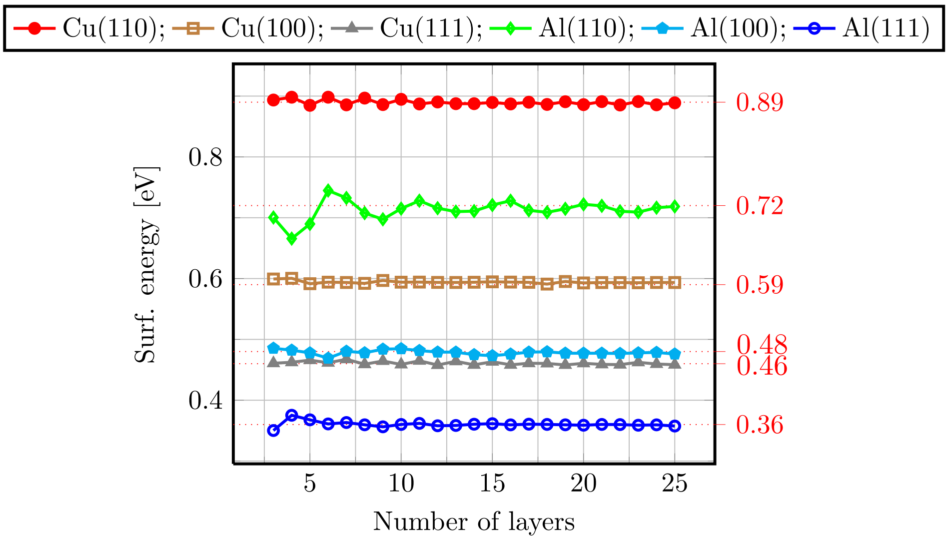

Figure 4.13: Surface energies of copper and aluminium surfaces.

4.1.6 Work function

The main quantity when considering binding energies of valence electrons in a solid is the work function which is the minimum energy which is needed to remove an electron from the crystal surface to the vacuum. For metals the Fermi energy E_F equals the energy of the highest occupied state. The work function is defined through

$$\Phi = E_{vac} - E_F \tag{4.12}$$

Fig. 4.14 shows the plane-averaged [2] electro-static potential for a Al(100) slab consisting of 10 atomic layers. For comparison, also the plane-averaged total potential, i.e., electro-static potential plus exchange-correlation potential is shown [28]. The

---

[2] 'Plane-averaged' means that for each point z the energy potential is arithmetically averaged over the x, y-plane inside the supercell.

exchange-correlation energy does not contribute to the vacuum energy potential. In Fig. 4.15 the work functions of the investigated surfaces are plotted vs. the number of layers.

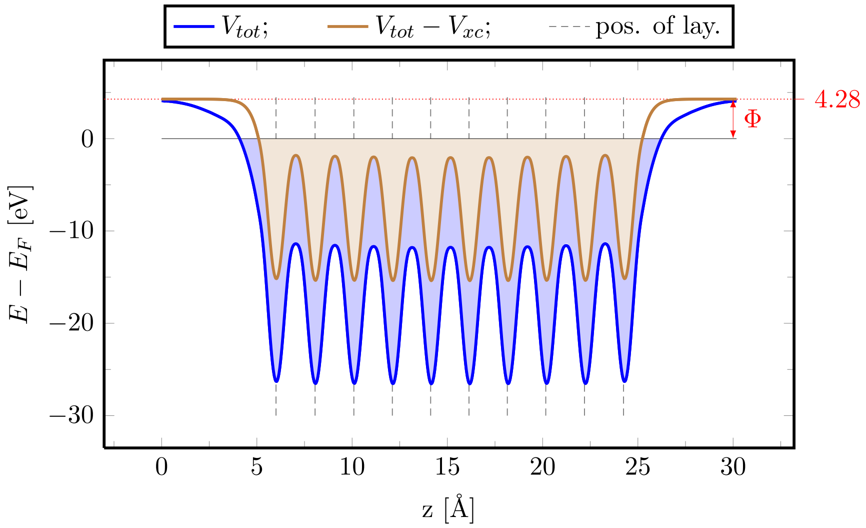

Figure 4.14: Comparison of the total potential with and without the exchange-correlation potential of a 10 layer Al(100) slab.

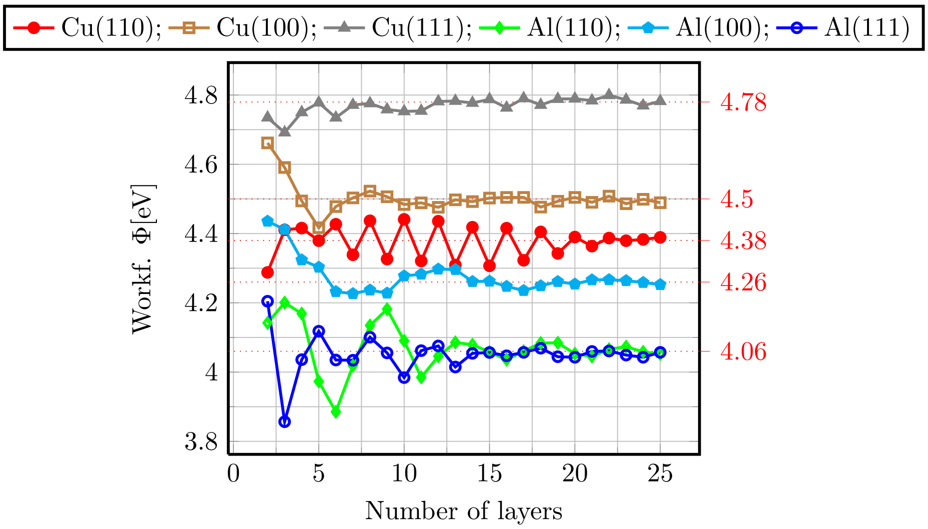

Figure 4.15: Work functions of copper and aluminium surfaces.

4.1.7 Electron density

In VASP the electron (charge) density is stored into the file CHGCAR. Consider for example a CHGCAR file computed for a 5-layer Al(100) slab.

```
1  Al100 surface
2     1.0000000000000000
3       2.856711     0.000000     0.000000
4       0.000000     2.856711     0.000000
5       0.000000     0.000000    20.080000
6     Al
7       5
8  Direct
9    0.000000   0.000000   0.795572
10   0.500000   0.500000   0.898145
11   0.000000   0.000000   0.000000
12   0.500000   0.500000   0.101855
13   0.000000   0.000000   0.204428
14
15    40    40   280
16  -.15139436439E+01  -.99353103102E+00 0.54057079040E+00 ..
17   ..
```

In lines 2–5, a scaling factor and the lattice vectors are stored. In lines 9–13 the positions of the ions are stored. In line 15 the numbers n_1, n_2, and n_3 are stored which define the three-dimensional grid on which the density is calculated. At n_1 equidistant points along the first lattice vector, at n_2 equidistant points along the second lattice vector, and at n_3 equidistant points along the third lattice vector the charge density has been calculated. Then starting from line 16, the $n_1 \cdot n_2 \cdot n_3$ electron density values are stored. The fastest index is that along the first lattice vector, the slowest index is that along the third lattice vector. One can read the values for example with a 'C++' program using the following code.

```cpp
..

char filename[]="CHGCAR";

// read from file CHGCAR
ifstream myfile ( filename );
if (myfile.is_open())
{

// read first line
getline (myfile,line);

// read scale factor
myfile >> scale;

// read lattice vectors
myfile >> a11;
myfile >> a12;
myfile >> a13;
myfile >> a21;
myfile >> a22;
myfile >> a23;
myfile >> a31;
```

```
myfile >> a32;
myfile >> a33;

// compute length of vectors
a1=sqrt( a11*a11 + a12*a12 + a13*a13 );
a2=sqrt( a21*a21 + a22*a22 + a23*a23 );
a3=sqrt( a31*a31 + a32*a32 + a33*a33 );

// volume of cell (a1 x a2)' . a3
vol=( a12 * a23 - a13 * a22 ) * a31 + ( a13 * a21 - a11 * a23 ) * a32 + ( a11 * a22 - a12 * a21 ) * a33;

// area |a1 x a2|
xyarea=sqrt( ( a12 * a23 - a13 * a22 ) * ( a12 * a23 - a13 * a22 ) + ( a13 * a21 - a11 * a23 ) * ( a13 * a21 - a11 * a23 ) + ( a11 * a22 - a12 * a21 ) * ( a11 * a22 - a12 * a21 ) );

// read further lines, depends on number of layers
getline (myfile,line);

..

// read number of points stored along the lattice vectors
myfile >> n1;
myfile >> n2;
myfile >> n3;

// read electron density
for( int k=0; k<n3; k++){
  for( int j=0; j<n2; j++){
    for( int i=0; i<n1; i++){
      // read value
      myfile >> density[i][j][k];
    }
  }
}

// close file
}
myfile.close();

..
```

Now one can compute the average electron density which is equal to the number of valence electrons in the unit cell divided by the cell volume.

$$N_{valence}/V \equiv \overline{n} = \frac{1}{V}\int_{\mathcal{V}} n(x,y,z)dxdydz \tag{4.13}$$

where V is the unit cell volume. One can further calculate the average electron density as a function of z.

$$\overline{n}(z) = \frac{1}{A}\int_{\mathcal{A}} n(x,y,z)dxdy \tag{4.14}$$

where $A = |\mathbf{a}_1 \times \mathbf{a}_2|$ is the area spanned by the first and second lattice vectors. In numerical implementations one has to replace the integral by a sum over all points with the same z. In this case the average electron density reads

$$\overline{n}(z) = \frac{1}{A} \sum_{x,y} n(x,y,z) \Delta x \Delta y \tag{4.15}$$

with $\Delta x = \frac{|\mathbf{a}_1|}{n_x}$ and $\Delta y = \frac{|\mathbf{a2}|}{n_y}$, where n_x and n_y are the number of points along the first and second lattice vectors.

In Fig. 4.16 the average electron densities $\overline{n}(z)$ of Al(110), Al(100), and Al(111) slabs, each consisting of 25 layers, are plotted. The gray area pictures the average positive ionic background charge (jellium model). In order to have a reference position, for all densities in this plot, the unrelaxed z-position of the surface layer is set to zero. One can notice that the ordering of the densities reaching into the vacuum is from Al(111), Al(100) to Al(110). In fact, this is exactly the reverse ordering of the xy-area per ion sizes

$$\mathcal{A}^{xy}_{110} = \frac{1}{\sqrt{2}} a^2 > \mathcal{A}^{xy}_{100} = \frac{1}{2} a^2 > \mathcal{A}^{xy}_{111} = \frac{\sqrt{3}}{4} a^2 \tag{4.16}$$

The area per ion $\mathcal{A}^{xy}$ is a measure how close the ions are packed within the corresponding layer.

Analogously, in Fig. 4.17 the average electron densities $\overline{n}(z)$ for 25 layer slabs of Cu(110), Cu(100), and Cu(111) are plotted. As for aluminium, the ordering of the densities reaching into the vacuum is from Cu(111), Cu(100) to Cu(110).

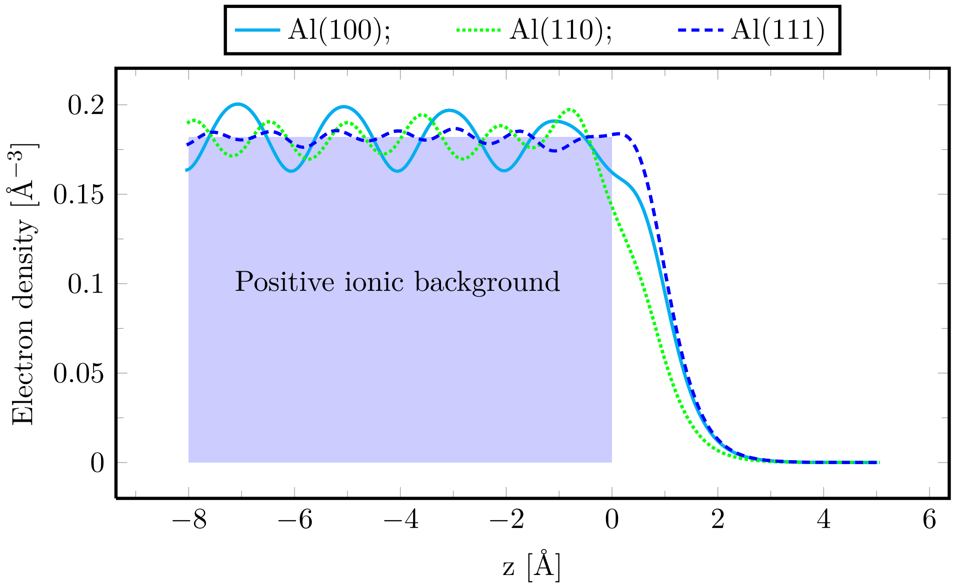

Figure 4.16: Comparison of the electron charge densities of Al(100), Al(110), and Al(111) slabs consisting of 25 layers.

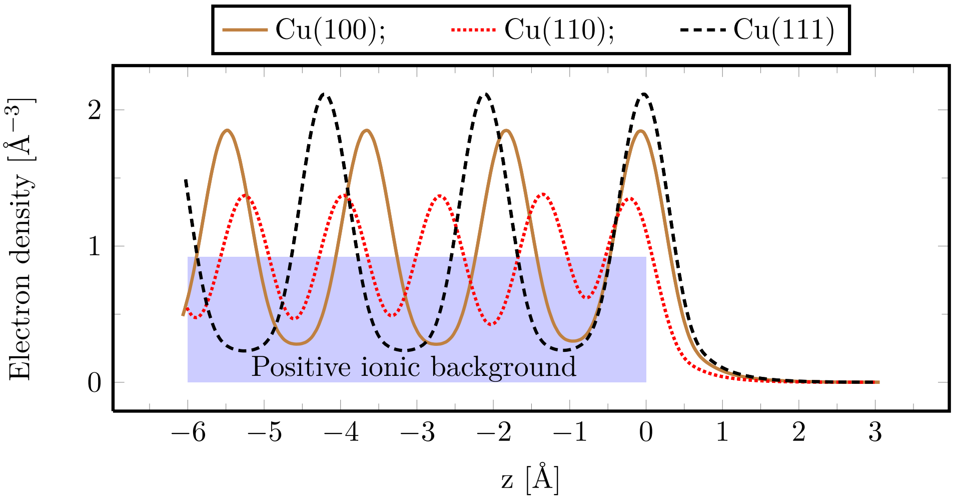

Figure 4.17: Comparison of the electron charge densities of Cu(100), Cu(110), and Cu(111) slabs consisting of 25 layers.

4.1.8 Surface states

The surface states have been identified by plotting the calculated energy bands of a N-layer slab on top of the bulk projected bandstructure. In Tabs. 4.2 and 4.3, a list of surface states has been determined via using the bandstructures of Figs. 4.7–4.12. In order to confirm that a state is indeed a surface state, we visualize the wavefunction or the density contribution of the state. As defined in Sec. 2.3, the amplitude of the wavefunction (and of the electron density) of the surface state has to decrease into the metal, otherwise it is not a surface state, but a bulk or a resonance state. In Fig. 4.18 the electron density of the surface state at the $\overline{S}$ point of Al(110) is plotted. One can see the exponential decay from the surface into the metal. All other surface states listed in Tabs. 4.2 and 4.3 have a similar behaviour. Some of them, for example $\overline{X}_2$ and $\overline{M}$ of Cu(100), are so strongly confined to the topmost layer that only one peak is visible.

Table 4.2: Energy and **k**-point positions of surface states of aluminium. There are labels defined for some surface states.

Al(100)		Al(110)		Al(111)	
at **k**-point	$E-E_F$[eV]	at **k**-point	$E-E_F$[eV]	at **k**-point (label)	$E-E_F$[eV]
$\overline{\Gamma}$	-2.72	$\overline{S}$	-0.22	$\overline{K}$ ($\overline{K}_1$)	-0.63
$\overline{X}$	1.78	$\overline{X}$	-2.79	$\overline{K}$ ($\overline{K}_2$)	8.14

Table 4.3: Energy and **k**-point positions of surface states of copper. There are labels defined for some surface states.

Cu(100)		Cu(110)		Cu(111)	
at **k**-point (label)	$E - E_F$[eV]	at **k**-point (label)	$E - E_F$[eV]	at **k**-point (label)	$E - E_F$[eV]
$\overline{\Gamma}$	-4.73	$\overline{S}$	6.70	$\overline{\Gamma}$	-0.48
$\overline{M}$	-1.14	$\overline{X}$ ($\overline{X}_1$)	1.69	$\overline{K}$ ($\overline{K}_1$)	-3.76
$\overline{X}$ ($\overline{X}_1$)	-4.21	$\overline{X}$ ($\overline{X}_2$)	4.95	$\overline{K}$ ($\overline{K}_2$)	-3.58
$\overline{X}$ ($\overline{X}_2$)	-0.06	$\overline{Y}$ ($\overline{Y}_1$)	-4.49	$\overline{K}$ ($\overline{K}_3$)	-3.07
$\overline{X}$ ($\overline{X}_3$)	3.19	$\overline{Y}$ ($\overline{Y}_2$)	-0.53	$\overline{K}$ ($\overline{K}_4$)	-2.70
		$\overline{Y}$ ($\overline{Y}_3$)	1.52	$\overline{K}$ ($\overline{K}_5$)	-2.67
				$\overline{K}$ ($\overline{K}_6$)	-2.11
				$\overline{K}$ ($\overline{K}_7$)	3.67
				$\overline{K}$ ($\overline{K}_8$)	4.30

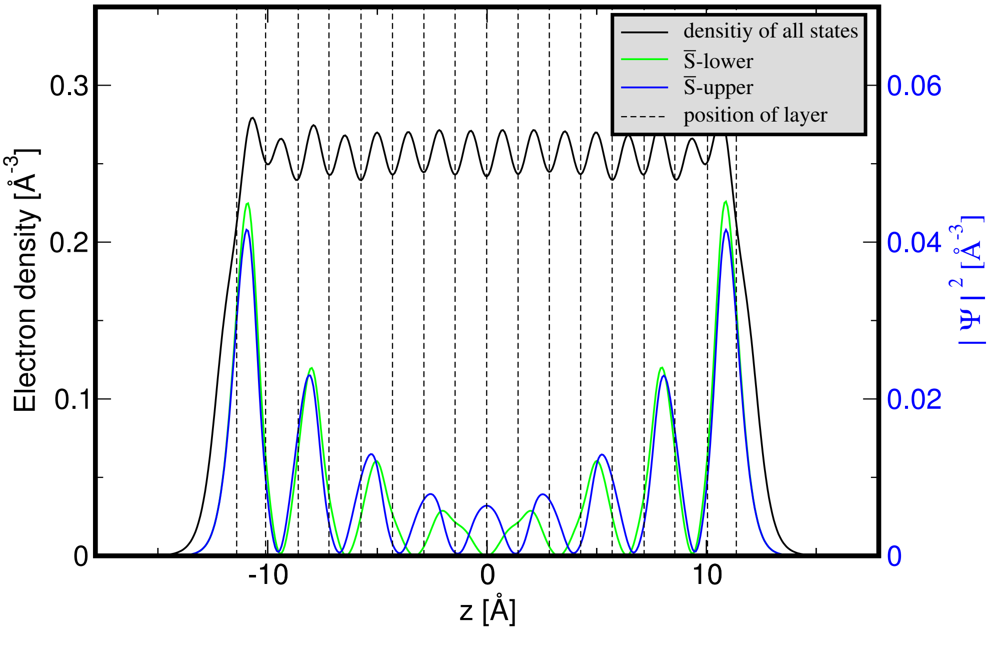

Figure 4.18: Electron density per cell volume of the surface state at the $\overline{S}$ point of Al(110). The vertical dotted lines depict the z-positions of the layers. Additionally, the total electron density is plotted. The right ordinate labels the density for the surface state and the left ordinate labels the total density.

4.1.9 Splitting energy

In Fig. 4.19 a surface state of the surface Al(110) at the $\overline{S}$-point is plotted. Here, the energy band of the surface state is shown for several numbers of layers. One can notice that there are in fact two surface state bands, one one arising from the top, the other from the bottom surface of the slab. As long as the slab thickness is smaller than the vertical decay rate of the surface state, these two states will interact with each other and their energies will split forming a bonding and an anti-bonding combination, respectively. The vertical distance between the energy values of both surface bands at the $\overline{S}$ point decreases exponentially for a linear increase of the numbers of layers. This vertical distance is the so-called splitting energy of the two energy bands. The exponential decay gives another characteristic of the speed of convergence.

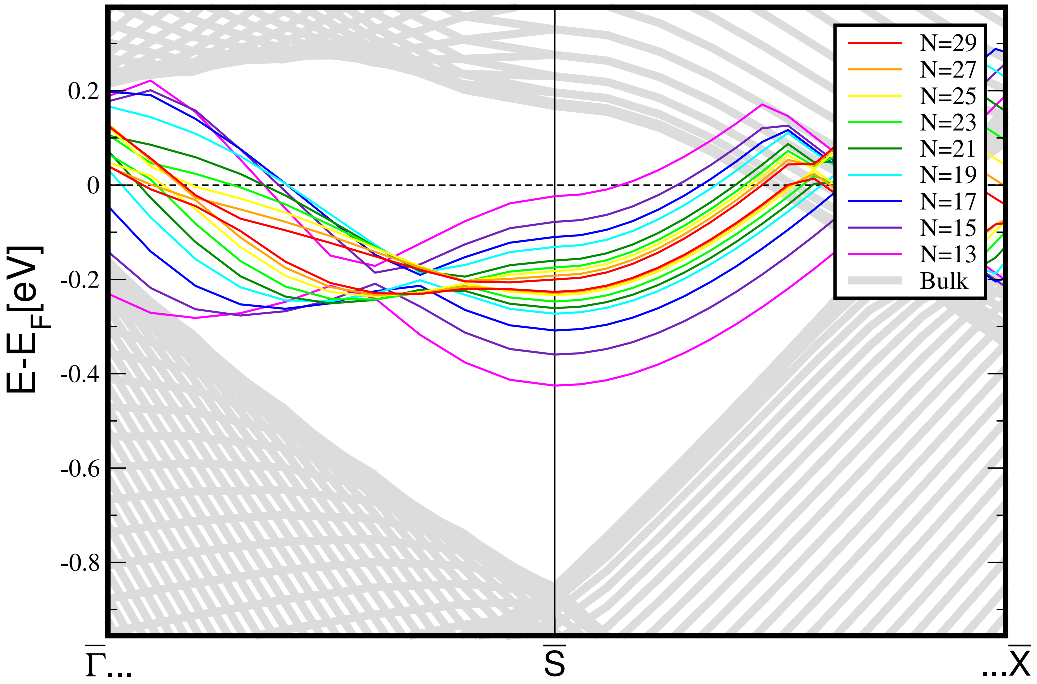

Figure 4.19: Surface state at the $\overline{S}$-point of Al(110).

In Fig. 4.20 splitting energies of surface states of Al(100) and Al(110), in Fig. 4.21 splitting energies of surface states of of Al(111) and Cu(100), and in Fig. 4.22 splitting energies of surface states of of Cu(110) and Cu(111) are plotted.

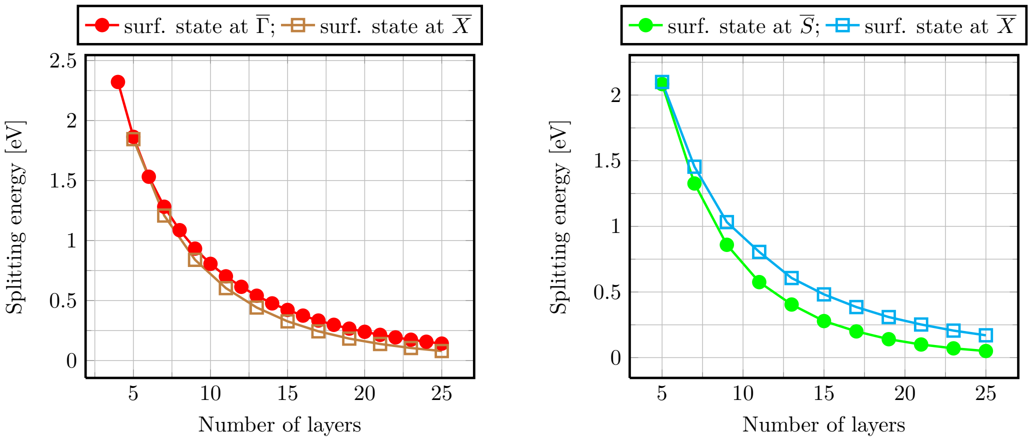

(a) Splitting energy of surface states at $\overline{\Gamma}$ and $\overline{X}$ of Al(100).

(b) Splitting energy of surface states at $\overline{S}$ and $\overline{X}$ of Al(110).

Figure 4.20: Splitting energy of surface states of Al(100) and Al(110).

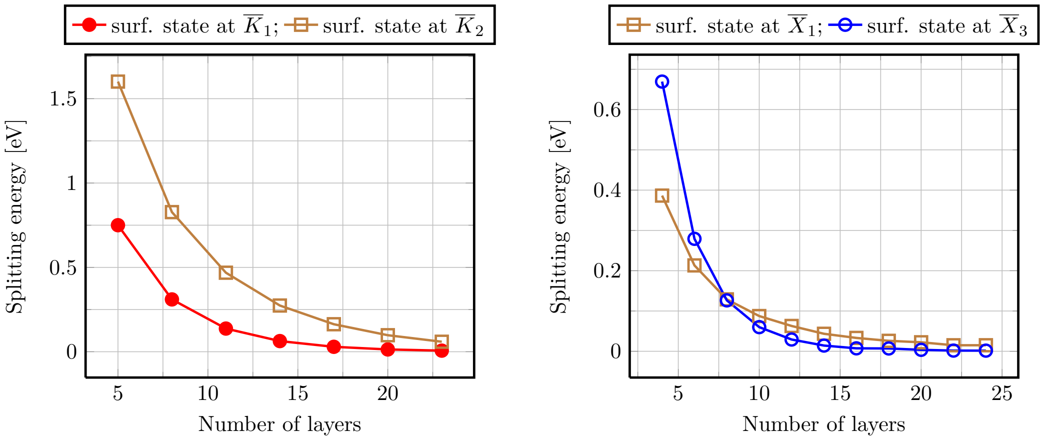

(a) Splitting energy of surface states at $\overline{K}$ of Al(111).

(b) Splitting energy of surface states at $\overline{X}$ of Cu(100).

Figure 4.21: Splitting energy of surface states of Al(111) and Cu(100).

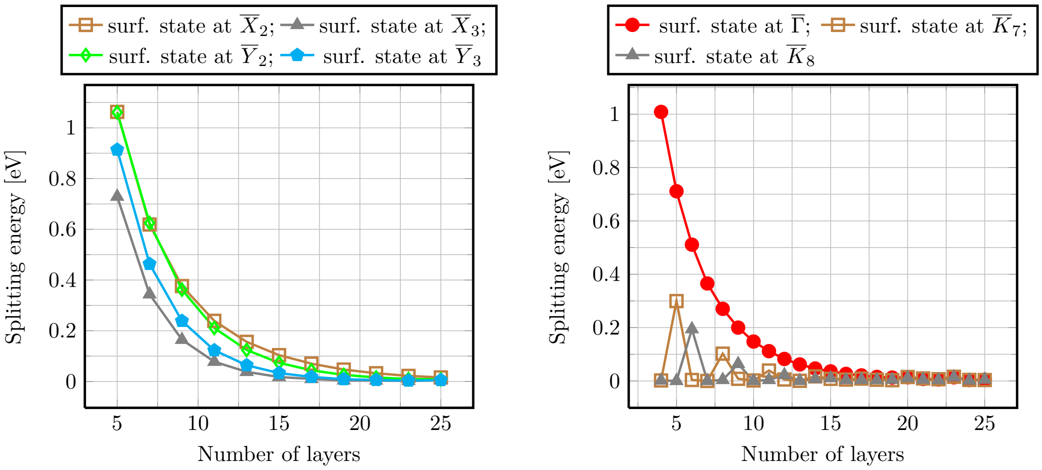

(a) Splitting energy of surface states at $\overline{X}$ and $\overline{Y}$ of Cu(110).

(b) Splitting energy of surface states at $\overline{\Gamma}$ and $\overline{K}$ of Cu(111).

Figure 4.22: Splitting energy of surface states of Cu(110) and Cu(111).

4.1.10 Effective electron mass

The energy of a free electron reads

$$E(k) = \frac{\hbar k^2}{2m_e}. \tag{4.17}$$

In the vicinity of a point $\mathbf{k}_0$ in the Brillouin zone, where a Shockley surface state is located, one can approximately describe the two-dimensional dispersion by a parabola

$$E(k) = E(\mathbf{k}_0) + \frac{\hbar\left(\mathbf{k} - \mathbf{k}_0\right)^2}{2m^*}, \tag{4.18}$$

where $m^* \equiv \tilde{m} \cdot m_{ele}$ is the effective electron mass. In order to compute the effective electron mass, a parabola is fitted into selected data points of the energy band of the surface state. In this thesis, the Levenberg-Marquardt algorithm has been used for the fit [29, 30]. The number of selected points for the parabolic fit is 5. However, as discussed in Sec. 4.1.9, there are always two energy bands for one surface state. Hence the effective mass has been computed for both, the lower and the upper band. One has to take into account that in general the effective electron mass is anisotropic. For this very reason the direction is specified, e.g. $\overline{\Gamma} \to \overline{X}$, which means that the surface state is located at the $\overline{\Gamma}$ point and the direction is towards the $\overline{X}$ point.

Two parameters have been used for the parabolic fit

$$E(k) = E_0 + E_1 \cdot k'^2, \tag{4.19}$$

namely E_0 and E_1. The parameter k_0 can directly be taken from the energy band, hence one can shift $k' = k - k_0$. In Fig. 4.23 a plot of such a fit is given. In order to point out the parabolic character of the surface band, all used data points except the minimum are reflected about the ordinate. However, although there is no need, since in the fitting function the linear term is dropped, the reflected data points have been used in the fit too.

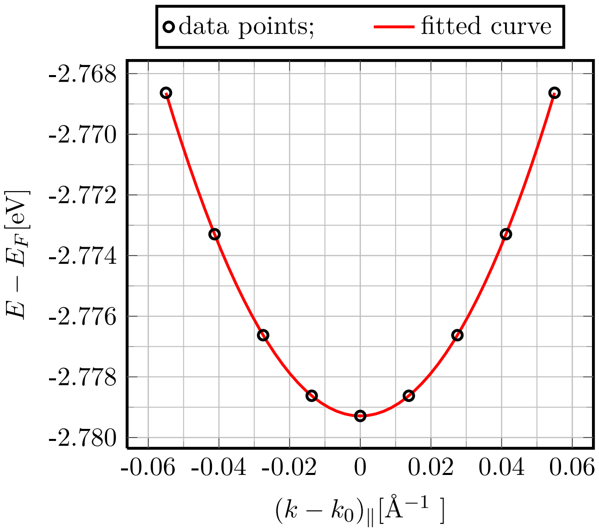

Figure 4.23: Parabolic fit into data points of a surface state energy band at the $\overline{\Gamma}$ point towards the $\overline{X}$ point of a 25-layer Al(100) slab.

In Fig. 4.24a the effective electron masses of the upper and lower energy bands of the surface state at $\overline{\Gamma}$ of Al(100) are plotted vs. the number of layers. To consider possible direction-dependences, two directions, $\overline{\Gamma} \to \overline{M}$ and $\overline{\Gamma} \to \overline{X}$, have been used.

However, the effective electron mass of this surface state has no anisotropic character due to the 4-fold symmetry of the (100) surface.

In Fig. 4.24b the effective electron masses of the upper and lower energy bands in the direction $\overline{X} \to \overline{S}$ of the surface state at $\overline{X}$ of Al(110) are plotted vs. the number of layers. One can notice, that for a small number of layers the effective electron mass depends upon whether the number of layers is even or odd. For increasing number of layers this effect vanishes.

In Fig. 4.25a, the effective electron masses of the upper and lower energy bands and in both directions, $\overline{K}_1 \to \overline{\Gamma}$ and $\overline{K}_1 \to \overline{M}$, of the surface state at $\overline{K}_1$ of Al(111) is plotted vs. the number of layers. The convergence of the effective electron mass is rather slow, but nevertheless one can state that the effective electron mass of this surface state is different for the two investigated directions.

For copper, a more extensive list of surface states has been found. For that reason in Fig. 4.25b only the lower energy bands have been used. In contrast to all other effective energy masses of Cu(100), the effective electron mass at $\overline{\Gamma}$ shows no anisotropic character as expected due to symmetry. One has to notice that the range of the ordinate is larger than those of the plots of the aluminium facets, so there is a larger spread in values.

In Fig. 4.26a the effective electron masses of the surface states of Cu(110) are

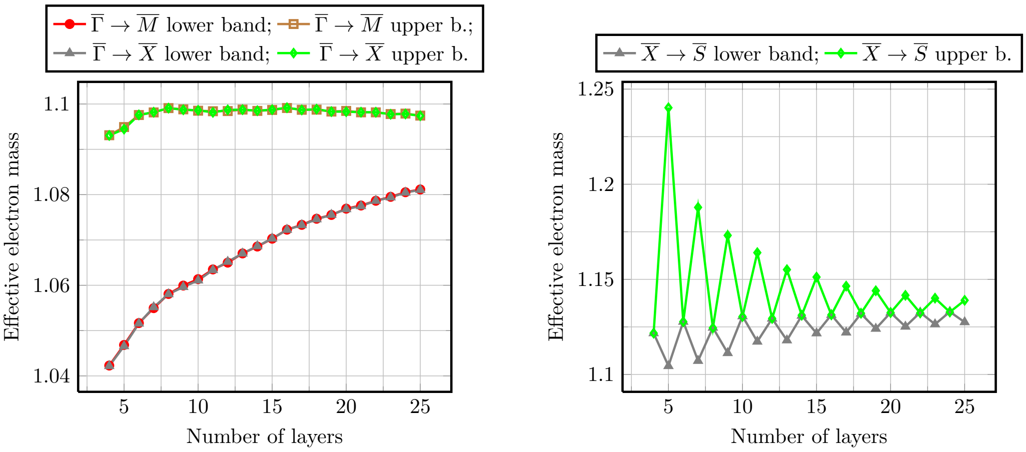

(a) Effective electron mass $\tilde{m} = m^*/m$ of the surface state at $\overline{\Gamma}$ of Al(100).

(b) Effective electron mass $\tilde{m} = m^*/m$ of the surface state at $\overline{X}$ of Al(110).

Figure 4.24: Effective electron mass $\tilde{m} = m^*/m$ of surface states of Al(100) and Al(110).

plotted vs. the number of layers. As for Al(110) one can notice, that for a small number of layers some effective electron masses depend on whether the number of layers is even or odd. In Fig. 4.26b the effective electron mass of the surface states $\overline{\Gamma}$, $\overline{K}_7$, and $\overline{K}_8$ are plotted. While for the surface states at $\overline{K}$ the effective electron masses have anisotropic behaviours, the effective electron mass of the surface state at $\overline{\Gamma}$ is isotropic. To summarise the investigation on the effective electron masses, all converged values are given in Tab. 4.4.

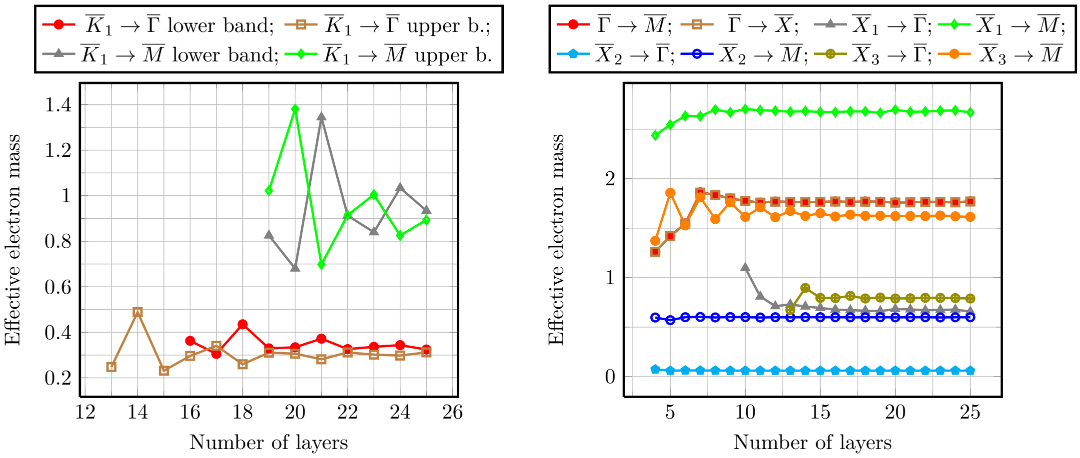

(a) Effective electron mass $\tilde{m} = m^*/m$ of the surface states at $\overline{K}$ (at 0.63 eV below the Fermi level) of Al(111). The labelling of the **k**-point refers to Tab. 4.2.

(b) Effective electron mass $\tilde{m} = m^*/m$ of surface states at $\overline{\Gamma}$ and $\overline{X}$ of Cu(100). The lower energy bands of the surface states has been used. The labelling of some **k**-points refers to Tab. 4.3.

Figure 4.25: Effective electron mass $\tilde{m} = m^*/m$ of surface states of Al(111) and Cu(100).

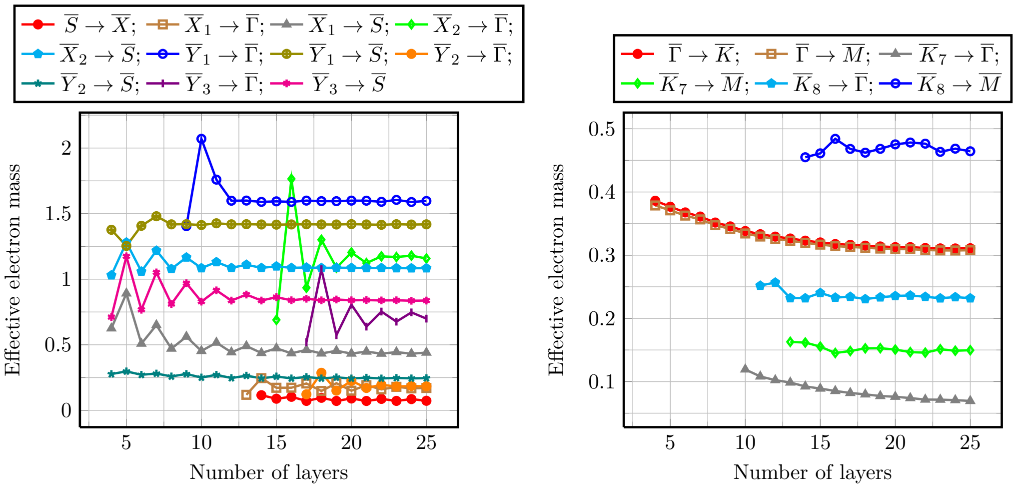

(a) Effective electron mass $\tilde{m} = m^*/m$ of surface states at $\overline{S}$, $\overline{X}$, and $\overline{Y}$ of Cu(110). The lower energy bands of the surface states has been used. The labelling of some **k**-points refers to Tab. 4.3.

(b) Effective electron mass $\tilde{m} = m^*/m$ of surface states at $\overline{\Gamma}$ and $\overline{K}$ of Cu(111). The lower energy bands of the surface states has been used. The labelling of some **k**-points refers to Tab. 4.3.

Figure 4.26: Effective electron mass $\tilde{m} = m^*/m$ of surface states of Cu(110) and Cu(111).

Table 4.4: Effective electron masses of surface states of aluminium and copper.

material	k-point	$E - E_F[eV]$	direction	$\tilde{m} = m^*/m$
Al100	$\overline{\Gamma}$	-2.72	$\overline{\Gamma} \to \overline{M}$	1.09
			$\overline{\Gamma} \to \overline{X}$	1.09
	$\overline{X}$	1.78	$\overline{X} \to \overline{\Gamma}$	0.05
			$\overline{X} \to \overline{M}$	1.11
Al110	$\overline{S}$	-0.22	$\overline{S} \to \overline{X}$	0.11
	$\overline{X}$	-2.79	$\overline{X} \to \overline{S}$	1.13
Al111	$\overline{K}$	-0.63	$\overline{K} \to \overline{\Gamma}$	0.3
			$\overline{K} \to \overline{M}$	0.9
Cu100	$\overline{\Gamma}$	-4.73	$\overline{\Gamma} \to \overline{M}$	1.77
			$\overline{\Gamma} \to \overline{X}$	1.77
	$\overline{X}$	-4.21	$\overline{X} \to \overline{\Gamma}$	0.65
			$\overline{X} \to \overline{M}$	2.66
	$\overline{X}$	-0.06	$\overline{X} \to \overline{\Gamma}$	0.06
			$\overline{X} \to \overline{M}$	0.60
	$\overline{X}$	3.19	$\overline{X} \to \overline{\Gamma}$	0.79
			$\overline{X} \to \overline{M}$	1.62
Cu110	$\overline{S}$	6.70	$\overline{S} \to \overline{X}$	0.08
	$\overline{X}$	1.69	$\overline{X} \to \overline{\Gamma}$	0.17
			$\overline{X} \to \overline{S}$	0.43
	$\overline{X}$	4.95	$\overline{X} \to \overline{\Gamma}$	1.16
			$\overline{X} \to \overline{S}$	1.08
	$\overline{Y}$	-4.49	$\overline{Y} \to \overline{\Gamma}$	1.60
			$\overline{Y} \to \overline{S}$	1.42
	$\overline{Y}$	-0.53	$\overline{Y} \to \overline{\Gamma}$	0.18
			$\overline{Y} \to \overline{S}$	0.24
	$\overline{Y}$	1.52	$\overline{Y} \to \overline{\Gamma}$	0.7
			$\overline{Y} \to \overline{S}$	0.84
Cu111	$\overline{\Gamma}$	-0.48	$\overline{\Gamma} \to \overline{K}$	0.31
			$\overline{\Gamma} \to \overline{M}$	0.31
	$\overline{K}$	3.67	$\overline{K} \to \overline{\Gamma}$	0.07
			$\overline{K} \to \overline{M}$	0.15
	$\overline{K}$	4.30	$\overline{K} \to \overline{\Gamma}$	0.23
			$\overline{K} \to \overline{M}$	0.47

4.1.11 Decay depth

Another characteristic property of a surface state is the exponential decay rate of the amplitude of the electron density, respectively, the electron wavefunction (see Sec. 2.3 where surface states are introduced). One can define a so-called decay depth z_0 of the envelope curve

$$n_{envelope}(z) = a_1 \exp\{-z/z_0\} \tag{4.20}$$

of the electron density. Taking into account that an N-layer slab has two surfaces, in this thesis a linear combination of two exponential functions is considered, thus

$$n_{envelope}(z) = a_1 \exp\{-z/z_0\} + a_2 \exp\{z/z_0\}. \tag{4.21}$$

Here, the z-coordinates are translated such that $z = 0$ is located in the middle of the slab. As already noted, for the effective electron mass, the Levenberg-Marquardt algorithm has been used for the non-linear fit. The fitting parameter of Eq. 4.21 are z_0, a_1, and a_2. The used initial values are $z_0 = 10$, $a_1 = 1$, and $a_2 = 1$. To avoid the fact that $n_{envelope}(z; z_0, a_1, a_2) \equiv n_{envelope}(z; z_0 \to -z_0, a_1 \to a_2, a_2 \to a_1)$, the constraints $z_0, a_1, a_2 \geq 0$ have been used. In Fig. 4.27 such a fit of the decay depth of a surface state of Al(111) is plotted.

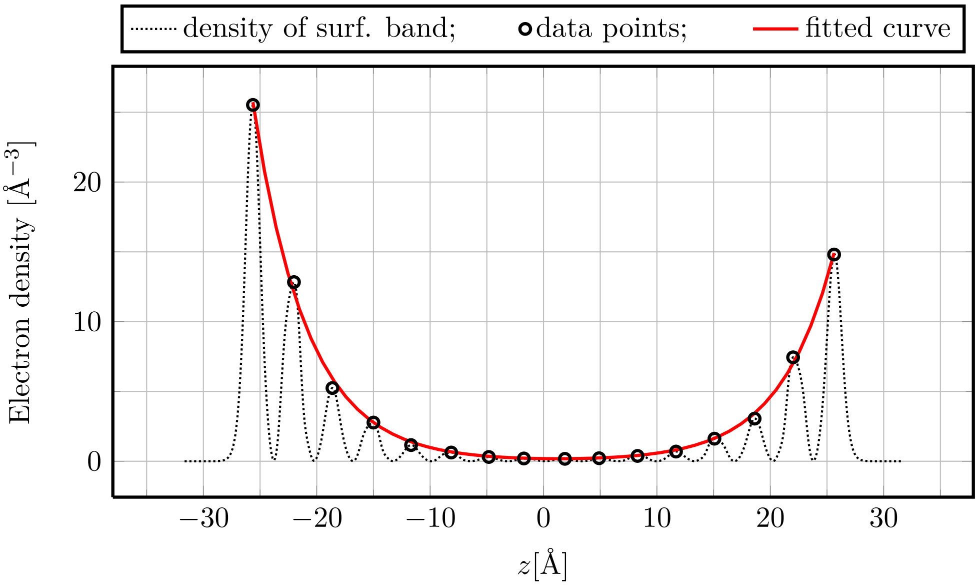

Figure 4.27: Non-linear fit for the decay depth of a surface state of Al(111). The surface state is located at the $\overline{K}$ point and at the energy 0.62 eV below the Fermi level. The data of a 23-layer slab is shown.

In Fig. 4.28 the decay depths of surface states of Al(100) and Al(110) are plotted vs. the number of layers. Compared to other quantities such as the effective electron mass, the decay depth has a slower convergence with respect to the number of layers. An example is the decay depth of the surface state at $\overline{\Gamma}$ of Al(100), where for 25 layers the value is not converged yet. For the decay depths of Al(110) one can notice, that for a small number of layers the decay depth depends slightly upon the fact whether the number of layers is even or odd. The layer sequence for the (110) surface is ABAB.. . For increasing number of layers this effect vanishes. However, for the surface state at $\overline{X}$ convergence is rather slow.

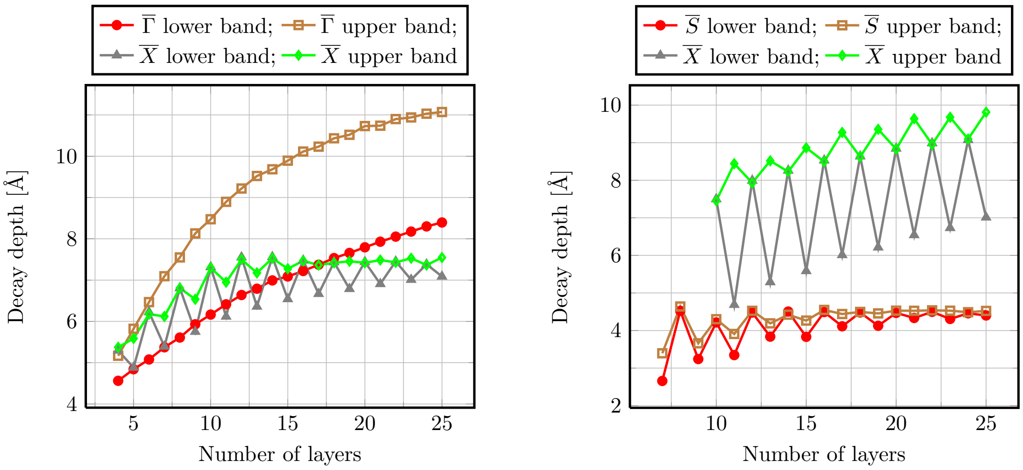

(a) Decay depths of surface states at $\overline{\Gamma}$ and $\overline{X}$ of Al(100).

(b) Decay depths of surface states at $\overline{S}$ and $\overline{X}$ of Al(110).

Figure 4.28: Decay depths of surface states of Al(100) and Al(110).

In Fig. 4.29 the decay depths of surface states of Al(111) and Cu(100) are plotted vs. the number of layers. The decay depths of Al(111) depend slightly upon the fact whether the modulo operation 'N mod 3' of the number of layers is zero, one or two, i.e. that the decay depths for $N = 8, 11, 14, ..$ has a slightly different behaviour than those for $N = 9, 12, 15, ..$ and those for $N = 10, 13, 16, ..$. The layer sequence for the (111) surface is ABCABC.. . For increasing number of layers this effect vanishes.

In Fig. 4.30 the decay depths of surface states of Cu(110) and Cu(111) are plotted vs. the number of layers. A list of the calculated decay depths is given in Tab. 4.5. The corresponding energy values can be used to find the surface states in the band structures in Figs. 4.7–4.12.

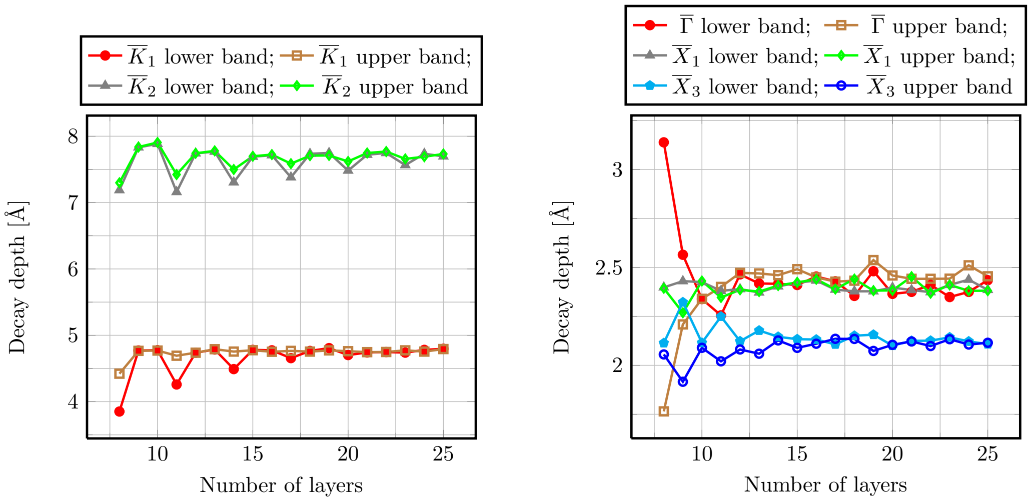

(a) Decay depths of surface states at $\overline{K}$ of Al(111).

(b) Decay depths of surface states at $\overline{\Gamma}$ and $\overline{X}$ of Cu(100).

Figure 4.29: Decay depths of surface states of Al(111) and Cu(100).

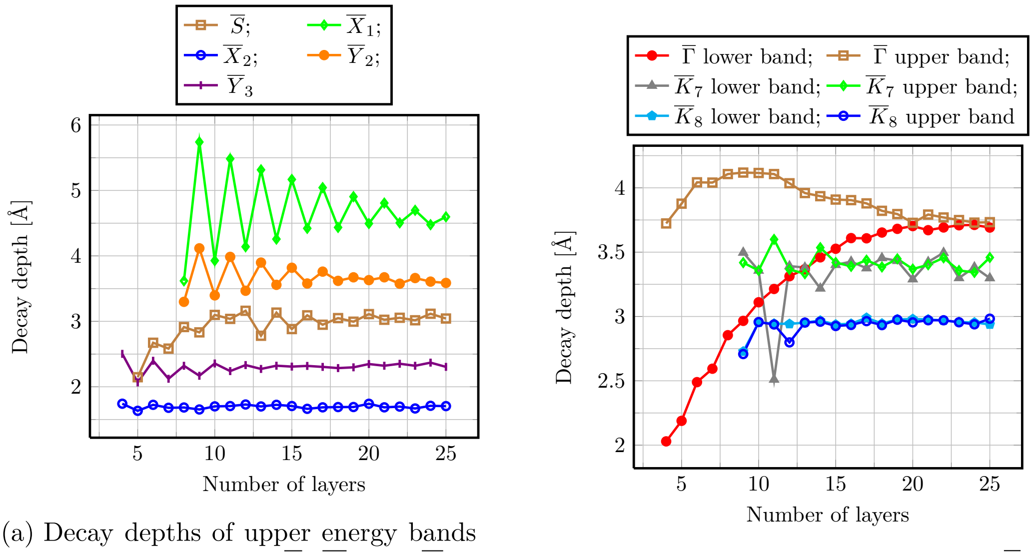

(a) Decay depths of upper energy bands of surface states at $\overline{S}$, $\overline{X}$, and $\overline{Y}$ of Cu(110).

(b) Decay depths of surface states at $\overline{\Gamma}$ and $\overline{K}$ of Cu(111).

Figure 4.30: Decay depths of surface states of Cu(110) and Cu(111).

Table 4.5: Decay depths of surface states of aluminium and copper.

material	k-point	$E - E_F [eV]$	Decay depth [Å]
Al100	$\overline{\Gamma}$	-2.72	12.0
	$\overline{X}$	1.78	7.4
Al110	$\overline{S}$	-0.22	4.5
	$\overline{X}$	-2.79	10.0
Al111	$\overline{K}$	-0.63	4.8
	$\overline{K}$	8.14	7.7
Cu100	$\overline{\Gamma}$	-4.73	2.4
	$\overline{X}$	-4.21	2.4
	$\overline{X}$	3.19	2.1
Cu110	$\overline{S}$	6.70	3.0
	$\overline{X}$	1.69	4.6
	$\overline{X}$	4.95	1.7
	$\overline{Y}$	-0.53	3.6
	$\overline{Y}$	1.52	2.3
Cu111	$\overline{\Gamma}$	-0.48	3.7
	$\overline{K}$	3.67	3.4
	$\overline{K}$	4.30	3.0

4.1.12 Photoemission intensity

Another possibility to find surface states, is to consider photoemission intensities. In this thesis the photoemission intensity has been calculated within the one-step-model and applying the dipole approximation. Therefore Eq. 3.62 has been used. In numerical applications the Dirac delta functional has to be replaced by a distribution function, e.g. the normal distribution.

$$f(x) = \frac{1}{\sigma\sqrt{2\pi}} \exp\left\{-\frac{(x-x_0)^2}{2\sigma^2}\right\} \tag{4.22}$$

The delta functional of Eq. 3.62 reads

$$\delta(E_i + \Phi + E_{kin} - \hbar\omega) \tag{4.23}$$

Since the polar emission angle, the azimuthal emission angle, and the kinetic energy E_{kin} can be transformed into a wavevector basis k_x, k_y, and k_z, the argument of the delta functional depends on the energy and the wavevector. Hence the broadening of the delta functional has to be performed in direction of the energy and in the three directions of the wavevector **k**. The broadening parameter is σ, σ_E for the energy broadening and σ_{k_x}, σ_{k_y}, and σ_{k_z} for the wavevector broadening. Furthermore a final state approach, described in Subsec. 3.3.2, has been applied. The universal curve visualized in Fig. 3.6 has been used to determine the inelastic mean free path IMFP.

In Fig. 4.31 the photoemission intensity of Cu(110) along the $k_{[001]}$-axis is plotted. The parameters in the calculation are $\hbar\omega = 30$ eV, $\sigma_{k_{[001]}} = 0.02$ Å^{-1} , $\sigma_E = 0.02$ eV, and IMFP $= 10$ Å. The red curves in the figure picture three surface states at the **k**-point $\overline{Y}$. The surface states at $E_B = -1.52$ eV and $E_B = 4.49$ eV are rather good visible in the contour plot of the photoemission intensity. In contrast to these states, the surface state at $E_B = 0.53$ eV is very close to the bulk projected bands. In order to specify this dispersion as a surface state in the photoemission intensity plot, it is needed to increase the number of points in the k-grid. For the calculation a Monkhorst-Pack meshgrid of 54x38x1 **k**-points has been used.

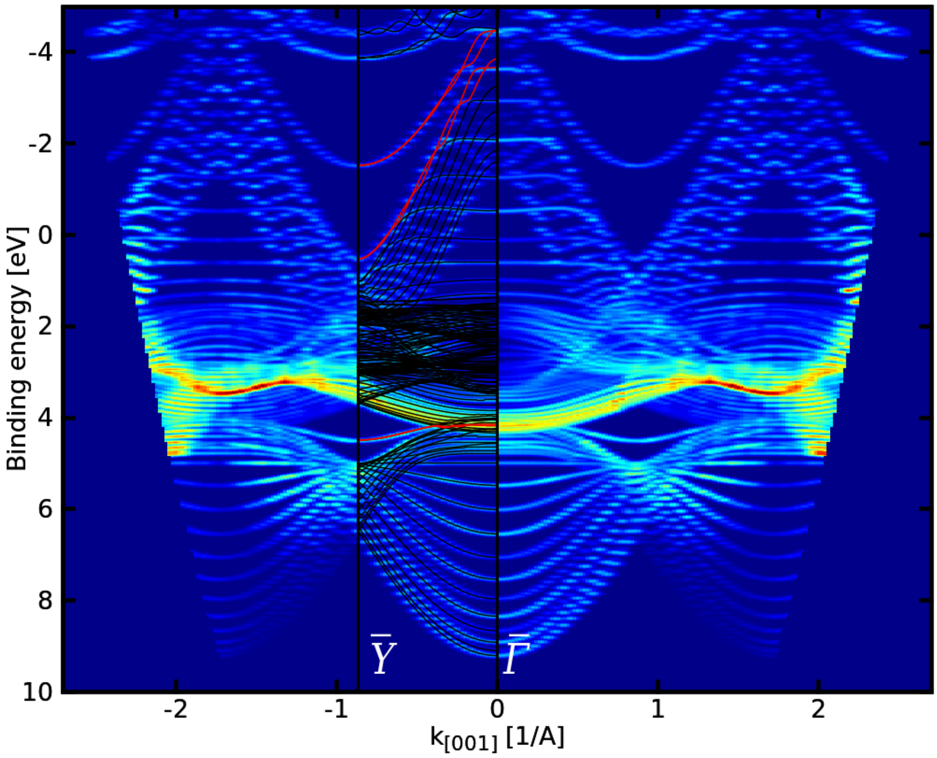

Figure 4.31: Photoemission simulation: E-vs-k-plot along the $k_{[001]}$-axis of a 25-layer Cu(110) slab. For the calculation a Monkhorst-Pack grid of 54x38x1 **k**-points has been used. Additionally, energy bands from $\overline{\Gamma}$ to $\overline{Y}$ are plotted on top of the photoemission intensity. The red curves denote surface states at $\overline{Y}$.

In Fig. 4.32 the photoemission intensity of Cu(110) along the $k_{[\bar{1}10]}$-axis is plotted. The parameters in the calculation are $\hbar\omega = 30$ eV, $\sigma_{k_{[\bar{1}10]}} = 0.02$ Å^{-1} , $\sigma_E = 0.02$ eV, and IMFP = 10 Å. A Monkhorst-Pack grid of 54x38x1 **k**-points has been used. The red curves in the figure picture two surface states at the **k**-point $\overline{X}$. The surface states are located at the binding energies $E_B = -1.69$ eV and $E_B = -4.95$ eV.

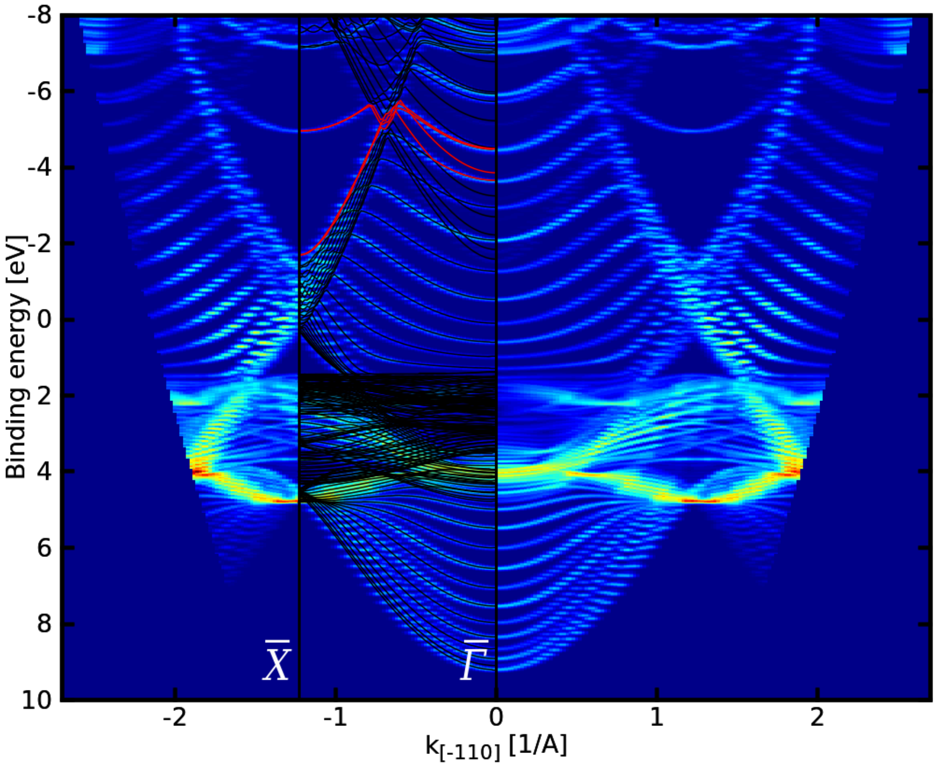

Figure 4.32: Photoemission simulation: E-vs-k-plot along the $k_{[\bar{1}10]}$-axis of a 25-layer Cu(110) slab. For the calculation a Monkhorst-Pack grid of 54x38x1 **k**-points has been used. Additionally, energy bands from $\overline{\Gamma}$ to $\overline{X}$ are plotted on top of the photoemission intensity. The red curves denote surface states at $\overline{X}$.

4.1.13 Summary of results

In Tab. 4.6 the surface energies and the work functions of the investigated surfaces are summarized. The results are compared to available experimental data, where a good agreement can be reached. The calculated work functions and surface energies tend to have slightly smaller values than those of the corresponding experimental values. The work functions of copper have a decreasing ordering from Cu(111), Cu(100) to Cu(110). Notice that in Fig. 4.17, the densities reaching into the vacuum have the same ordering. This is also expected for aluminium, but, however, Al(111) has a smaller work function than Al(110), for both, experimental and simulated data. For the surface energies, as expected, both materials have a decreasing ordering from (110), (100) to (111).

One can notice that in Tab. 4.7 the energy band positions, the effective electron masses, and the decay depths of the surface states are in a good agreement with experiments. Most energies of the surface states tend to have slightly smaller values than those of the corresponding experimental values. The slight energy shift of the energy bands is characteristic for DFT-GGA calculations.

Due to the symmetric property of the $\overline{\Gamma}$ point, all calculated effective electron masses at this special point are isotropic. Note that all other effective masses are anisotropic.

Table 4.6: Surface energy and work function of facets of Cu and Al.

	workf. $\Phi[eV]$		surf. energy $[eV]$	
material	this work	exp.	this work	exp.
Al100	4.26	4.41 [31]	0.48	
Al110	4.06	4.28 [31]	0.72	0.81 [32]
Al111	4.06	4.24 [31]	0.36	
Cu100	4.50	4.59 [33]	0.59	
Cu110	4.38	4.38 [33]	0.89	
Cu111	4.78	4.94 [33]	0.46	0.64 [24]

Table 4.7: Energy, effective mass and decay depth of selected surface states.

		$E - E_F [eV]$		$\tilde{m} = m^*/m$			decay depth [Å]
material	k-point	this work	exp.	direction	this w.	exp.	this w.
Al110	$\overline{S}$	-0.22	-0.2 [34]	$\overline{S} \rightarrow \overline{X}$	0.11		4.5
	$\overline{X}$	-2.79	-2.7 [34]	$\overline{X} \rightarrow \overline{S}$	1.13		10.0
Al100	$\overline{\Gamma}$	-2.72	-2.8 ± 0.2 [35]	$\overline{\Gamma} \rightarrow \overline{M}$	1.09	1.07 [36]	12
				$\overline{\Gamma} \rightarrow \overline{X}$	1.09	1.07 [36]	
	$\overline{X}$	1.78		$\overline{X} \rightarrow \overline{\Gamma}$	0.05		7.4
				$\overline{X} \rightarrow \overline{M}$	1.11		
Al111	$\overline{K}$	-0.63	-0.7 [35]	$\overline{K} \rightarrow \overline{\Gamma}$	0.3	0.32 ± 0.06 [37]	4.8
				$\overline{K} \rightarrow \overline{M}$	0.9		
Cu110	$\overline{Y}$	-0.53	-0.51 [2]	$\overline{Y} \rightarrow \overline{\Gamma}$	0.18	0.26 [2]	3.6
				$\overline{Y} \rightarrow \overline{S}$	0.24		
	$\overline{Y}$	1.52	1.8 ± 0.2 [38]	$\overline{Y} \rightarrow \overline{\Gamma}$	0.7	0.8 ± 0.2 [38]	2.3
				$\overline{Y} \rightarrow \overline{S}$	0.84		
	$\overline{X}$	4.95	5.4 ± 0.3 [38]	$\overline{X} \rightarrow \overline{\Gamma}$	1.16	2.0 ± 0.2 [38]	1.7
				$\overline{X} \rightarrow \overline{S}$	1.08		
Cu100	$\overline{\Gamma}$	-4.73		$\overline{\Gamma} \rightarrow \overline{M}$	1.77		2.4
				$\overline{\Gamma} \rightarrow \overline{X}$	1.77		
	$\overline{X}$	-0.06	-0.06 [39]	$\overline{X} \rightarrow \overline{\Gamma}$	0.06	0.16 [39]	
				$\overline{X} \rightarrow \overline{M}$	0.60		
Cu111	$\overline{\Gamma}$	-0.48	-0.44 [2]	$\overline{\Gamma} \rightarrow \overline{K}$	0.31	0.38 [2]	3.7
				$\overline{\Gamma} \rightarrow \overline{M}$	0.31	0.38 [2]	

4.2 Organic/metal interfaces

In this section, the interface of a monolayer comprised of organic molecules with a metallic surface is investigated. First, the molecule is introduced and a possible unit cell of the system is defined. Second, a convergence study with respect to the number of **k**-points and with respect to the number of substrate layers is performed. Then the photoemission intensity for a freestanding monolayer of molecules and for the covered substrate is calculated by using the one-step model - see Eq. 3.62. Finally the energy positions of two surface states of the system are investigated. To this end, photoemission intensity maps of the molecule-metal system are compared to the bandstructure of the clean metal.

4.2.1 Supercell of PTCDA on Ag(110)

The investigated material is a silver surface, Ag(110), covered with a monolayer of perylene-tetracarboxylic-dianhydride (PTCDA). This molecule/metal interface has attracted considerable interest over the last years and has been intensively studied, both, experimentally and theoretically [40, 41, 7, 8, 42]. A PTCDA molecule consists of 24 carbon (C) atoms, 8 hydrogen (H) atoms and 6 oxygen (O) atoms. To realize a DFT calculation of this system, its supercell has to be constructed. The choice of the supercell is taken from [41]. In Fig. 4.33 some views of the supercell are given. The supercell vectors are pictured as black arrows where a denotes the lattice parameter of silver for which we took the theoretical value $a = 4.16$ Å.

$$\mathbf{a}_1 = a \begin{pmatrix} 2 \\ 3/\sqrt{2} \\ 0 \end{pmatrix}, \; \mathbf{a}_2 = a \begin{pmatrix} -2 \\ 3/\sqrt{2} \\ 0 \end{pmatrix}, \; \mathbf{a}_3 = h_0 \begin{pmatrix} 0 \\ 0 \\ 1 \end{pmatrix} \qquad (4.24)$$

The height of the supercell is

$$h_0 = (N-1) \cdot \Delta h_0 + \Delta h_{PTCDA} + h_{\text{vac}} \qquad (4.25)$$

where N is the number of atomic silver layers, $\Delta h_0 = \frac{a}{2\sqrt{2}}$ is the (bulk) distance of adjacent substrate layers, Δh_{PTCDA} is the distance between the topmost substrate layer and the PTCDA-layer, and h_{vac} is the thickness of the vacuum. In the simulations the thickness of the vacuum was choosen to be $h_{\text{vac}} = 16$ Å.

As copper and aluminium, silver has a fcc structure. Hence, the layer sequence of Ag(110) is ABAB.. In contrast to the supercells of the clean metals in the first part of chapter 4, now one layer consists of 12 metal atoms instead of one. The $x-$ and

$y-$positions of the twelve Ag-atoms of layer A are as follows

$$\Big(\frac{3a}{2},\frac{7a}{2\sqrt{2}}\Big),\ \Big(\frac{3a}{2},\frac{5a}{2\sqrt{2}}\Big), \tag{4.26}$$

$$\Big(\frac{a}{2},\frac{9a}{2\sqrt{2}}\Big),\ \Big(\frac{a}{2},\frac{7a}{2\sqrt{2}}\Big),\ \Big(\frac{a}{2},\frac{5a}{2\sqrt{2}}\Big),\ \Big(\frac{a}{2},\frac{3a}{2\sqrt{2}}\Big), \tag{4.27}$$

$$\Big(-\frac{a}{2},\frac{9a}{2\sqrt{2}}\Big),\ \Big(-\frac{a}{2},\frac{7a}{2\sqrt{2}}\Big),\ \Big(-\frac{a}{2},\frac{5a}{2\sqrt{2}}\Big),\ \Big(-\frac{a}{2},\frac{3a}{2\sqrt{2}}\Big), \tag{4.28}$$

$$\Big(-\frac{3a}{2},\frac{5a}{2\sqrt{2}}\Big),\ \Big(-\frac{3a}{2},\frac{3a}{2\sqrt{2}}\Big) \tag{4.29}$$

The $x-$ and $y-$positions of the twelve Ag-atoms of layer B are

$$\big(0,0\big),\ \Big(0,\frac{a}{\sqrt{2}}\Big),\ \Big(0,\frac{2a}{\sqrt{2}}\Big),\ \Big(0,\frac{3a}{\sqrt{2}}\Big),\ \Big(0,\frac{4a}{\sqrt{2}}\Big),\ \Big(0,\frac{5a}{\sqrt{2}}\Big), \tag{4.30}$$

$$\Big(a,\frac{2a}{\sqrt{2}}\Big),\ \Big(a,\frac{3a}{\sqrt{2}}\Big),\ \Big(a,\frac{4a}{\sqrt{2}}\Big), \tag{4.31}$$

$$\Big(-a,\frac{2a}{\sqrt{2}}\Big),\ \Big(-a,\frac{3a}{\sqrt{2}}\Big),\ \Big(-a,\frac{4a}{\sqrt{2}}\Big) \tag{4.32}$$

A relaxation of the first two layers at the surface connected to the molecule-monolayer is performed by using 5 substrate layers in total. This relaxed distances are taken for all other supercells with different number of substrate layers in order to avoid geometrical effects and to highlight effects due to the variation of the number of substrate layers. The relaxed geometries for the PTCDA molecule are taken from [8]. A visualization of the supercell for a 15-layer Ag(110) slab, covered with a PTCDA monolayer, is given in Fig. 4.33. The unit cell vectors are displayed by the black arrows. The directions $[1\bar{1}\bar{1}]$ and $[1\bar{1}1]$ of the unit cell vectors denoted in Fig. 4.33a refer to the silver (110) layers, which are defined in Fig. 2.2h.

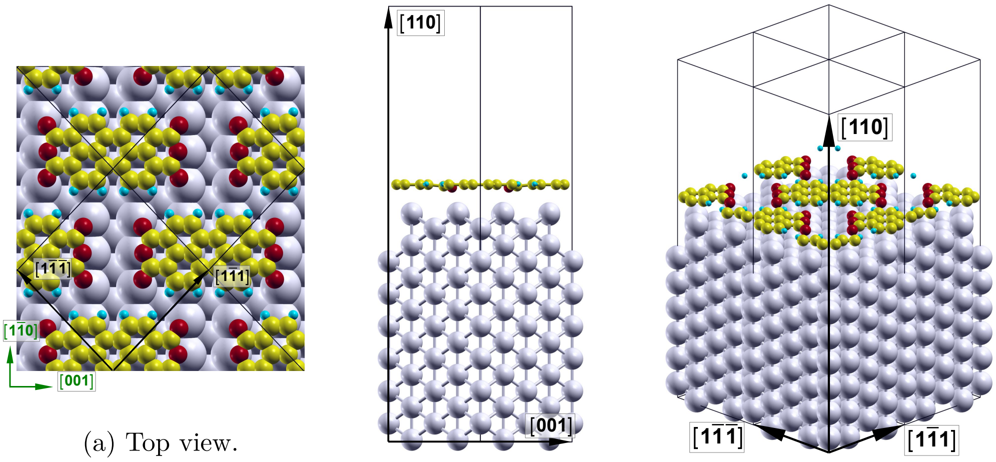

(a) Top view.

(b) Side view.

(c) Diagonal view.

Figure 4.33: PTCDA on Ag(110).

4.2.2 Density of states (DOS)

In this subsection a convergence study is performed in order to find out how many **k**-points are needed to obtain converged density of states (DOS) curves. Fig. 4.34 shows the DOS of a free standing PTCDA monolayer and the projected DOS (pDOS) of a PTCDA monolayer on 5 Ag(110) layers. Here, the pDOS is the contribution to the DOS from the PTCDA ions only. The black dashed line indicates the energy of the highest occupied molecule orbital (HOMO) respectively at the former highest occupied molecule orbital (FHOMO). The red dashed line indicates the energy of the lowest unoccupied molecule orbital (LUMO) respectively at the former lowest unoccupied molecule orbital (FLUMO). We see that the DOS of the free-standing layer is already converged with a k-grid of 6x6x1. Similarly, also the PTCDA/Ag(110) interface exhibits a converged pDOS spectrum when using a 6x6x1 k-grid. We note that already for a 3x3x1 k-grid, reasonably converged results can be expected.

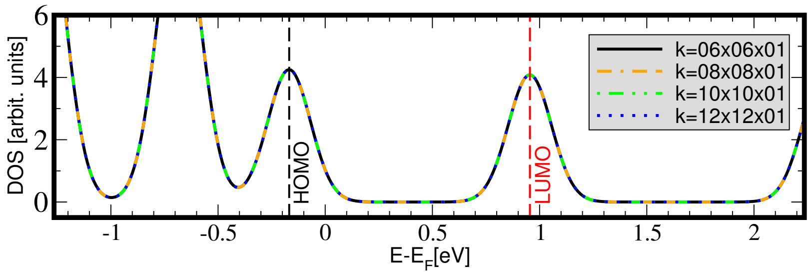

(a) Free standing PTCDA monolayer.

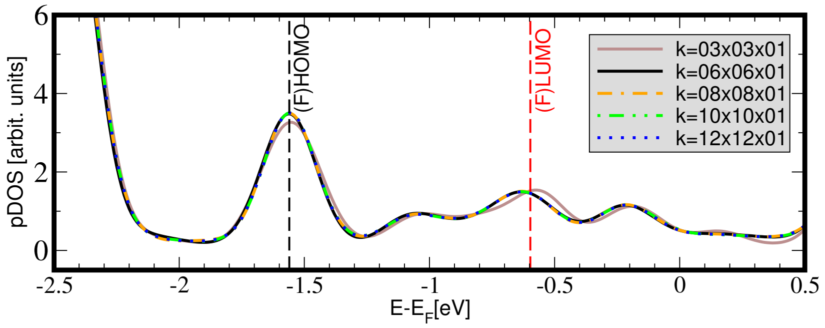

(b) 5 layers Ag(110) covered with PTCDA.

Figure 4.34: pDOS of PTCDA on Ag(110).

In addition to the convergence with respect to the number of **k**-points, we have also studied the convergence of the pDOS spectrum with respect to the number of metallic layers. We have varied the number of Ag-layers from 4–25 layers and evaluated the pDOS (Fig. 4.35). Note that all calculations are based on the relaxed adsorption geometry obtained for the 5-layer slab [8], and that Ag-layers have simply be added at the bottom of the slab by assuming the bulk layer spacings. While the shape and position of the HOMO-related peak in the pDOS shows a weak influence on the number of Ag-layers, there is a strong layer-dependence for the FLUMO-feature shown in Fig. 4.35. In particular, we observe a pronounced 'even-odd' dependence:

While the FLUMO seems to consists of three distinct peaks for the odd number of layers, particularly, in the range from 5–11, the pDOS for the even-numbered slabs always exhibits only one peak.

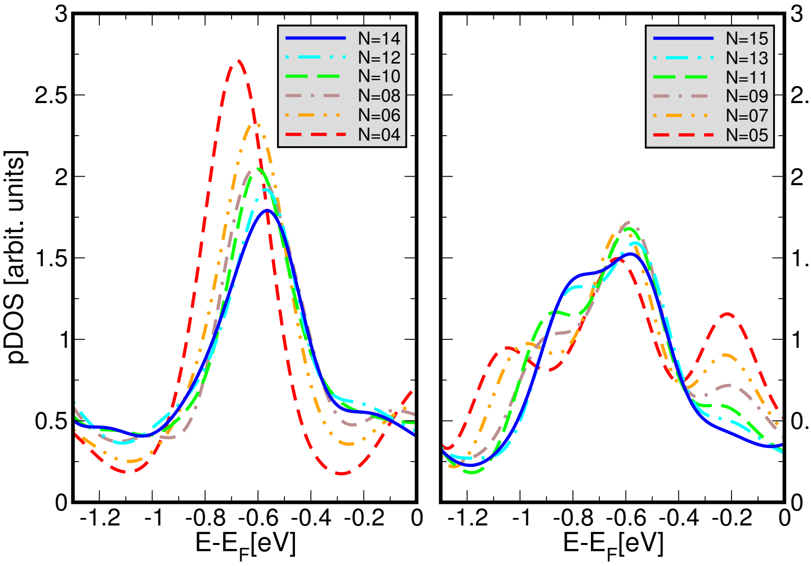

(a) $N = 4, 5, 6, .., 15$; k-mesh=6x6x1

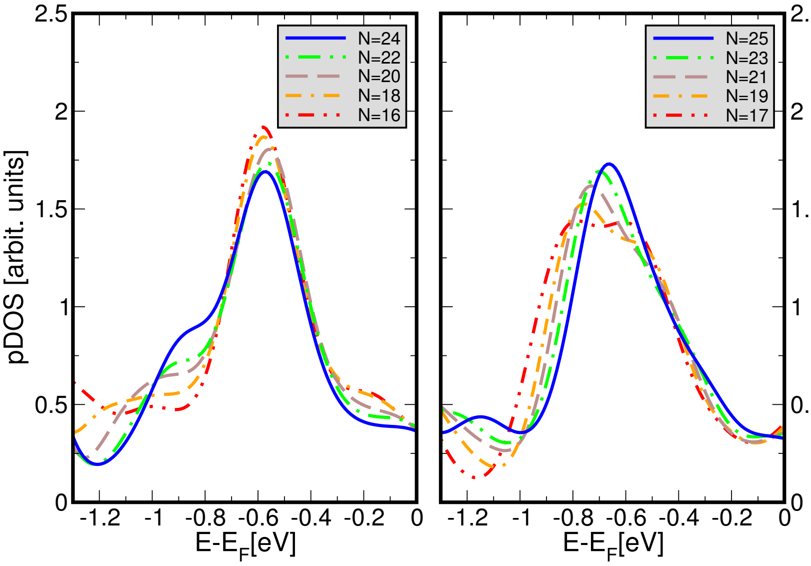

(b) $N = 16, 17, .., 25$; k-mesh=3x3x1

Figure 4.35: pDOS of PTCDA on Ag(110) at FLUMO.

In Fig. 4.36 the values of (F)HOMO and (F)LUMO in terms of the binding energy against the number of substrate layers are plotted.

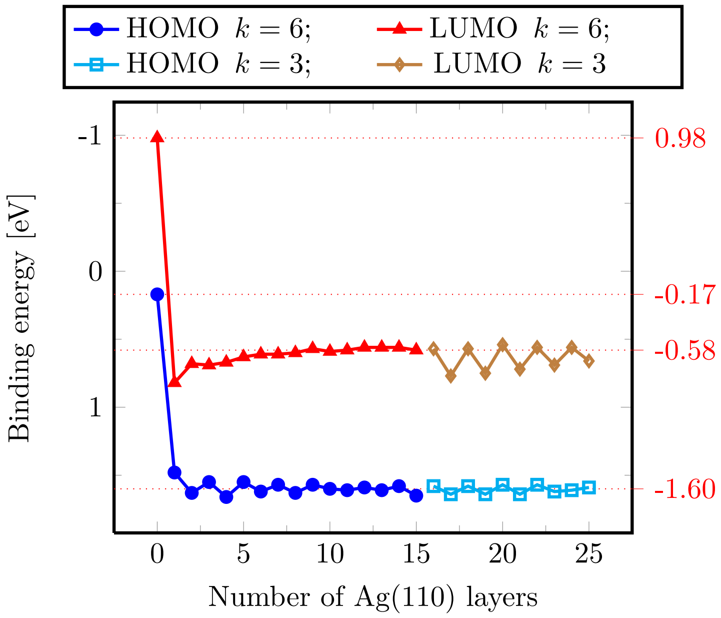

Figure 4.36: Binding energy of (F)HOMO and (F)LUMO of PTCDA on Al(110).

4.2.3 Work function

The supercell depicted in Fig. 4.33 is an asymmetric slab, *i.e.*, the PTCDA-monolayer is only on one side which implies different work functions on each side. This can lead to a convergence problem in the Kohn-Sham algorithm because due to periodic boundary conditions on the supercell, the potential at an arbitrary point on the boundary must be equal to its opposite point. Introducing a dipole in the vacuum area does solve this problem [28]. In VASP this method is already implemented. The use of the dipole correction scheme is easily done by setting the corresponding VASP-tags.

```
IDIPOL=3
LDIPOL=.TRUE.
```

The tag LDIPOL=.TRUE. switches on the potential correction mode. The tag IDIPOL=3 switches on the monopole, dipole and the quadrupole corrections. Another optional tag is the DIPOL-tag which specifies the position of the dipole in the supercell. If this tag is not set, then VASP places the dipole where the electron charge density averaged over a plane (xy-plane) has a minimum, that is in the middle of the vacuum layer.

Fig. 4.37 shows the plane-averaged electro-static potential of a 15 layer Ag(110) slab covered with a PTCDA-monolayer. The vertical dashed lines display the z-positions of the metal layers and the z-position of the PTCDA layer. Φ_0 is the work function of the unrelaxed clean metal surface and Φ is the work function of the covered metal surface. The work function Φ is needed for further photoemission calculations. Moreover, one can notice the small step of the potential in the vacuum at $z \approx 32$ Å, which is a consequence of the added dipole layer. In Fig. 4.38 the work function Φ against the number of substrate layers is plotted. As for the pDOS, the values appear to oscillate between even and odd numbers of layers before a convergence is reached.

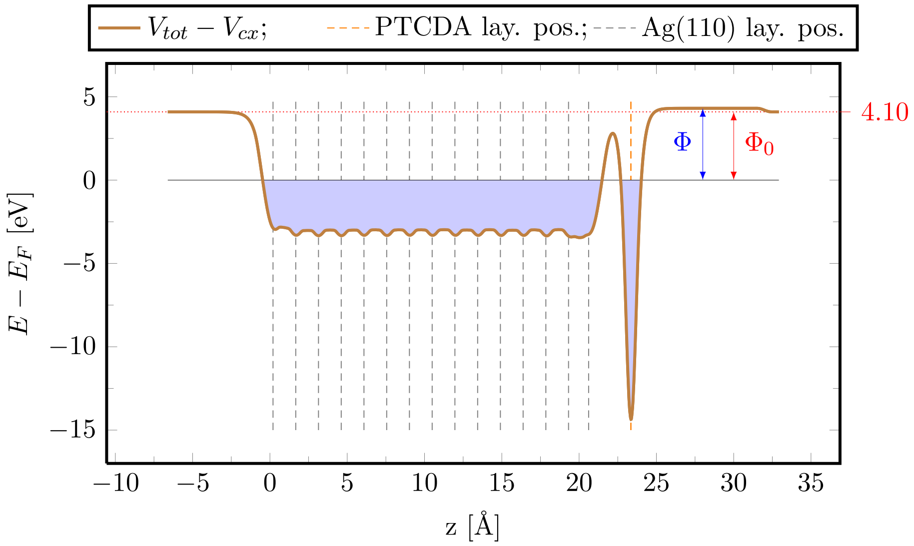

Figure 4.37: Hartree potential plus core-potential of PTCDA on 15 layers Ag(110).

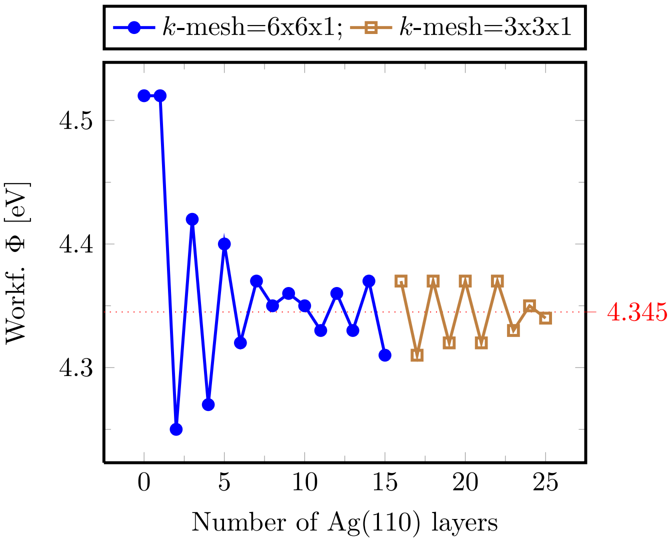

Figure 4.38: Work function of PTCDA on Ag(110).

4.2.4 Photoemission intensity

Due to the adsorbed PTCDA molecule, the number of Ag(110) atoms in the unit cell is set to 12. While for the clean Ag(110) surface a band structure plot is useful, the bandstructure for the PTCDA/Ag(110) interface would be difficult to interpret due to multiple band-folding into the much reduced Brillouin zone of the supercell. By calculating the photoemission intensity, more insights into the electronic structure of the interface can be gained and a better comparison with experimental data is enabled. To this end, we have computed the ARPES intensity within the one-step model of photoemission as described in Sec. 3.3 given by Eq. 3.62.

Before we analyse results for the PTCDA/Ag(110) interface, we compute the ARPES intensity for a freestanding layer of PTCDA molecules. Note that for these calculations the geometry of the PTCDA layer is frozen in the state which it exhibits when it is adsorbed. Fig. 4.39 and 4.40 show momentum maps at the HOMO and LUMO energy, respectively. A momentum map displays the angular distribution of the photo-current at a fixed binding energy. In these figures, we show two sets of experimental data taken from Refs. [7, 8] and compare them to simulated momentum maps for a free-standing layer of PTCDA. For these simulations, the following parameters have been used: $\hbar\omega = 30$ eV, $\sigma_{k_{[001]}} = \sigma_{k_{[1\bar{1}0]}} = 0.1$ Å^{-1}, $\sigma_E = 0.1$ eV, and IMFP $= 10$ Å. We note an overall good agreement between the experimental and theoretical momentum maps, in particular for the HOMO. On closer inspection, the experimental map for LUMO, in particular the data taken from Ref. [7], exhibits an additional peak at normal emission, that is at the center $k_{[001]} = k_{[1\bar{1}0]} = 0$, while the other experiment (the right semi circle in Fig. 4.40b) does not show such a peak at $k_{[001]} = k_{[1\bar{1}0]} = 0$ [8]. In Ref. [7], it was argued that a possible origin for this

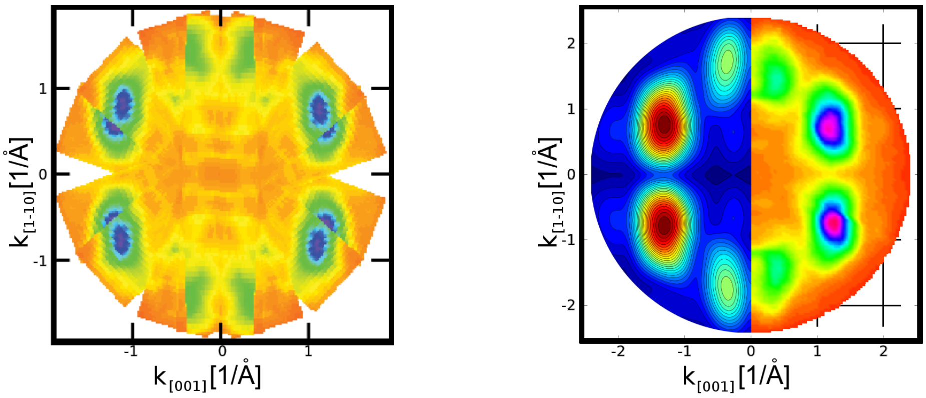

(a) Experiment of PTCDA on Ag(110) taken from [7].

(b) Left semi-circle: Simulation of a free PTCDA monolayer. Right semi-circle: Experiment of PTCDA on Ag(110) taken from [8].

Figure 4.39: Photoemission intensity maps of PTCDA on Ag(110) at (F)HOMO.

peak could be the hybridization between the LUMO and metallic states. It must be noted that due to different experimental geometries in the two experiments, the polarization factor appearing in the formula of the one-step-model may explain the discrepancy in the two sets of experimental data with respect to this normal emission feature.

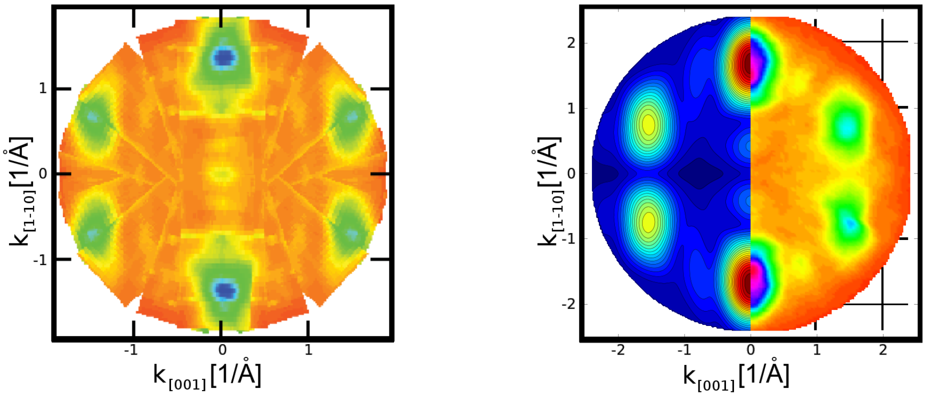

(a) Experiment of PTCDA on Ag(110) taken from [7].

(b) Left semi-circle: Simulation of a free PTCDA monolayer. Right semi-circle: Experiment of PTCDA on Ag(110) taken from [8].

Figure 4.40: Photoemission intensity maps of PTCDA on Ag(110) at (F)LUMO.

In order to clarify whether, this normal emission peak indeed arises from hybridization, we have also simulated the photoemission intensity for the PTCDA/Ag(110) interface within the one-step model. In addition to constant binding energy (CBE) momentum maps, we have also computed band maps, that is, maps of the photoemission intensity as a function of binding energy and parallel momentum vector for a fixed emission plane. Fig. 4.41 shows such band maps for an emission plane which is rotated by 32°with respect to the $k_{[001]}$ axis (note that this emission plane is highlighted in Fig. 4.43a). The left panel displays experimental data while the middle and right panels show simulated maps for PTCDA adsorbed on a 14 and 15 layer slab, respectively. The reason for taking a 32° rotated plane is that under such an angle peaks from both, the FHOMO and FLUMO, can be obtained in one band map. Note that the HOMO orbital has nodal planes both along the x and y direction, so no significant photoemission intensity is to be expected for these emission directions. One can clearly identify the three molecular features denoted as M1, M2 and M3 in Ref. [8] also in the simulated band maps, where M1 refers to the FLUMO, M2 to the HOMO, and M3 to a set of 4 π-orbitals. When comparing simulated results for 14 and 15 layers of Ag atoms, we observe the same tendency as has already observed for the pDOS. An even number of layers gives rise to only one peak for the FLUMO, while for the odd number of layers, the FLUMO splits into three peaks. In comparison to experiment, both simulations show stronger contributions from the substrate *sp* bands, in particular parabolic-like bands around the $\overline{\Gamma}$ point in the binding energy range from 0 to 3 eV at $k_{||} = 0$. The number and energy position of these silver-derived bands strongly change with the number of silver layers. We have performed a convergence study with respect to the number of layers which reveals that the number of such silver bands continues to grow with increasing number of layers, and that their energy positions do not converge to any special energy position. In order to analyse, band maps of the FLUMO energy region further, we have computed bands maps along the $k_{[1\bar{1}0]}$ axis in which the FLUMO shows a pronounced peak. Fig. 4.42 compares experimental data of such a band map [7] with simulated maps for PTCDA on a 14 and on a 15 layer slab, respectively. One clearly observes that in contrast to Fig. 4.42b (14 layers), one has three intensity peaks at the FLUMO area in Fig. 4.42c (15 layers) in agreement with the investigations on the pDOS in Subsection 4.2.2. The convergence study from 4 to 25 numbers of silver layers N has shown that for increasing N the three intensity peaks move to one energy position and superpose to one peak only. In order to investigate the sensitivity of the molecule-derived photoemission intensity on the number of Ag-layers further, we have also simulated CBE maps for a 14 and a 15 layer computation which are shown in Fig. 4.43. Here, Fig 4.43a shows a FLUMO map of the 14 layer slab at $E_1 = 0.56$ eV which equal to the peak position of the pDOS in the FLUMO region. Figs. 4.43b–4.43d, on the other hand are maps simulated for a 15 layer slab at binding energies $E_2 = 0.59$ eV, $E_3 = 0.85$ eV, and $E_4 = 1.65$ eV, respectively. Thus, the first two maps show the FLUMO region while the last map is at the maximum of the HOMO. In Fig. 4.43c, there is a peak at the center $k_{[001]} = k_{[1\bar{1}0]} = 0$ similar to what has been observed experimentally in Ref. [7]. Figs. 4.41b and 4.41c, however, identify the peak as a minimum of a parabolic silver energy band. Thus, the convergence study with respect to the num-

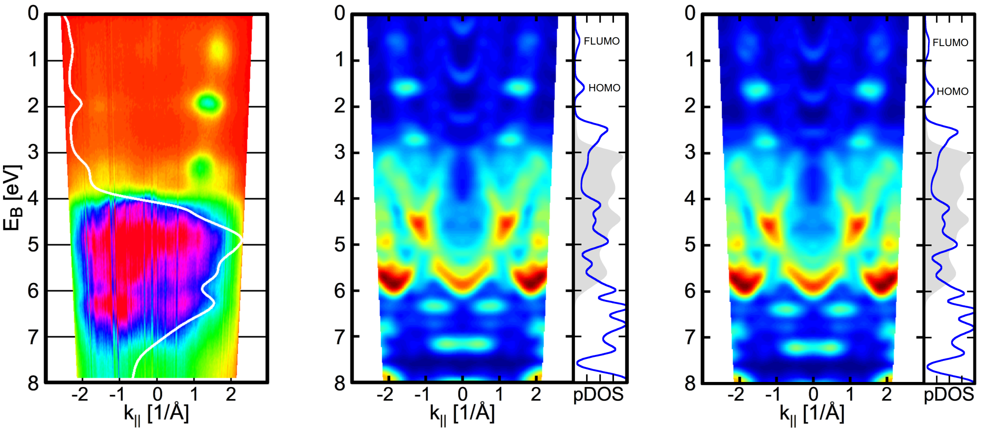

(a) Experiment of PTCDA on Ag(110) - taken from [8].

(b) Simulation of PTCDA on 14-layer Ag(110).

(c) Simulation of PTCDA on 15-layer Ag(110).

Figure 4.41: Energy-momentum maps of PTCDA on Ag(110) along the 32°-rotated $k_{[001]}$-axis.

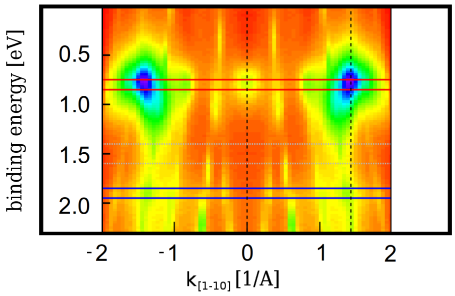

(a) ARPES intensity experiment of PTCDA on Ag(110) - taken from [7].

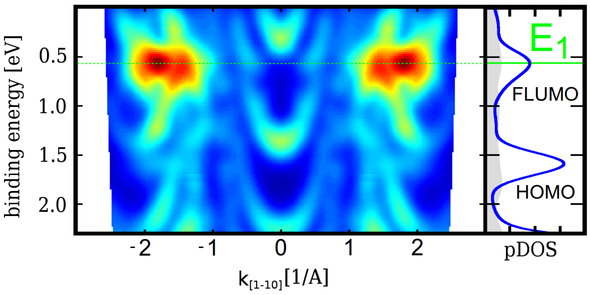

(b) Simulation of PTCDA on 14-layer Ag(110).

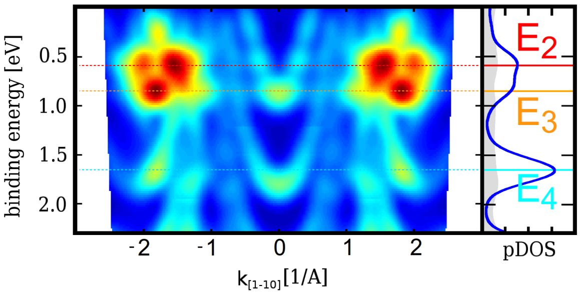

(c) Simulation of PTCDA on 15-layer Ag(110).

Figure 4.42: Energy-momentum maps of PTCDA on Ag(110) along the $k_{[1\bar{1}0]}$-axis.

ber of silver layers shows that the appearance of this peak at the energy position of the high binding energy side of the FLUMO peak may only be accidental. This is further demonstrated by the fact that no such peak appears in the 14 layer calculation. In summary, we can state that a variation over the number of layers (4–25) did not show a convergence of the FLUMO map with respect to intensity at the $\overline{\Gamma}$ point and that the accidental appearance of normal emission intensity arises from band minima of Ag *sp* bands which are moving through the energy position of the FLUMO. Thus, we conclude that the origin of the experimentally observed normal emission peak (see Fig. 4.40a) could not be clarified.

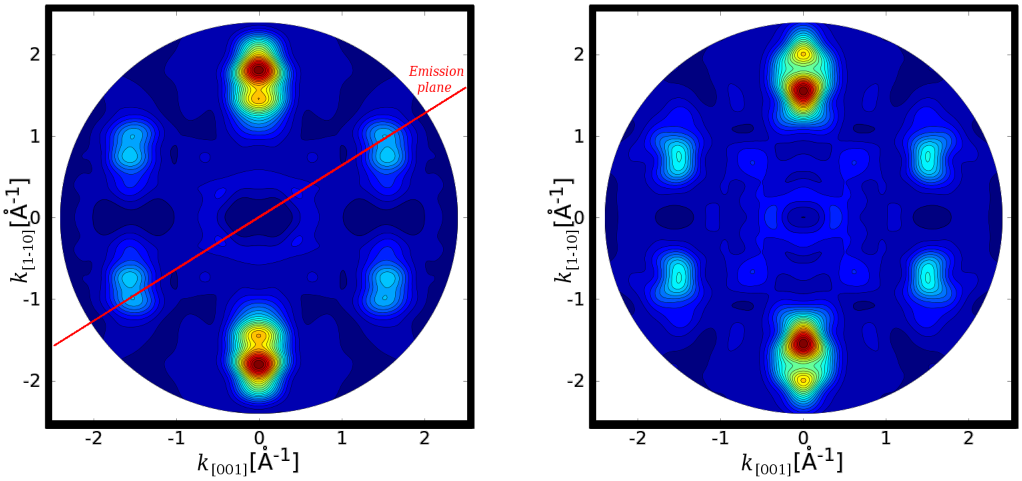

(a) Momentum-map of PTCDA on 14 layers Ag(110) at the binding energy $E_1 = 0.56$ eV (at FLUMO).

(b) Momentum-map of PTCDA on 15 layers Ag(110) at the binding energy $E_2 = 0.59$ eV (at FLUMO).

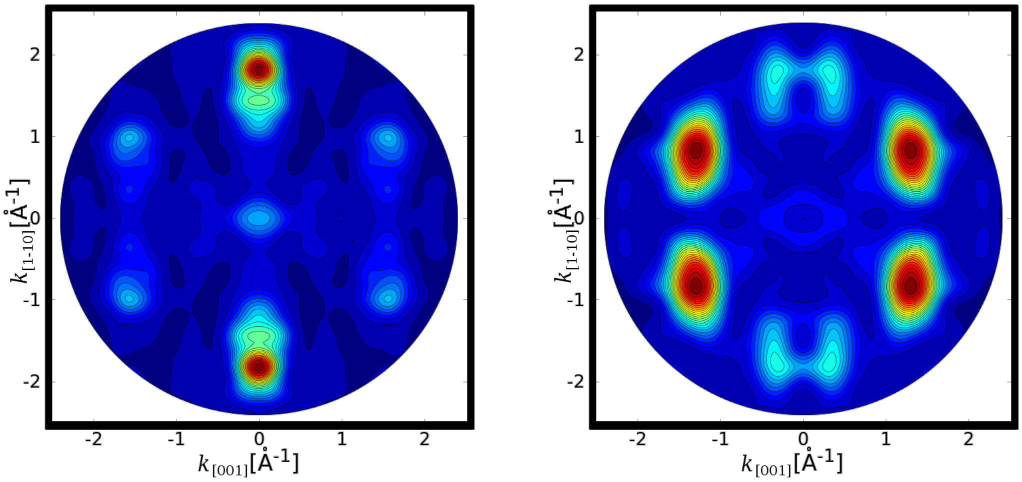

(c) Momentum-map of PTCDA on 15 layers Ag(110) at the binding energy $E_3 = 0.85$ eV (at FLUMO).

(d) Momentum-map of PTCDA on 15 layers Ag(110) at the binding energy $E_4 = 1.65$ eV (at FHOMO).

Figure 4.43: Momentum-maps of PTCDA on Ag(110) at the binding energies E_1, E_2, E_3, and E_4 defined in Fig. 4.42.

4.2.5 Surface state

The sensitivity of the FLUMO feature on the amount of Ag-layers and the fact whether an even or odd number is used, both for the pDOS spectra and in the photoemission maps, may suggest that a surface state of Ag(110) substrate may play a role in the hybridization of the molecular LUMO with the metal. To this end, we attempt to investigate how surface states of an uncovered Ag(110) surface are modified upon adsorption of PTCDA by analysing photoemission intensity maps. Fig. 4.44 compares the photoemission intensity of PTCDA on 15 layers Ag(110) to the bandstructure from $\overline{\Gamma}$ to $\overline{Y}$ of an *uncovered* 15-layer Ag(110) slab. Note that in this figure, also states above the Fermi level ($E = 0$ eV) are shown simply by neglecting the respective Fermi-Dirac factor in the evaluation of the photoemission intensity. The red lines denote the bands of the two surface states detected via bulk-projected band structures, both located at the $\overline{Y}$-point, one at the binding

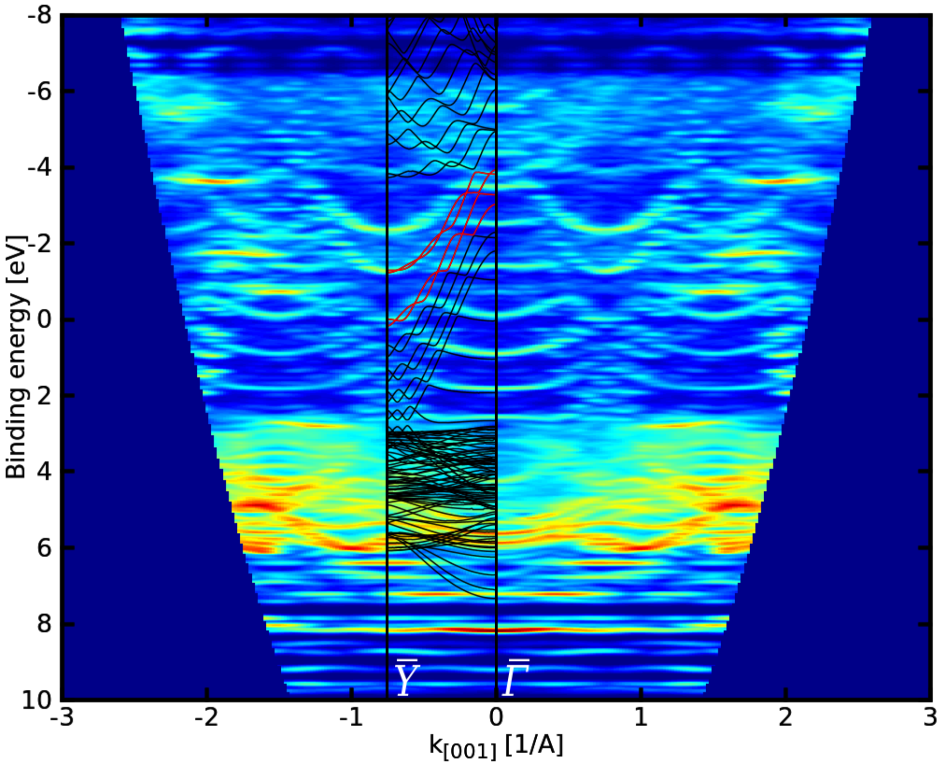

Figure 4.44: Photoemission simulation: Band map with an emission plane along the $k_{[001]}$-axis of a 15-layer Ag(110) slab covered with a PTCDA monolayer. Additionally, energy bands from $\overline{\Gamma}$ to $\overline{Y}$ of a clean 15-layer Ag(110) slab are plotted onto the photoemission intensity. The red curves picture surface states at $\overline{Y}$.

energy $E_B = -1.24$ eV and the other one at the binding energy $E_B = 0.1$ eV. One can see that there is no (or at least a very weak) hybridization effect on the energy position of the surface state at $E_B = -1.24$ eV after adsorbing a PTCDA monolayer. Additionally, the corresponding parabola in the vicinity of the $\overline{Y}$-point has not changed. This leads to the conclusion that the effective electron mass seems to be not (or at least very weak) modified by the molecule layer. In fact, the more interesting surface state is located at $E_B = 0.1$ eV, which is occupied in contrast to the state at $E_B = -1.24$ eV. Unfortunately, the calculation is not accurate enough to give insights on how the PTCDA-monolayer affects this occupied surface state. The parameters in the calculation are $\hbar\omega = 30$ eV, $\sigma_{k_{[001]}} = 0.05$ Å^{-1} , $\sigma_E = 0.03$ eV, and IMFP = 10 Å. A Monkhorst-Pack grid of 6x6x1 **k**-points has been used.

Moreover, and what could be very interesting is, that there seems to be another surface state at $\overline{Y}$ at the binding energy $E_B = -2.30$ eV which does not occur for the uncovered Ag(110) slab.

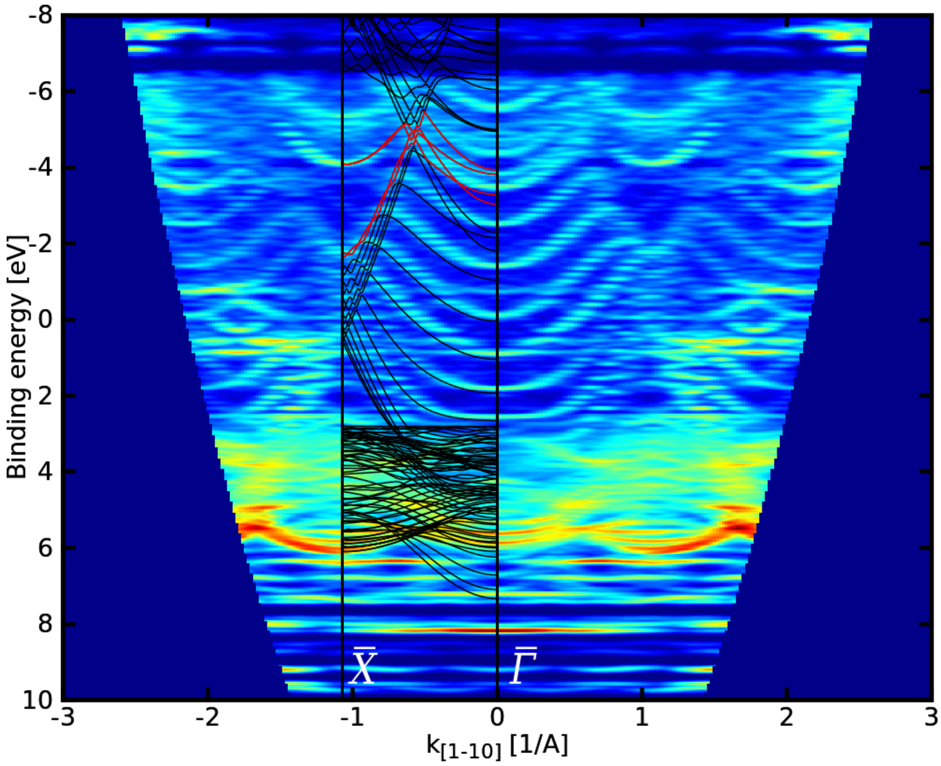

Figure 4.45: Photoemission simulation: Band map with an emission plane along the $k_{[1\bar{1}0]}$-axis of a 15-layer Ag(110) slab covered with a PTCDA monolayer. Additionally, energy bands from $\overline{\Gamma}$ to $\overline{X}$ of a 15-layer Ag(110) slab are plotted onto the photoemission intensity. The red curves picture surface states at $\overline{X}$.

In Fig. 4.45 the photoemission intensity of PTCDA on 15 layers Ag(110) is compared to the bandstructure from $\overline{\Gamma}$ to $\overline{X}$ of a clean 15-layer Ag(110) slab. The red lines denote the bands of the two surface states detected via bulk-projected band structures, both located at the $\overline{X}$-point, one at the binding energy $E_B = -4.04$ eV and the other one at the binding energy $E_B = -1.70$ eV. Again, one can see that there is no hybridization effect on the energy position of the surface state at $E_B = -4.04$ eV after adsorbing a PTCDA monolayer. In order to reveal possible modifications of the other surface state at $E_B = -1.70$, there is need for a denser k-mesh and for more atomic silver layers. The parameters in the calculation are $\hbar\omega = 30$ eV, $\sigma_{k_{[1\bar{1}0]}} = 0.05$ Å^{-1} , $\sigma_E = 0.03$ eV, and IMFP = 10 Å. A Monkhorst-Pack grid of 6x6x1 **k**-points has been used.

5 Conclusion

In the first part of the thesis, a comprehensive study on uncovered metal surfaces is performed within the framework of density functional theory. In particular, the low-index surfaces (111), (100), and (110) of the two fcc metals Al and and Cu are investigated. Several quantities characterising the electronic and structural properties of these surfaces are calculated including the surface energy and the work function. A particular focus is put on the accurate determination of the electronic structure of Shockley surface states. By comparing the bulk projected band structures with the band structures of the respective slab calculations, all relevant Shockley surface states are determined and their energetic positions, their energy dispersion (effective masses), and their wave functions are analysed. Care has been put on reaching converged results, in particular with respect to the number of atomic layers used in the metallic slabs. The results are compared to available experimental data where overall good agreement can be noted. In addition, photoemission intensity maps within the so-called one-step model are applied to the Cu(110) surface and corresponding energy-momentum maps have been obtained.

In the second part of the thesis the focus is set on a molecule/metal interface to investigate molecule-substrate interactions, where the model interface perylene-tetracarboxylic-dianhydride (PTCDA) on Ag(110) has been selected. In particular, the sensitivity of the electronic structure on the number of layers in the Ag(110) has been in the focus of interest. While many properties of molecule/metal interfaces, such as the adsorption geometry, do only require moderate thicknesses of metallic slabs (5 layers are often sufficient), other properties, such as the shape of molecule-derived density of states spectra (pDOS), are much more sensitive to the number of metal layers. In this work, we have demonstrated such an effect for the former LUMO (FLUMO) of the molecule which becomes occupied upon adsorption due to electron transfer from the metal. We have calculated the electronic structure for PTCDA monolayers sitting on 4–25 layers of Ag and observed a pronounced dependence of the pDOS on the amount of Ag layers and the fact whether an even or odd number has been used. These calculations also served as starting point for the simulation of photoemission intensity maps within the one-step-model which are compared to recent experimental data. The overall agreement of these simulations with the experimental data is very good. Moreover, an attempt has been made to shed light on an apparent discrepancy reported in constant binding energy maps at the energy position of the FLUMO. While one experiment has reported significant photoemission at normal emission and attributed this fact to the hybridization of the LUMO with metallic states, another experiment did not show such a normal emission peak. Unfortunately, the simulated photoemission maps resulting from this thesis could not provide a final answer to this open problem. The appearance of normal emission features in the LUMO peak could be demonstrated for the PTC-

DA/Ag(110) interface. Due to the slow convergence of the photoemission maps with respect to the number Ag layers in conjunction with the numerical effort of such computations (note that the 25 layer calculation already contains 338 atoms), future work will be necessary to clarify this issue.

Acknowledgements

It gives me great pleasure in acknowledging the support and help of my thesis supervisor Professor Peter Puschnig.

A special acknowledgement goes to my colleagues, to my friends, to my family, and last but not least to my girlfriend for being part of my life.

Finally, financial support from the Austrian Science Fund, project P23190-N16, is acknowledged.

Bibliography

[1] William Shockley. On the surface states associated with a periodic potential. *Phys. Rev.*, 56:317–323, Aug 1939.

[2] P. Straube, F. Pforte, T. Michalke, K. Berge, A. Gerlach, and A. Goldmann. Photoemission study of the surface state at $\overline{Y}$ on cu(110): Band structure, electron dynamics, and surface optical properties. *Phys. Rev. B*, 61:14072–14077, May 2000.

[3] P. Hohenberg and W. Kohn. Inhomogeneous electron gas. *Phys. Rev.*, 136:B864–B871, Nov 1964.

[4] W. Kohn and L. J. Sham. Self-consistent equations including exchange and correlation effects. *Phys. Rev.*, 140:A1133–A1138, Nov 1965.

[5] J. P. Perdew, K. Burke, and M. Ernzerhof. Generalized gradient approximation made simple. *Phys. Rev. Lett.*, 77:3865, 1996.

[6] J. P. Perdew, K. Burke, and M. Ernzerhof. Erratum: Generalized gradient approximation made simple. *Phys. Rev. Lett.*, 78:1396, 1997.

[7] J. Ziroff, F. Forster, A. Schöll, P. Puschnig, and F. Reinert. Hybridization of organic molecular orbitals with substrate states at interfaces: Ptcda on silver. *Phys. Rev. Lett.*, 104:233004, Jun 2010.

[8] P. Puschnig, E.-M. Reinisch, T. Ules, G. Koller, S. Soubatch, M. Ostler, L. Romaner, F. S. Tautz, C. Ambrosch-Draxl, and M. G. Ramsey. Orbital tomography: Deconvoluting photoemission spectra of organic molecules. *Phys. Rev. B*, 84:235427, Dec 2011.

[9] H.A. Bethe, R. Jackiw, and R.W. Jackiw. *Intermediate Quantum Mechanics.* Advanced book classics. Addison-Wesley, 1997.

[10] C. Fiolhais, F. Nogueira, and M.A.L. Marques. *A Primer in Density Functional Theory.* Lecture Notes in Physics. Springer, 2003.

[11] G. Czycholl. *Theoretische Festkörperphysik: Von den klassischen Modellen zu modernen Forschungsthemen.* Springer-Lehrbuch. Springer, 2007.

[12] Neil Ashcroft and David Mermin. *Solid state physics.* 1976.

[13] Charles Kittel. *Introduction to Solid State Physics.* John Wiley & Sons, Inc., New York, 7th edition, 1996.

[14] Hans Lueth. *Solid Surfaces, Interfaces and Thin Films.* Springer, 4th edition, 2001.

[15] H. Haken and H.C. Wolf. *The Physics of Atoms and Quanta: Introduction to Experiments and Theory.* Advanced Texts in Physics. Springer, 2005.

[16] Mel Levy. Universal variational functionals of electron densities, first-order density matrices, and natural spin-orbitals and solution of the v-representability problem. *Proceedings of the National Academy of Sciences*, 76(12):6062–6065, 1979.

[17] N. Troullier and José Luriaas Martins. Efficient pseudopotentials for plane-wave calculations. *Phys. Rev. B*, 43:1993–2006, Jan 1991.

[18] P. E. Blöchl. Projector augmented-wave method. *Phys. Rev. B*, 50:17953–17979, Dec 1994.

[19] G. Kresse and J. Hafner. *Ab initio* molecular dynamics for liquid metals. *Phys. Rev. B*, 47:558–561, Jan 1993.

[20] G. Kresse and J. Hafner. *Ab initio* molecular-dynamics simulation of the liquid-metal-amorphous-semiconductor transition in germanium. *Phys. Rev. B*, 49:14251–14269, May 1994.

[21] G. Kresse and J. Furthmüller. Efficiency of ab-initio total energy calculations for metals and semiconductors using a plane-wave basis set. *Computational Materials Science*, 6(1):15 – 50, 1996.

[22] G. Kresse and J. Furthmüller. Efficient iterative schemes for *ab initio* total-energy calculations using a plane-wave basis set. *Phys. Rev. B*, 54:11169–11186, Oct 1996.

[23] Hendrik J. Monkhorst and James D. Pack. Special points for brillouin-zone integrations. *Phys. Rev. B*, 13:5188–5192, Jun 1976.

[24] David Sholl and Janice Steckel. *DENSITY FUNCTIONAL THEORY - A Practical Introduction.* John Wiley & Sons, Inc., 2009.

[25] Peter Puschnig, Stephen Berkebile, Alexander J. Fleming, Georg Koller, Konstantin Emtsev, Thomas Seyller, John D. Riley, Claudia Ambrosch-Draxl, Falko P. Netzer, and Michael G. Ramsey. Reconstruction of molecular orbital densities from photoemission data. *Science*, 326(5953):702–706, 2009.

[26] Peter J. Feibelman and D. E. Eastman. Photoemission spectroscopy—correspondence between quantum theory and experimental phenomenology. *Phys. Rev. B*, 10:4932–4947, Dec 1974.

[27] S. Tanuma, C. J. Powell, and D. R. Penn. Calculations of electron inelastic mean free paths. ix. data for 41 elemental solids over the 50 ev to 30 kev range. *Surface and Interface Analysis*, 43(3):689–713, 2011.

[28] Jörg Neugebauer and Matthias Scheffler. Adsorbate-substrate and adsorbate-adsorbate interactions of na and k adlayers on al(111). *Phys. Rev. B*, 46:16067–16080, Dec 1992.

[29] K. Levenberg. A method for the solution of certain problems in least squares. *Quart. Applied Math.*, 2:164–168, 1944.

[30] Donald W. Marquardt. An algorithm for least-squares estimation of nonlinear parameters. *SIAM Journal on Applied Mathematics*, 11(2):431–441, 1963.

[31] S. V. Faleev, O. N. Mryasov, and T. R. Mattsson. Qsgw calculation of the work functions of al(111) and al(100) surfaces. *ArXiv e-prints*, October 2009.

[32] K. M. Ho and K. P. Bohnen. Investigation of multilayer relaxation on al(110) with the use of self-consistent total-energy calculations. *Phys. Rev. B*, 32:3446–3450, Sep 1985.

[33] P. O. Gartland, S. Berge, and B. J. Slagsvold. Photoelectric work function of a copper single crystal for the (100), (110), (111), and (112) faces. *Phys. Rev. Lett.*, 28:738–739, Mar 1972.

[34] M. J. G. Lee, M. Gensch, A. I. Shkrebtii, Th. Herrmann, W. Richter, N. Esser, and Ph. Hofmann. Surface states and resonances on al(110): Ultraviolet photoemission spectroscopy and *ab initio* calculations. *Phys. Rev. B*, 72:085408, Aug 2005.

[35] M. Heinrichsmeier, A. Fleszar, and A.G. Eguiluz. Lda calculation of the surface states on the (001), (110), and (111) surfaces of aluminum. *Surface Science Letters*, 285(1-2):A311 –, 1993.

[36] Xihui Liang, Cheng-Maw Cheng, Ku-Ding Tsuei, and Dah-An Luh. Surface band structure of al(100) studied with high-resolution angle-resolved photoelectron spectroscopy. *Journal of Electron Spectroscopy and Related Phenomena*, 184(11-12):551–555, 2012.

[37] G. V. Hansson and S. A. Flodström. Photoemission from surface states and surface resonances on the (100), (110), and (111) crystal faces of aluminum. *Phys. Rev. B*, 18:1562–1571, Aug 1978.

[38] A. Goldmann, V. Dose, and G. Borstel. Empty electronic states at the (100), (110), and (111) surfaces of nickel, copper, and silver. *Phys. Rev. B*, 32:1971–1980, Aug 1985.

[39] W. Jacob, V. Dose, U. Kolac, Th. Fauster, and A. Goldmann. Bulk, surface and thermal effects in inverse photoemission spectra from cu(100), cu(110) and cu(111). *Zeitschrift für Physik B Condensed Matter*, 63(4):459–470, 1986.

[40] M. Böhringer, W.-D. Schneider, K.Glöckler, E. Umbach, and R. Berndt. Adsorption site determination of PTCDA on Ag(110) by manipulation of adatoms. *Surf. Sci.*, 419:L95–L99, 1998.

[41] K Glöckler, C Seidel, A Soukopp, M Sokolowski, E Umbach, M Böhringer, R Berndt, and W.-D Schneider. Highly ordered structures and submolecular scanning tunnelling microscopy contrast of {PTCDA} and dm-pbdci monolayers on ag(111) and ag(110). *Surface Science*, 405(1):1 – 20, 1998.

[42] M. Wießner, J. Ziroff, F. Forster, M. Arita, K. Shimada, P. Puschnig, A. Schöll, and F. Reinert. Substrate-mediated band-dispersion of electronic states in adsorbed molecules. *Nature Communications*, 4:1514, 2013.